

**STRUCTURAL STUDIES OF *MYCOBACTERIUM TUBERCULOSIS*  
KATG, AN INH DRUG ACTIVATOR, AND *BRUCELLA ABORTUS*  
VIRB11, AN ATPASE OF TYPE IV TRANSLOCATION SYSTEM**

A Dissertation

by

HONG YU

Submitted to the Office of Graduate Studies of  
Texas A&M University  
in partial fulfillment of the requirements for the degree of

DOCTOR OF PHILOSOPHY

May 2007

Major Subject: Biochemistry

**STRUCTURAL STUDIES OF *MYCOBACTERIUM TUBERCULOSIS*  
KATG, AN INH DRUG ACTIVATOR, AND *BRUCELLA ABORTUS*  
VIRB11, AN ATPASE OF TYPE IV TRANSLOCATION SYSTEM**

A Dissertation

by

HONG YU

Submitted to the Office of Graduate Studies of  
Texas A&M University  
in partial fulfillment of the requirements for the degree of

DOCTOR OF PHILOSOPHY

Approved by:

Chair of Committee,  
Committee Members,

Head of Department,

James C. Sacchettini  
Patricia J. LiWang  
Dorothy E. Shippen  
Jerry Tsai  
Thomas R. Ioerger  
Gregory D. Reinhart

May 2007

Major: Biochemistry

## ABSTRACT

Structural Studies of *Mycobacterium tuberculosis* KatG, an INH Drug Activator, and *Brucella abortus* VirB11, an ATPase of Type IV Translocation System. (May 2007)

Hong Yu, B.S., Northeast Agriculture University, China;

M.S., Kansas State University

Chair of Advisory Committee: Dr. James C. Sacchettini

Catalase-peroxidase (KatG) of *Mycobacterium tuberculosis* is a bifunctional heme enzyme that has been shown to play an important role in the activation of a first line drug, isoniazid (INH), used in the treatment of tuberculosis infection. Mutations in the *katG* gene have been found to be associated with INH resistance. The most commonly encountered mutation is the Ser315Thr point mutation. In this dissertation, the x-ray crystallographic structures of *Mtb*KatG and the mutant enzyme KatG[S315T] are presented to explore the molecular basis of the INH activation and resistance. The structure is dimeric and contains a heme cofactor in each subunit of the dimer. The most important change in KatG[S315T] is due to the presence of the methyl group of the threonine 315 side chain, which is located at the narrowest part of the substrate channel. The protruding methyl group effectively constricts the accessibility to the heme by closing down the dimensions of the channel, constraining the substrate entrance.

VirB11 of *Brucella abortus* is a hexameric ATPase that belongs to the type IV secretion system. The crystal structure of *Ba*VirB11 was found to contain six molecules per asymmetric unit. The Walker A (P loop), His box, and Glu box from the C-terminal

domain are located at the interface of the N- and C-terminal domain. A large conformational change was found in the linker region when compared with that of HP0525 structure, the VirB11 analogous from *H. pylori*. To elucidate the functional role of each domain, seven functional mutations were generated and used for biochemical studies. The GER motif and the linker region were found to be crucial for ATP hydrolysis activity of *BaVirB11*. Mutations in the GER motif (R101Q) and the linker region (R120E) of *BaVirB11* completely abolish the ATP hydrolysis activity of the enzyme. The binding affinities of the two mutants to the ATP; however, are similar to that of the wild-type enzyme, indicating that mutation in the GER motif or the linker region has no effect on ATP binding.

## **DEDICATION**

To my parents, my husband Jeff and son Daniel, for their love and support.

## ACKNOWLEDGEMENTS

I would like to thank my advisor, Dr. James Sacchettini, for his valuable advice and great guidance during my graduate years. He has been an outstanding and challenging mentor, and inspired me to get into the challenging field of structural biology. His encouragement, insightful comments, and incisive criticisms were invaluable. I am also very grateful to the members of my advisory committee: Dr. Patricia Liwang, Dr. Dorothy Shippen, Dr. Thomas Ioerger, and Dr. Jerry Tsai, for their constant support, suggestions and words of encouragement.

I would also like to thank my colleagues in Dr. Sacchettini lab who made this work possible, particularly Mr. Erik McKee, Dr. Gukulan Kuppan, Dr. Christoph Eicken, Dr. Rosemarie Swanson, Dr. Stan Sanwson, Dr. Arockiasamy, Dr. Chih-chin Huang, Dr. Mack Kuo, Dr. Sudharsan Sridharan, Dr. Dong Yang, Ms. Ana Camila Murillo, Dr. Sheng Ye, Dr. Ty Gould and Mrs. Karen Hodges for their advice and help at various stages of my research.

I have to thank our collaborator Dr. Magliozzo at the Department of Chemistry, Brooklyn College and The Graduate Center of the City University of New York, Brooklyn, New York for the work on the KatG project. I also would like to extend my gratitude to Dr. Renee Tsolis of the University of California, Davis, for the supply of VirB protein constructs and proteins.

Thanks to my family, my dear husband who pushed me through, my lovely son Daniel who made me proud all the time and my parents who love me and encourage me

to perform to my best. I also thank to my Christian friends who prayed for me constantly during my graduate years.

## NOMENCLATURE

AA	Amino Acid
ABC	ATP-binding Cassette
ADP	Adenosine 5'-diphosphate
ADP $\beta$ S	Adenosine 5'-( $\beta$ -thiol)-diphosphate
AIDS	Acquired Immunodeficiency Syndrome
ALS	Advanced Light Source
AMP	Adenosine 5'-monophosphate
AMPPCP	Adenosine 5'-( $\beta$ , $\gamma$ -methylene)-diphosphate
AMPPNP	Adenosine 5'-( $\beta$ , $\gamma$ -imido)-triphosphate
APS	Advanced Photon Source
APX	Ascorbate Peroxidase
ARP	<i>Arthromyces ramosus</i> Peroxidase
ATP	Adenosine 5'-triphosphate
ATP $\gamma$ S	Adenosine 5'-(3-O-thio) Triphosphate
ATS	American Thoracic Society
BCV	<i>Brucella</i> -containing Vacuole
BHA	Benzhydroxmic Acid
CCD	Charged Coupled Devices
CCP	Cytochrome C Peroxidase
CDC	Centers for Disease Control
CS	Cycloserine



CTD	C-terminal Domain
DMSO	Dimethyl Sulfoxide
DTT	Dithiothreitol
EMB	Ethambutol
ETH	Ethionamide
FOM	Figure of Merit
FQ	Fluoroquinolones
GSP	General Secretion Pathway
HEPES	N-(2-hydroxyethyl)-piperazine-N'-2-ethanesulfonic Acid
HIV	Human Immunodeficiency Virus
HRP or HP	Horseradish Peroxidase
HRPC	Horseradish Peroxidase Isoenzyme C
INH	Isoniazid
IP	Image Plate
IPTG	Isopropyl-beta-D-Thiogalactopyranoside
KatG	Bacterial Catalase-Peroxidases
LB	Luria Bertani Broth
LiP	Lignin Peroxidase
LPS	Lipopolysaccharide
MAD	Multiwavelength Anomalous Dispersion
MDR-TB	Multiple Drug Resistant Strains of Tuberculosis
MIC	Minimum Inhibition Concentration

MIR	Multiple Isomorphous Replacement
MnP	Manganese Peroxidase
MPD	2-methyl-2,4-pentanediol
MSD	Membrane Spanning Domains
MW	Molecular Weight
NAD <sup>+</sup>	Nicotinamide Adenine Dinucleotide (oxidized form)
NADH	Nicotinamide Adenine Dinucleotide (reduced form)
NADPH	Nicotinamide Adenine Dinucleotide Phosphate (reduced form)
NBD	Nucleotide Binding Domain
NCS	Non-crystallography Symmetry
NTD	N-terminal Domain
PAGE	Polyacrylamide Gel Electrophoresis
PAS	Para-Aminosalicylic Acid
PCR	Polymerase Chain Reaction
PDB	Protein Data Bank
PEG	Polyethylene Glycol
PMSF	Phenylmethylsulfonyl Fluoride
Psi	Pounds per Square Inch
PT	Pertussis Toxin
PZA	Pyrazinamide
RMSD	Root-Mean-Square Deviation
RT	Room Temperature

SAD	Singlewavelength Anomalous Dispersion
SIR	Single Isomorphous Replacement
SDS	Sodium Dodecyl Sulphate
Se-Met	Selenium Methionine
TMS	Trans-Membrane
TOSS	Type I Secretion System
Tris	Tris(hydroxymethyl) Aminomethene
T2SS	Type II Secretion System
T3SS	Type III Secretion System
T4SS	Type IV Secretion System
WHO	World Health Organization
wt	wild-type

## TABLE OF CONTENTS

	Page
ABSTRACT .....	iii
DEDICATION .....	v
ACKNOWLEDGEMENTS.....	vi
NOMENCLATURE.....	viii
TABLE OF CONTENTS.....	xii
LIST OF FIGURES.....	xiv
LIST OF TABLES.....	xvii
 CHAPTER	
I INTRODUCTION.....	1
Overview .....	1
Tuberculosis .....	3
<i>M. tuberculosis</i> Catalase-Peroxidase (KatG) .....	14
Brucellosis and <i>Brucella abortus</i> .....	27
Type IV Secretion System (T4SS) .....	31
 II STRUCTURE DETERMINATION BY X-RAY CRYSTALLOGRAPHY.....	
Introduction .....	49
Protein Crystals.....	50
X-ray Diffraction .....	53
Data Processing .....	56
Phasing Method ----- Molecular Replacement.....	57
Phasing Method -----Multiple Wavelength Anomalous Dispersion (MAD) Phasing .....	59
Model Building and Refinement .....	62

CHAPTER	Page
III STRUCTURAL STUDIES OF <i>Mtb</i> KatG, KatG[S315T] MUTANT, AND <i>Mtb</i> KatG COMPLEXED WITH KCN AND INH.....	65
Introduction .....	65
Materials and Methods .....	67
Results and Discussion .....	73
Summary .....	110
IV STRUCTURAL AND FUNCTIONAL STUDIES OF VirB11 FROM <i>BRUCELLA ABORTUS</i> .....	112
Introduction .....	112
Materials and Methods .....	118
Results and Discussion .....	130
Summary .....	155
V SUMMARY AND FUTURE DIRECTIONS .....	157
REFERENCES .....	163
VITA .....	196

## LIST OF FIGURES

FIGURE	Page
1. Chemical structures of the first line antituberculosis drugs .....	7
2. INH activation pathway .....	12
3. Sequence alignments of class I peroxidases.....	17
4. Proposed reaction pathways of catalase-peroxidase <i>M. tuberculosis</i> .....	19
5. Sequence alignments of KatGs from several bacterial species.....	22
6. Ribbon diagrams of peroxidases from class I peroxidase super-family .....	24
7. Substrate binding site in HRPC -BHA and ARP-BHA structure complexes .....	26
8. Examples of medically important pathogens that use Type IV secretion systems (T4SS) to translocate effector molecules and virulent factors into host cells.....	34
9. Subunits of the multiprotein complexes in T4SS .....	37
10. Crystal unit cell and the lattice plane.....	51
11. A single X-ray diffraction image generated from a protein crystal.....	54
12. Single plate-like crystals of <i>MtbKatG</i> .....	69
13. Ramachandran plot of <i>MtbKatG</i> .....	72
14. Overall structure of <i>MtbKatG</i> .....	75
15. Ribbon diagram of one subunit in the <i>MtbKatG</i> dimer .....	77
16. The heme active site of <i>MtbKatG</i> .....	79
17. Hydrogen-bond networks at the distal site of <i>MtbKatG</i> .....	82
18. The Trp-Tyr-Met adduct .....	84
19. The access channels to the distal active site.....	87

FIGURE	Page
20. The U-shaped channel and the features of the alternate conformations of Arg418 side chain .....	89
21. Ramachandran plot of the <i>Mtb</i> KatG [S315T] generated in PROCHECK.....	92
22. Electron density map showing the methyl group of the threonine 315 side chain in KatG[S315T] .....	93
23. Distal heme environment comparison between <i>Mtb</i> KatG and KatG[S315T] mutant .....	95
24. Structural comparisons of <i>Mtb</i> KatG and KatG[S315T] mutant at the distal side of the substrate access channel .....	97
25. Structure modeling of clinically significant mutants.....	103
26. Ramachandran plot of <i>Mtb</i> KatG-KCN-INH structure .....	107
27. View of INH binding at the distal heme binding pocket in close proximity to the substrate channel .....	108
28. View of the environment surrounding INH binding site .....	109
29. Sequence alignments of VirB11 from several bacterial species .....	113
30. One step Strep-tactin affinity purification of <i>Ba</i> VirB11.....	130
31. Chromatography of the gel filtration purification .....	132
32. ATPase activities of <i>Ba</i> VirB11 and its mutants .....	134
33. Comparisons of <i>Ba</i> VirB11 and its mutants on ATP-agarose binding .....	136
34. Crystals of the <i>Ba</i> VirB11 .....	140
35. Ribbon diagram of the structure of <i>Ba</i> VirB11 monomer .....	143

FIGURE	Page
36. Superposition of HP0525 monomer model and the best refined <i>BaVirB11</i> structure .....	144
37. A magnified view of the NTD-CTD interface .....	145
38. Ribbon diagram of the <i>BaVirB11</i> hexamer .....	147
39. Surface of the <i>BaVirB11</i> was displayed using the program SPOCK .....	148
40. Selected section of the electron density map at the linker region .....	150
41. A model of the represented region defined in the figure .....	151
42. Superimposition of HP0525 and <i>BaVirB11</i> at the ATP binding site .....	154



## LIST OF TABLES

TABLE	Page
1. Four recommended regimens (WHO) for treating patients with tuberculosis caused by drug-susceptible organisms .....	9
2. Data collection and structure refinement statistics for wild-type <i>MtbKatG</i> .....	74
3. Data collection and structure refinement statistics for <i>MtbKatG</i> [S315T] .....	91
4. Multiple data collections and refinements for <i>MtbKatG</i> and <i>MtbKatG</i> [S315T]..	94
5. INH sensitivity and catalase-peroxidase activity of <i>MtbKatG</i> mutants .....	101
6. Data collections and structure refinements for substrates soaked or co-crystallized <i>MtbKatG</i> .....	102
7. Data collection and structure refinement statistics for wt <i>MtbKatG</i> -KCN-INH.....	106
8. VirB11 mutants generated in this study .....	118
9. PCR primers used to generate <i>Brucella</i> VirB11 mutants .....	121
10. Data collection and structure refinement statistics for <i>BaVirB11</i> .....	141

## CHAPTER I

### INTRODUCTION

#### Overview

Both *Mycobacterium tuberculosis* and *Brucella abortus* are intracellular bacteria that can cause infections in mammals.

Tuberculosis (TB), an infectious disease caused by *Mycobacterium tuberculosis*, is the single leading cause of death worldwide due to the wide spread of multidrug-resistant strains and increasing infections among AIDS/HIV patients (WHO 2003). Isoniazid (INH), a frontline drug used in the treatment of tuberculosis, is a pro-drug that requires activation by the *M. tuberculosis* catalase-peroxidase (KatG) (Zhang et al., 1992). Shortly after the introduction of INH, bacteria strains resistant to the drug were identified (Middlebrook 1952; Dean 1953). Most INH resistance in clinical isolates has been associated with loss or decreased KatG activity due to mutations in the *katG* gene (Slayden and Barry 2000). The most commonly encountered mutation is the Ser315Thr point mutation, which has been found in over 50% of resistant clinical isolates (Slayden and Barry 2000). Understanding the molecular basis of the pro-drug activation and the relationship between drug resistance and the structure and function of KatG is essential for new drug development.

---

This dissertation follows the style and format of the *EMBO Journal*.

Brucellosis is the most frequent human zoonosis of global importance (Young 1983; Boschioli et al., 2001). The disease is characterized by acute fever, night sweats, undue fatigue, anorexia, headache, and several neurological disorders. The causative agents of brucellosis are intracellular pathogens *Brucella spp.* The severity of the disease and lack of vaccines suitable for use in human has led to the investigation of *Brucella* as an agent for bioterrorism (Culter et al., 2005). Indeed, *Brucella* has been classified as a class 3 bioterrorism agent (Robinson-Dunn 2002). Like *M. tuberculosis*, *Brucella spp.* are Gram-negative bacteria that survive and replicate within host monocytes and macrophages, causing chronic granulomatous infections both in animals and humans (Smith and Ficht 1990). *Brucella abortus* is the aetiological agent of bovine brucellosis, which induces abortion and sterility in cattle and causes significant economic losses (Corbel 1997; Ficht 2003). A key aspect of the virulence of *Brucella* species is thought to be due to their ability to avoid the killing mechanism within host cells via the type IV secretion system (T4SS), encoded by the *virB* region (O'Callaghan 1999; Comerchi et al., 2001; Baron et al., 2002; Boschioli et al., 2002a). The bacteria use T4SS to translocate DNA and protein effectors across the cell envelope into the host cells. *A. tumefaciens*, a plant pathogenic bacterium, uses T4SS to deliver DNA and proteins into plant cells causing the Crown Gall tumour disease. *H. pylori*, a causative agent of peptic ulcers, translocate a 40 kDa protein CagA into the host cell through T4SS to interfere with the signaling pathway of the host cell (Segal 1999). VirB11 ATPase is an energy-consuming component of T4SS, presenting a good target for developing new drugs against pathogenic bacteria. Elucidating structural features and molecular determinants

that govern the activity of the enzyme may lead to drug discovery. Structural studies are important for understanding the molecular basis of drug resistance and ultimately inhibitor design. In this thesis, we describe the structure of KatG[S315T], which explains the mechanism of isoniazid resistance. We also describe the structure of VirB11 in *Brucella*, which is a virulent factor of the pathogenic bacterium.

Chapter I introduces *M. tuberculosis*, the front-line drug isoniazid (INH) and the catalase-peroxidase (KatG) that is responsible for the pro-drug activation. It also describes brucellosis and the type IV secretion system of *Brucella spp.* Chapter II describes the X-ray crystallographic methods. Chapter III presents the X-ray crystal structures of the *Mtb* KatG, S315T mutant and the wild-type *Mtb*KatG co-crystallized with INH. Functional and structural studies of VirB11 ATPase from *Brucella abortus* are described in chapter IV. Future studies and perspectives on VirB11 and other components of T4SS are proposed in chapter V.

## **Tuberculosis**

### ***History of Tuberculosis***

*Mycobacterium tuberculosis* has affected humans for several millennia (Ayvazian 1993) and remains a devastating public health threat with an estimated eight million people contracting the disease and approximately two million deaths worldwide each year (WHO 2003). In the United States, bacteria of this genus have significantly increased in prevalence in the past two decades due to synergistic co-infection among AIDS/HIV

patients and the emergence of wide spread multi-drug resistant strains (Musser 1995). It has been estimated that approximately 1 billion people will be newly infected in next 20 years, over 150 million people will get sick, and 36 million will die of tuberculosis, if proper controls are not instituted (WHO 2005).

Tuberculosis (TB) is an ancient disease that can be traced back to the predynastic era (Morse et al., 1964). Tuberculosis probably occurred as a sporadic disease in early history (Bates and Stead 1993). The epidemic slowly spread as a result of increasing population density. During the so-called “Great White Plague” in the seventeenth century, almost all Western Europeans became infected with TB, and about one in four deaths were due to tuberculosis (Dubos 1952). As infected Europeans traveled to and colonized distant cities, the epidemic spread worldwide. By the turn of the 19th Century, the estimation of TB death rate was seven million per year and the pulmonary TB rate was 50 million per year worldwide (Bates and Stead 1993).

The invention of antimicrobial chemotherapy in the 20<sup>th</sup> century was a great contribution to modern medicine. The first vaccine used on humans was introduced by French physician Calmette in 1921 and the vaccines have been widely used for tuberculosis prevention since World War II (Sakula 1982). With the development of the antibiotic streptomycin by Schatz and Waksman in 1944 (Schatz et al., 2005), treatment of tuberculosis became a possibility. When more effective drugs such as isoniazid (INH) and pyrazinamide (PZA) were introduced in the early 1950s, tuberculosis became a treatable disease (Temple 1951).

From early 1950s to 1980s, TB cases declined significantly with the worldwide implementation of disease control and prevention program. From 1985 through 1990, however, the number of reported cases has increased rapidly due to the neglect of TB control programs, insurgence of HIV/AIDS, and immigrations (Schweinle 1990). Multiple drug resistant strains of tuberculosis (MDR-TB), resistant to both isoniazid and rifampin at least, are the emerging public health crisis in many regions of the world. The World Health Organization (WHO) declared TB a global health emergency in 1993. Since then, new cases have decreased due to the widespread use of directly observed therapy, short-courses (DOTs), treatments regiment recommended by the World Health Organization.

### ***Microbiology and Pathogenesis of Tuberculosis***

Tuberculosis is a complex communicable respiratory infection of human caused by *M. tuberculosis* and less commonly by *M. africanum* and *M. bovis*, collectively referred to as *tubercle bacilli* (Coberly et al., 2001). *M. tuberculosis* has been classified in the genus of *Mycobacterium*, which belongs to the family of Mycobacteriaceae of the order of Actinomycetales (Osoba 2003). A virulent strains of *M. tuberculosis* that infects humans is H37RV (Daniel et al., 1997).

Mycobacteria are acid-fast, non-spore forming, non-motile, and non-encapsulated bacilli. They are slender, slightly curved, obligate aerobes averaging 4x 0.3mm in size. The distinct feature of Mycobacteria is their unique and complex cell walls rich in lipid

complexes. The lipid content of the cell wall is remarkably high (60% as contrasted to 20% in Gram negative organisms, and 1-4% in Gram positives) (Coberly 2001).

The lipid wall of mycobacteria is responsible for difficulty in staining, acid-fastness, and the relative resistance to host phagocytic defenses.

The pulmonary tuberculosis is usually caused by the inhalation of tubercle bacilli in cough spray (Rieder et al., 1989). The majority of inhaled bacilli are destroyed by pulmonary alveolar macrophages. However, bacilli that escaped macrophage killing start to multiply within the macrophages and establish primary infection (Alland et al., 1994). T cells respond nonspecifically to the components of the bacilli leading to secretion of the gamma-interferon, which causes macrophage aggregation and activation, enabling more aggressive phagocyte killing (Ellner 1997). If these early, nonspecific reactions do not wipe out the infection, bacilli are transported to the lymph nodes at the hilum of the lung, resulting in the formation of granuloma.

### ***Treatments of Tuberculosis***

The abnormal thickness of the lipid bilayer, along with its slow-growing nature and the co-existing of semi-dormant and dormant forms, complicate tuberculosis chemotherapy, often requiring months of treatment.

Drugs used in the chemotherapy of tuberculosis are divided into two categories: the first line and the second line agents. The first line agents (Figure 1) including isoniazid (INH), rifampin, pyrazinamide (PZA), Ethambutol (EMB) and streptomycin, are the most commonly used drugs against *M. tuberculosis* with a low incidence of





toxicity. The second line drugs are used when resistance or unacceptable toxicity precludes the use of first line agents. They are generally less effective and more toxic. The second line drugs include kanamycin, amikacin, capreomycin, cycloserine (CS), ethionamide (ETH), para-aminosalicylic acid (PAS), and fluoroquinolones (FQ).

The American Thoracic Society (ATS) and the Centers for Disease Control (CDC) have collaborated to develop joint guidelines for the diagnosis, treatment, prevention, and control of tuberculosis. The guideline was published in 1994 for treating tuberculosis in settings where mycobacteria cultures, drug susceptibility testing, radiographic facilities, and second-line drugs are routinely available (ATS/CDC 1994). There are four recommended regimens for treating patients with tuberculosis caused by drug-susceptible organisms (Table 1). Each regimen has an initial phase of 2 months followed by a choice of several options for the continuation phase of 4 to 6 months.

### ***Drug Resistant Tuberculosis***

Drug resistance as a limiting factor for a successful TB treatment was recognized immediately following the introduction of the first antibiotic streptomycin in 1946 (Youmans and Feldman 1946). Subsequent studies proved that the increase in drug resistance following mono-therapy was due to the selection of the drug-resistant mutants (Temple 1951) (Dean and Hinshelwood 1953). In many parts of the world such as Africa and Asia, drug resistant tuberculosis is an increasing problem. The World Health Organization estimated that up to 50 million persons worldwide may be infected with drug resistant TB strains.

Table 1. Four recommended regimens (WHO) for treating patients with tuberculosis caused by drug-susceptible organisms

	TB treatment regimens			
	I	II	III	IV
Recommended Drugs and Dosage (mg/kg)	INH 4-6 RIF 8-12 PZA 20-30	INH 4-6 RIF 8-12 PZA 20-30 EMB 15-20 or SM 12-18	INH 4-6 RIF 8-12 PZA 20-30 EMB 15-20 or SM 12-18	INH 4-6 RIF 8-12
Treatment Length	Daily for 2 months	Daily for 2 weeks	3 times/week for 6 months	Daily for 9 months
Follow up Treatments	INH + RIF Daily or 2-3 times/wk for 4 months	2 times/week for 6 weeks		
Follow up Treatments		INH 4-6 RIF 8-12 for 4 months		

INH (Figure 1A) is the mostly common used drug for treating tuberculosis. Following its introduction in 1952, bacteria strains that were resistant to INH were detected (McDemott 1958). Mutations leading to INH resistance have been identified in different genes including *katG*, *inhA* and *ahpC* (Sherman et al., 1996). A variety of point mutations in two genes have been identified that account for most of clinical INH resistance characterized to date: the *katG* gene, which encodes a catalase-peroxidase

(KatG) (Stoeckle et al., 1993), and the *inhA* gene, which encodes a fatty-acyl carrier protein enoyl reductase (Banerjee et al., 1994). Mutations in these genes account for 60-70% (*katG*) and 10-15% (*inhA*) of INH-resistant tuberculosis and vary considerably with location (Sherman et al., 1996).

MDR-TB is a form of tuberculosis that is resistant to two or more of the primary drugs used for the treatment of tuberculosis. The first report of MDR-TB outbreak at a London hospital HIV Unit occurred in August 1995, and the second in June 1996 (Breathnach et al., 1998). By the year of 2001, there were about 50 million people infected with MDR-TB (Espinal et al., 2001).

Treatment for MDR-TB involves drug therapy over many months or years. Despite the longer course of treatment, the cure rate decreases from over 90 percent for nonresistant strains of TB to 50 percent or less for MDR-TB (Espinal et al., 2001). In 2003, the CDC in Atlanta USA reported that 7.7% of tuberculosis cases in the U.S. were resistant to isoniazid and 1.3% resistant to both isoniazid and rifampin. About 300,000 new cases of MDR-TB are diagnosed around the world each year and 79% of the MDR-TB cases show resistance to three or more drugs (ATS/CDC 2003). MDR-TB has been a particular concern among HIV-infected persons. Patients with HIV/AIDS are at a greater risk of developing TB. The spread of antibiotic-resistant strains presents a serious threat to current tuberculosis control programs throughout the world.

### ***Isoniazid, a First Line Anti-tuberculosis Drug***

Isoniazid (INH) has been the most widely used of all antituberculosis drugs for the past several decades. INH was first synthesized by Meyer and Malley in 1912 (Meyer 1912). However, its antituberculous effect was not recognized until 1942 (Chorine 1945). Three drug companies, Hoffman LaRoche, E.R. Squibb & Sons, and Bayer, developed INH simultaneously in 1952 by reshuffling chemical groups in thiosemicarbazone (Bernstein et al., 1952); (Fox 1952); (Offe et al., 1952). Since its discovery, INH has been a mainstay TB drug and is the cornerstone of all effective regimens for TB treatment and prevention. The emergence and outbreak of MDR-TB has renewed the interest in understanding the mechanisms of drug activation and resistance in *M. tuberculosis* (Bloom and Murry 1992).

The structure of INH consists of a pyridine ring and a hydrazide group (Figure 2). Both the pyridine and hydrazide moieties are essential for the high level of activity of INH against *M. tuberculosis* (Bernstein et al., 1952). *M. tuberculosis* is highly susceptible to INH with MIC values in the range of 0.01 to 0.25 ug/ml. However, INH is active against growing tubercle bacilli but not resting bacilli (Zhang 2005). *M. bovis* is slightly less susceptible to INH than to *M. tuberculosis*. *M. smegmatis* and *M. avium* are relatively insensitive to INH treatment with MIC of 10-100 ug/ml. Other bacterial species outside the mycobacterial genera are highly resistant to INH (MIC greater than 600 ug/ml) (Pansy et al., 1952). The reason for these differences is that *M. tuberculosis* contains only KatG that has both peroxidase and catalase activities, whereas other

bacterial species contain one more catalase in addition to a peroxidase-catalase protein (Shoeb 1985). The activities of KatG are responsible for INH activation, whereas the activity of a catalase is not. The mechanism by which catalase confers protection against INH is not known. A plausible explanation is that catalase scavenges  $\text{H}_2\text{O}_2$  and inhibits  $\text{H}_2\text{O}_2$ -dependent peroxidase-mediated oxidation of INH (Shoeb 1985).

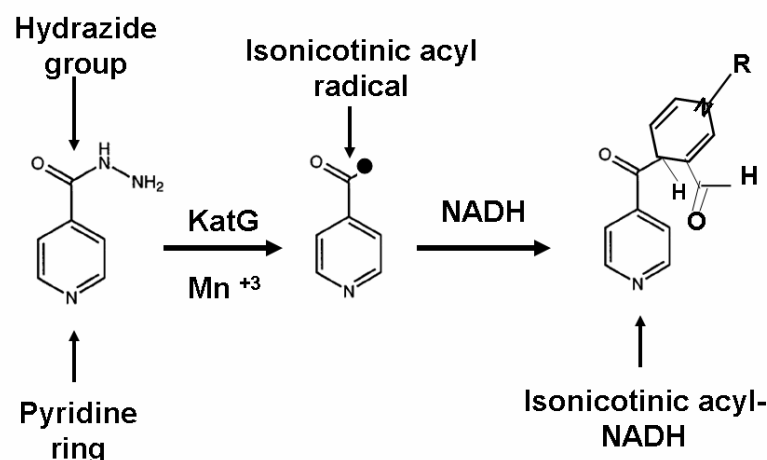


Figure 2. INH activation pathway. The figure was draw to show the isonictinic acyl radical and the INH-NAD adduct.

### ***INH Activation and the Drug Targets***

INH is a pro-drug that requires activation by *M. tuberculosis* KatG. However, the mechanism of activation has not been precisely elucidated. It is not known where the substrate-binding site is located in *M. tuberculosis* KatG, and how the electrons are

transferred between the enzyme and the substrate. It has been shown that initiation of isoniazid oxidation starts with the resting enzyme, oxygen, and the reductant (Chouchane et al., 2000). Oxidation of INH may also be mediated nonenzymatically by Mn(III) (Magliozzo and Marcinkeviciene 1997). Activation of INH, by either KatG or Mn+3, leads to an acyl radical species that can attack the 4th position of the nicotinamide group of NAD(H) to yield a covalent isonicotinoyl-NAD adduct (Figure 2) (Rozwarski et al., 1998). Despite numerous and intensive studies, knowledge of the mechanism of INH activation is limited (Ghiladi et al., 2005). The consensus opinion is that *Mtb*KatG oxidizes INH to an isonicotinic acyl radical, which then couples to NAD<sup>+</sup> to form an isonicotinoyl-NAD adduct (Figure 2).

The primary target of INH inhibition is thought to be the mycolic acid synthesis pathways. INH treatment can cause the loss of acid-fastness in mycobacteria (Middlebrook 1952). InhA is a key enzyme involved in the biosynthesis of mycolic acids, which are specific components of the mycobacterial cell wall (Marrakchi et al., 2000). It was first identified as the drug target of INH using genetic experiments (Banerjee et al., 1994) (Dessen et al., 1995). Mutations in the InhA gene in INH-resistant clinical strains were identified and a point mutant (S94A) was shown to confer resistance to INH in *M. smegmatis* and in *M. bovis* (Banerjee et al., 1994). Mutations in InhA that have been identified in INH resistant strains of Mycobacteria were found to be localized to the binding site of the isonicotinoyl-NAD adduct and were shown to result in a decreased affinity of the InhA enzyme for NADH (Basso et al., 1998). Much progress has been made in regard to the INH inhibition of the InhA enzyme by means of

biochemical and crystallographic studies (Johnsson et al., 1998); (Rozwarski et al., 1998); (Quemard et al., 1995). INH has been shown to inhibit the catalytic activity of InhA *in vitro* (Johnsson et al., 1995), and that isonicotinoyl-NAD is a slow, tight-binding competitive inhibitor of InhA (Rozwarski et al., 1998); (Rawat et al., 2003). The co-crystal structure revealed that the isonicotinoyl-NAD adduct binds irreversibly to a cysteine residue near the active site of InhA, blocking NADH-binding sites (Rozwarski et al., 1998). Inactivation of InhA alone was shown to be sufficient for inhibition of mycolic acid biosynthesis (Kremer 2003).

### ***M. tuberculosis* Catalase-Peroxidase (KatG)**

All living organisms, except anaerobic bacteria, require protection against the damaging effects of reactive oxygen species. The *M. tuberculosis* KatG is a component of the oxidative defense system of the bacteria and functions primarily as a catalase to remove hydrogen peroxide. Such catalase activity is regarded as one of the virulence factors for *M. tuberculosis* (Middlebrook 1954), because this reaction detoxifies reactive oxygen species generated by macrophages and facilitates the bacterial survival. Strains of *M. tuberculosis* lacking the *katG* gene are heavily attenuated in animal models (Pym et al., 2002). On the other hand, *M. tuberculosis* KatG functions as a peroxidase, oxidizing INH to its active form. KatG is thought to be the only enzyme in *M. tuberculosis* that is capable of generating isoniazid susceptibility (Zhang et al., 1992). It has been shown that most INH resistance in clinical isolates results from blocking prodrug activation through

mutation in the katG gene that alters or diminishes catalase-peroxidase activity (Musser 1995).

In the following section, the peroxidase family will be introduced and the catalase and peroxidase properties of KatG will be summarized. Reaction mechanisms of KatG and class I peroxidases will be compared and the structural studies of class I peroxidases will be reviewed.

### *Classification of Peroxidases*

Based on the sequence similarity, KatGs have been classified into the class I peroxidase superfamily (Welinder 1992b).

Peroxidases are ubiquitous oxidative heme-containing enzymes that utilize hydrogen peroxide to oxidize a wide variety of organic and inorganic compounds. They have been implicated in diverse biological processes that include cell wall synthesis and degradation, stress response, signaling during oxidative stress, and removal of xenobiotics (Rodriguez-Lopez 2001). The plant peroxidase superfamily includes peroxidases of prokaryotic origin, secreted fungal and secreted plant peroxidases.

The plant peroxidase superfamily is further classified into three families, class I, class II, and class III (Dunford 1999). Class I peroxidases consist of peroxidases of prokaryotic origin, including plant peroxidases, e.g. horseradish peroxidase (HRP), ascorbate peroxidase (APX), fungal peroxidases, e.g. cytochrome c peroxidase (CCP), and bacterial catalase-peroxidases (KatGs). Class I peroxidases contain no



carbohydrate, no cysteine bridge ions, and no signal peptide for secretion. Class II peroxidases include the secretory fungal peroxidases such as lignin peroxidase (LiP), manganese peroxidase (MnP) (Sundaramoorthy 1994), and *Arthromyces ramosus* peroxidase (ARP). Class II peroxidases contain an amino terminal signal peptide sequence for the secretion through the endoplasmic reticulum (Welinder 1992a). Class III peroxidases are the secretory plant peroxidases that are targeted for the secretory pathways (Welinder 1992b). All members of the three classes catalyze the reduction of hydrogen peroxide.

The sequence alignment for the class I peroxidase superfamily is shown in Figure 2. There are three additional insertions in the N-terminal domain of KatG which other class I peroxidases do not possess (Figure 3). The short insertion occurs between Trp 36 and Ala 60 in *MtbKatG*, named loop LL1. The large insertion LL2 occurs from Pro 194 to Asn 231 in *MtbKatG* and it is unique to all KatGs. Another conserved insertion among KatGs occurs from Pro 280 to Ile 313 in *MtbKatG*, named loop LL3. Structural consequences of the insertions in KatGs will be addressed in a later chapter.

KatGs are homodimeric proteins with monomers being twice as large as other members of class I peroxidase e.g. CCP or APX, which is ascribed to gene duplication (Welinder 1992a). Their N-terminal domain binds a heme and shows high sequence homology to yeast cytochrome c peroxidase (Duroux and Welinder 2003). The C-terminal domain has lost its heme and has a much lower homology to cytochrome c peroxidase. In contrast to other members of the class I family, KatGs exhibit a high

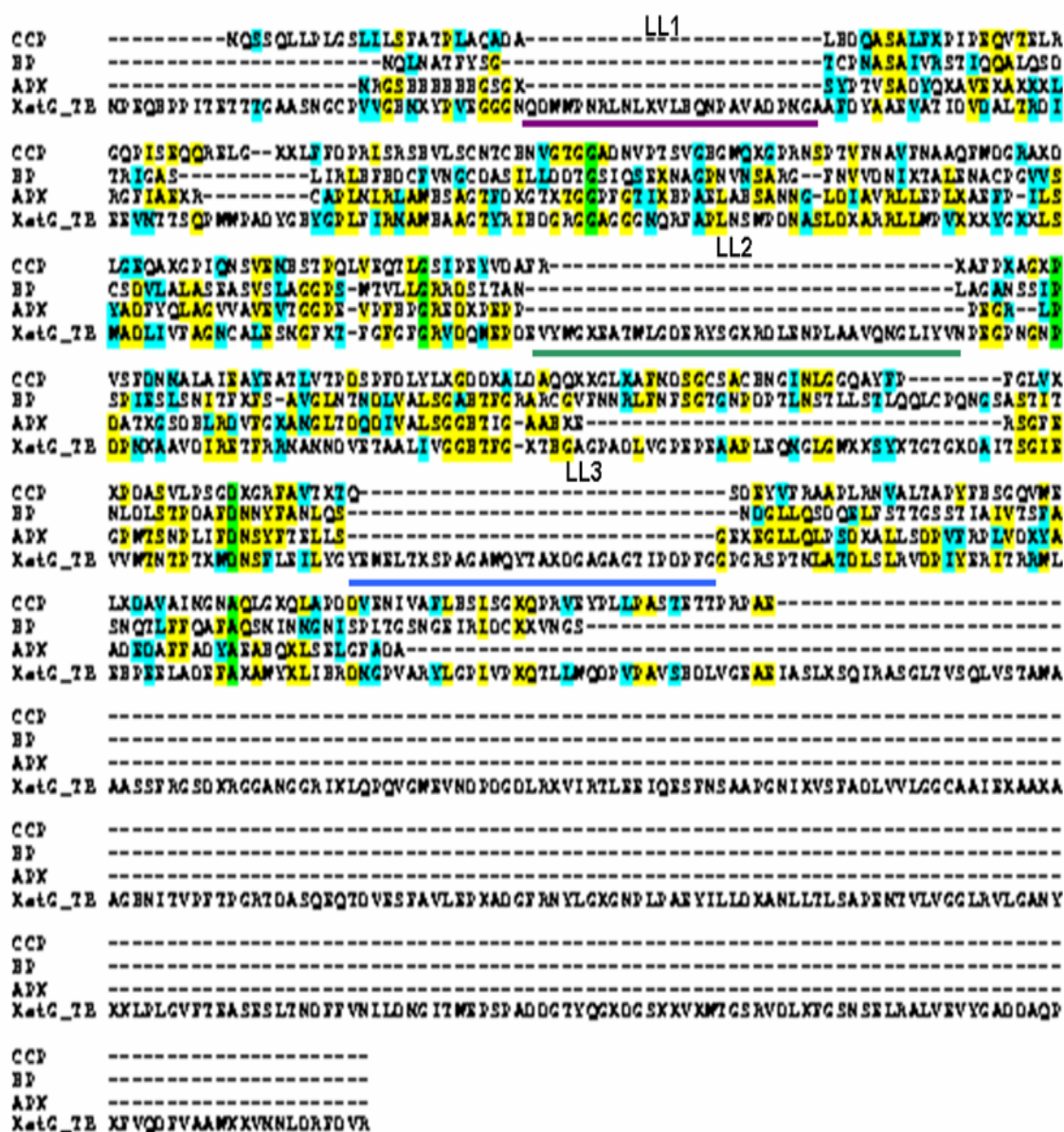


Figure 3. Sequence alignments of class I peroxidases. The figure was generated using the Clustalw multiple sequence alignment program in Biology Workbench. CCP: cytochrome c peroxidase; HP: horseradish peroxidase; APX: ascorbate peroxidase; KatG\_TB: *M. tuberculosis* KatG. LL1: loop 1; LL2: loop 2; LL3: loop 3 in *Mtb*KatG.

catalase activity comparable to monofunctional catalase, despite having low sequence similarity with typical monofunctional catalase (Murthy et al., 1981).

### ***Reaction Mechanisms of Class I Peroxidases***

Class I peroxidases, in general, show very broad substrate specificity and produce highly reactive products. The biological functions and the specific substrates in this peroxidase group have been difficult to verify and are not yet fully resolved. The generally accepted mechanism of the enzyme reaction is a three-step catalytic cycle in the classical peroxidation reaction as shown in Figure 4. The initial step in the catalytic cycle is the heterolysis of the oxygen-oxygen bond of hydrogen peroxide (**1**). Hydrogen peroxide binds to the heme in the Fe(III) state to form the two-electron oxidized enzyme intermediate, compound I, which contains an oxyferryl iron center and a second oxidizing equivalent stored as a radical Fe(IV)=OR\* (Hiner et al., 2002). The reaction causes the release of one water molecule. In the second step (**3**), compound I reacts with a reducing agent, typically a phenol derivative, to form compound II, in which the oxygen-oxygen bond of hydrogen peroxide is cleaved, and a phenolic radical is discharged leaving only the oxyferryl iron. Another water molecule is released during this reaction. In the third reaction step (**4**), the compound II is reduced back to the ferric state of the resting enzyme by a second reducing phenol derivative. In the peroxidase cycle, two reducing agents are converted to reactive phenolic radicals.

The catalase-peroxidase catalytic cycles both begin with the oxidation of the ferric heme by two electrons of a hydrogen peroxide to form oxyferryl porphyrin-protein

intermediate compound I (reaction **1** as showed in figure 4). The catalase cycle is completed by the reduction of compound I to the ferric resting enzyme by a second hydrogen peroxide molecule (reaction **2**). In the peroxidase cycle, compound I is reduced in the two sequential one-electron steps by an exogenous reducing agent as in other peroxidases (reaction **3&4**). In presence of excess hydrogen peroxide, compound II is oxidized into compound III (reaction **5**), an oxyperoxidase at an oxidation state IV (Chouchane et al., 2000); (Jakopitsch et al., 2005).

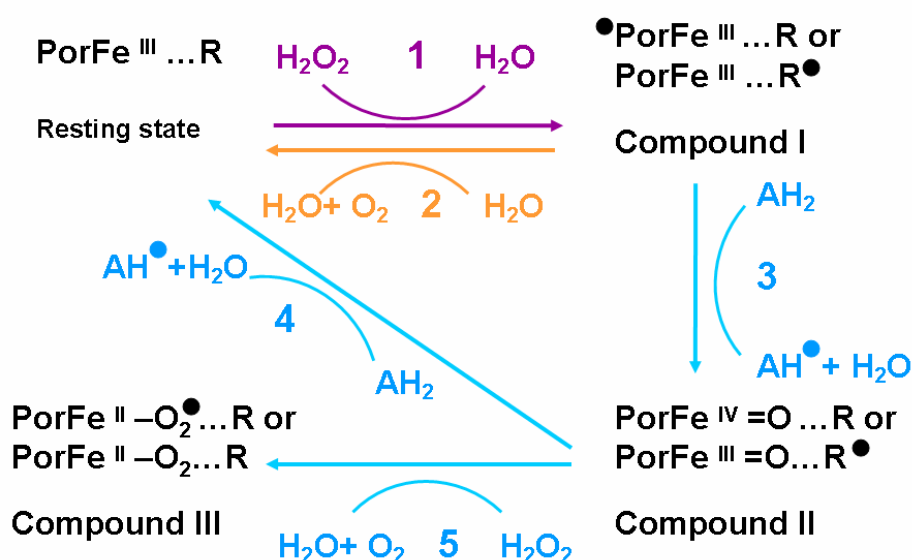


Figure 4. Proposed reaction pathways of catalase-peroxidase of *M. tuberculosis*. The peroxidase cycle includes reaction **1**, **3**, **4** and reaction **5** if there is excess hydrogen peroxide presence. The catalase cycle includes reaction **1** and **2**.  $\text{AH}_2$  represents a phenol derivative as a reducing agent in the peroxidase cycle. The dot represents a compound in its radical form. R represents protein residues.

### ***Properties of MtbKatG***

*M. tuberculosis* KatG is an 80 kDa bifunctional enzyme exhibiting a high catalase activity and a peroxidase activity with broad specificity (Heyme et al., 1993) (Welinder 1992a) (Zhang et al., 1992). It is capable of using a single active site to catalyze both the catalase and peroxidase reactions and thereby remove hydrogen peroxides from the biological system efficiently. It is believed that the catalase function of KatG is essential for the protection of the bacteria against oxygen free radicals within the macrophage (Manca et al., 1999).

KatGs differ from classic catalases in many respects. They have little sequence homology with typical catalases. In contrast to classic catalases which show a broad pH activity (range from pH 5.5 to 10.0), KatGs show maximum activity in a narrow pH range (6.0-6.5) and are not inhibited by typical catalase inhibitors (Nadler 1986). The catalase activity of KatG is greatly reduced by dialysis against low concentration hydrogen peroxide, while dialysis against hydrogen peroxide had no effect on the classic catalase (Nadler 1986). A covalent bond between the active site tryptophan, tyrosine, and methionine residues was found to present in the *H. marismortui* KatG, *Synechocystis* KatG, *B. pseudomallei* KatG, and *M. tuberculosis* KatG (Yamada et al., 2002; Jakopitsch et al., 2003a). Thus, the Trp-Tyr-Met adduct may be a common feature to all catalase-peroxidase. The integrity of the covalent adduct correlates to catalase activity but not the peroxidase activity of KatGs (Jakopitsch et al., 2003a). Studies had been shown that upon exchange of the active site tryptophan, the catalase activity was

dramatically diminished in *E. coli* (Hillar et al., 2000) or even lost in the *Synechocystis* (Regelsberger et al., 2000) and the bifunctional enzyme was converted to a monofunctional peroxidase (Jakopitsch et al., 2003a).

On the other hand, KatG possesses significant peroxidase activity with several reducing substrates such as *o*-Dianisidine, a typical substrate for class I peroxidase, *p*-Phenylendiamine, pyrogallol, NADH, and INH (Johnsson and Schultz 1994). The function of KatG as a peroxidase is believed to play a critical role in activation of INH (Zhang et al., 1992); (Zhang et al., 1993); (Rouse et al., 1995); (Wengenack et al., 1997); (Saint-Joanis et al., 1999). However, INH is not a natural substrate of KatG. The endogenous substrate of KatG has not yet been identified. The activation of INH by KatG produces an isonicotinic acyl radical, which can covalently attach to NAD<sup>+</sup> to form an isonicotinic acyl-NAD (INH-NAD) adduct (Figure 2). The ultimate target of the INH-NAD adduct is InhA. Binding of the INH-NAD adduct to InhA blocks enoyl-acyl ACP reduction and thereby results in inhibition of mycolic acid biosynthesis, which is a key component of the mycobacterial cell wall (Marrakchi et al., 2000).

It is interesting to note that other bacterial species outside the mycobacterial genera are highly resistant to INH, though they contain a *katG* gene with high homology to *MtbKatG*. Figure 5 shows sequence alignments of KatG amino acids from several bacterial species. *MtbKatG* shares 65% identity to *BpKatG*, 55% identity to *HmKatG*, and 50% identity to *E. coli* HRPI. *M. smegmatis*, which is in the mycobacterial genera, is insensitive to INH treatment though it contains a *katG* gene with 85% similarity to *M. tuberculosis*.





Figure 5. Sequence alignments of KatGs from several bacterial species. The figure was generated using the Clustalw multiple sequence alignment program in Biology Workbench. *MtKatG*: *M. tuberculosis* KatG; *KsmKatG*: *M. smegmatis* KatG; *BpKatG*: *B. pseudomalli* KatG; *SyKatG*: *Synechococcus* PCC 7942; *HmKatG*: *H. marsimortui* KatG.

### *Structural Studies of Class I Peroxidases*

The first X-ray structure solved for the peroxidase superfamily is that of the cytochrome c peroxidase (CCP) (Finzel et al., 1984). Since that time, great efforts have been made to probe the mechanism of the enzyme reaction and the characteristics of the intermediates, both structurally and biochemically. In the past two decades, there has been a rapid growth in crystallographic structural information on the peroxidase families. Structures have been obtained including horseradish peroxidase (HRP) (Gajhede et al., 1997), ascorbate peroxidases (APX) (Patterson and Poulos 1995); (Sharp et al., 2003) and the KatGs of several bacteria species (Yamada et al., 2002); (Carpena et al., 2003); (Bertrand et al., 2004).

The overall folding of the class I peroxidases are similar. Structural comparison among class I peroxidases is shown in Figure 6. The structures of the class I peroxidases contain mostly  $\alpha$ -helices. The structure of the two domains in KatGs, the N-terminal domain and the C-terminal domain, is organized similar to those of HRP and APX. A heme-binding consensus sequence is present in the N-terminal domain of the KatGs where the active site is located. The C-terminal domain has no heme-binding motif and its function is elusive. The rms differences for atoms in the heme-binding moiety and eight conserved residues in the active site are 0.27 Å between CCP and *HmKatG*, and 0.29 Å between APX and *HmKatG* (Yamada et al., 2002).

The native enzymes contain a heme, a ferric-protoporphyrin IX, with four pyrrole nitrogen bound to Fe(III). A ferric-protoporphyrin IX contains eight side chains, four



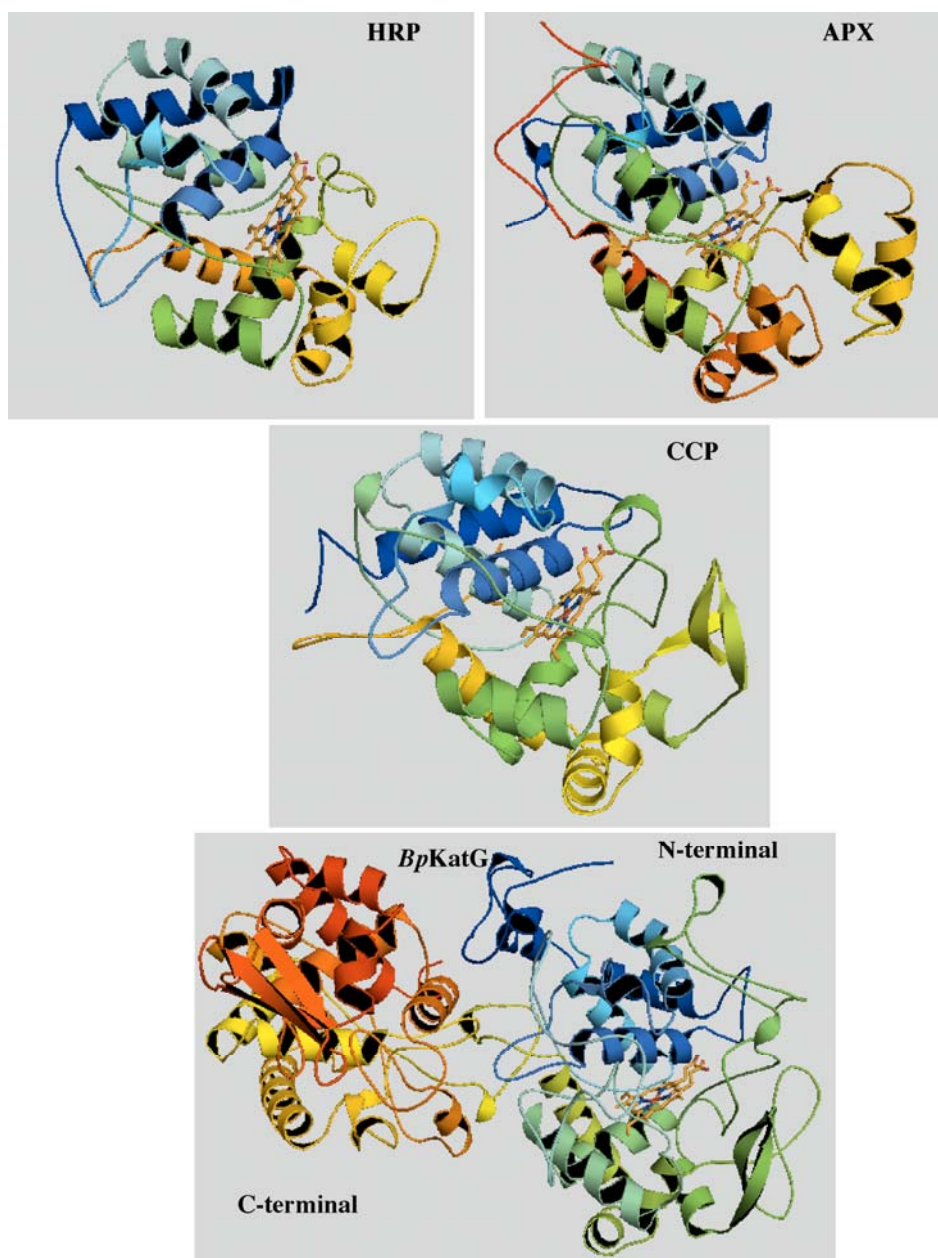


Figure 6. Ribbon diagrams of peroxidases from class I peroxidase super-family. HRP: horseradish peroxidase; CCP: cytochrome c peroxidase; APX: ascorbate peroxidase; BpKatG: *Burkholderia pseudomalli* KatG. The figure is constructed using PyMol (DeLano 2002).

methyl groups, two vinyl groups, and two propionate groups. In peroxidases, the heme is attached to the enzyme through a covalent linkage, in which the side chain of a histidine is attached to the fifth coordination position of Fe(III). The propionate side chains form hydrogen bonds with neighboring residues, and the binding of the heme to the protein is stabilized by the van der Waals contact between the organic porphyrin and the hydrophobic amino acid residues (Dunford 1999).

To better understand the enzyme reaction mechanism, it is very important to determine the binding site of reducing substrates on peroxidases. However, only a few X-ray crystallographic studies have been made on peroxidases which complexes with aromatic compounds. Crystal structures of aromatic substrate complexes with class I peroxidases have not yet been reported. The well-studied cases are the ARP and horseradish peroxidase isoenzyme C (HRPC), which belong to the class II and class III peroxidases, respectively. The crystal structure of ARP in complex with Benzohydroxamic acid (BHA) was obtained, showing that BHA binds to ARP in the distal heme pocket (Figure 7B) (Itakura et al., 1997). The benzene ring is located at the entrance of the heme cavity and parallel to the heme plane. All three functional groups of BHA are involved in hydrogen bonds with the distal amino acid residues histidine, arginine and proline (Itakura et al., 1997). Structures of HRPC-BHA complex and HRPC-CN Ferulic (FA) complex revealed a similar aromatic binding site as that found in ARP-BHA complex (Figure 7A) (Henriksen et al., 1999); (Laberge et al., 2001). BHA is a reducing substrate of ARP, a class II peroxidase, but not a good substrate of KatG. However, the structure of BHA is similar to that of INH containing a benzene

ring and an amine hydroxyl group (Figure 7C). It has been speculated that INH binds near the  $\delta$ -meso edge of the heme in a similar position to BHA in the ARP-BHA and HRPC-BHA crystal structures (Bertrand et al., 2004).

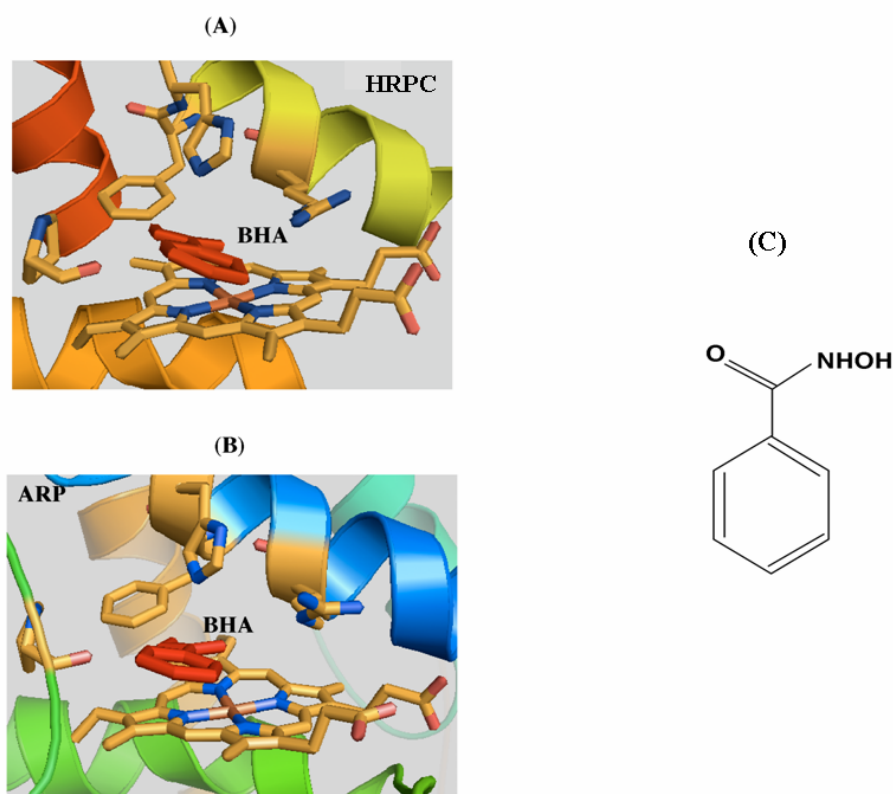


Figure 7. Substrate binding site in HRPC-BHA and ARP-BHA structure complexes. (A): HRPC-BHA; (B): ARP-BHA; (C): Structure of Benzohydroxamic acid (BHA). The figure is constructed using PyMol. HRPC: horseradish peroxidase isoenzyme C; ARP: *Arthromyces ramosus* peroxidase; BHA: Benzohydroxamic acid, colored red.

## **Brucellosis and *Brucella abortus***

### ***Brucellosis***

Brucellosis, like tuberculosis, is a chronic granulomatous infection caused by intracellular bacteria *Brucella sap* and requires combined prolonged antibiotic treatment. It is the most frequent human zoonosis, a human infection of animal origin (Young 1983). The most incidences have been reported from the Middle East and India (Ficht 2003). Transmission of brucellosis to humans occurs through the consumption of infected animal-milk products, direct contact with infected animal parts and the inhalation of *Brucella* aerosolized particles. Bacteria that have entered the human body and have been taken up by local tissue lymphocytes are transferred through regional lymph nodes into the circulation system and spread throughout the body (Harmon et al., 1988).

The disease is characterized by acute fever, undue fatigue, anorexia, weight loss, headache, and arthralgia. The most common complication caused by brucellosis in human is osteoarticular disease including peripheral arthritis, sacroiliitis, endocarditis, and spondylitis and several neurological disorders (Young 1983). Brucellosis has been proposed as a cause of reactive arthritis as well (Ariza et al., 1993). In most host species, the disease primarily affects the reproductive system, resulting in the loss of productivity in animals. Brucellosis presents a substantial risk of testicular inflammation in men and spontaneous abortion in pregnant women (Khan et al., 2001; Navarro-Martinez et al., 2001).

Treatment of human brucellosis involves a combination of antibiotics that can penetrate macrophages and act in the acidic intracellular environment. The treatment recommended by the WHO for acute brucellosis in adults is rifampin and doxycycline daily for a minimum of six weeks (WHO 1986). There is no human brucellosis vaccine available. Brucellosis vaccines for animal use are live attenuated vaccines, which show a residual virulence and cause disease in human (Banai et al., 2002).

### ***Brucella spp.***

Members of the bacterial genus *Brucella* are Gram-negative facultative extracellular/intracellular bacteria that cause infections in a broad range of mammals (Acha and Szylres 1980; Corbel 1997). *Brucella* belongs to the  $\alpha 2$  subdivision of the proteobacteria, along with *Ochrobactrum*, *Rhizobium*, *Rhodobacter*, *Bartonella*, and *Agrobacterium* (Moreno et al., 1990). Based on their host preference, the *Brucella* genus have been classified into six nomenclature species: *B. abortus* (cattle), *B. canis* (dogs), *B. melitensis* (sheep, goats), *B. neotomae* (desert wood rat), *B. ovis* (sheep), and *B. suis* (swine, reindeer) (Corbel 1984). All *Brucella* species seem to have arisen from a common ancestor (Moreno and Moriyon 2002). *B. melitensis*, *B. abortus* and *B. suis* can cause brucellosis in humans, leading to chronic disease such as orchitis, spondylitis, arthritis and Mediterranean fever (Ariza et al., 1995). *B. abortus* causes bovine brucellosis, a major disease in cattle, leading to abortion during the last trimester of gestation.

### ***Brucella pathogenesis***

*Brucella*, a facultative extracellular/intracellular pathogen that survives and replicates inside both phagocytic and nonphagocytic host cells, is able to penetrate target cells by inducing a local rearrangement of the host-cell plasma membrane around the invading bacteria (Pizarro-Cerda et al., 1999). Upon cell contact, the bacteria are internalized via complement and Fc receptors in the macrophages and monocytes through activation of small GTPases of the Rho subfamily (Harmon et al., 1988; Guzman-Verri et al., 2001; Chaves-Olarte et al., 2002). Treatment with nocodazole or cytochalasin D impairs the internalization of the bacteria, suggesting that both microtubules and the actin cytoskeleton are necessary for entry (Pizarro-Cerda et al., 1999; Guzman-Verri et al., 2001). Once brucellae invade mucosa, phagocytes ingest the bacterium and the majority of brucellae are rapidly eliminated by phagolysosome fusion. Of those surviving, some are relocated to early phagosomes where they avoid fusion with late endosomes and lysosomes (Arenas et al., 2000). It was suggested that *Brucella* is ingested through a discrete recruitment of actin filaments in HeLa cells (Gorvel and Moreno 2002). Most of the ingested Brucellae are relocated to the endoplasmic reticulum by the autophagocytic route in HeLa cells, whereas only a few bacteria are directed to phagosome (Comerci et al., 2001).

### ***Virulence Factors in Brucella***

In contrast to other pathogenic bacteria, the classical virulence factors such as exotoxins, cytolysins, capsules, fimbria, flagella, plasmids and the cellular receptors that are involved in attachment and entry of the bacteria into host cells are not known in *Brucella*. It has been demonstrated that there are specific molecules participating in *Brucella* binding to host cells. *Brucella* binds to the cellular spikes in cells treated with *Clostridium difficile* TcdB toxin, suggesting the participation of adhesion plaques (Guzman-Verri et al., 2001).

The ligand(s) implicated in the internalization process must be widespread since *B. abortus* is able to invade a broad range of mammalian cell lines (Detilleux et al., 1990; Pizarro-Cerda et al., 1998). Lipopolysaccharide (LPS), a major component of the outer membrane of gram-negative bacteria, has been implicated in the bacterial virulence (Freer et al., 1996). The entrance of *Brucella* by non-professional-phagocytes is also suppressed by inhibitors of energy metabolism such as iodoacetate and dinitrophenol, inhibitors of receptor-mediated endocytosis and cyclic-AMP (Gorvel and Moreno 2002). Invasion of *Brucella* into epithelial cells was inhibited by clostridial toxins, a GTPase inhibitor (Ferreira et al., 2002).

Genomic approaches used in the infected macrophage studies identified some genes implicated in the virulence of *Brucella* (O'Callaghan et al., 1999; Sieira et al., 2004). The first identified virulence determinant in *Brucella* was the *virB* operon, which codes a type IV secretion system that is responsible for the injection of effectors into the

cytoplasm of infected cells (O'Callaghan et al., 1999; Delrue et al., 2001; Boschirolì et al., 2002a; Boschirolì et al., 2002b; DelVecchio 2002).

It has been demonstrated that internalization (cell entry) and intracellular trafficking are two independent events during *B. abortus* infection in non-professional phagocytes (Pizarro-Cerda et al., 1998). The recent discovery of a type IV secretion system in gram-negative bacteria has been described to control the intracellular trafficking of *Brucella* but not the internalization to host cells (Comerci et al., 2001; Delrue et al., 2001). In infected hosts, *Brucella* reside in the endoplasmic reticulum and survive intracellularly under the control of the VirB type IV secretion system within macrophages (Celli and Gorvel 2004). However, the molecular mechanisms that regulate those processes are still poorly understood. It has been speculated that the type IV secretion system may export bacterial effectors. These effectors are able to modulate the biogenesis pathway of the *Brucella*-containing vacuole (BCV), allowing the BCV to mature into a replication-permissive organelle (Celli and Gorvel 2004). Vacuoles containing virB mutants are deficient in full maturation and are unable to sustain fusion-proficient interactions with the ER (Comerci et al., 2001; Celli and Gorvel 2004).

#### **Type IV Secretion System (T4SS)**

The T4SS is medically important, due to virulence-gene spread, genome plasticity and the alteration of host cellular processes during infection (Ochman et al., 2000; Ding et al., 2003). The T4SS secretion machinery plays essential roles in many pathogenic bacteria such as *Legionella* (Nagai and Roy 2001; Nagai et al., 2002), *Bordetella*



(Covacci and Rappuoli 1993; Weiss et al., 1993), *Helicobacter* (Segal et al., 1999; Comerci et al., 2001) and *Brucella* (Baron et al., 2002; Boschirolì et al., 2002a). In the past decade, the type IV family has expanded considerably, and many new VirB/D4 systems were discovered through genetic screens or genome sequencing.

### ***Secretion Systems in Gram-negative Bacteria***

At least five major independent mechanisms of protein secretion exist in the gram-negative bacterial species, namely type I, II, III, IV and V (Stathopoulos et al., 2000).

The type I secretion system (TOSS) or ABC (ATP-binding cassette) secretion systems are involved in multidrug efflux and toxin export (Andersen 2001). ABC transporters are classified as importers and exporters depending on the direction of the substrate translocation. The type I export apparatus consists of two hydrophobic membrane spanning domains (MSDs), which allow the translocation of the substrate through the membrane, and two cytoplasmic nucleotide binding domains (NBDs), which bind to ATP and couple ATP hydrolysis to drive the transport process (Braibant et al., 2000).

The type II secretion system (T2SS) is defined as the main terminal branch (MTB) of the Sec-dependent General Secretion pathway (GSP) (Filloux et al., 1998). All proteins secreted via a type II secretion pathway are synthesized with an N-terminal signal peptide. This pathway is responsible for secretion of extracellular proteins and toxins by a wide variety of gram-negative bacteria.

The type III secretion system (T3SS) was first identified in pathogenic *Yersinia spp.* for Yop proteins secretion and lately has been found in several mammalian and plant pathogens (Hardt and Galan 1997; Mecsas et al., 1998; He et al., 2004; Tampakaki et al., 2004). The type III secretion system translocate effector molecules across the inner and outer membranes in a Sec-independent fashion (Blocker et al., 2001). Type III secretion is activated by bacterial contact with host cells and is capable of translocating effectors through a large secretion apparatus into the cytosol of target eukaryotic cells (Hueck 1998).

A macromolecular translocation system ancestrally related to the conjugal transfer system is referred as type IV secretion system (T4SS) (Christie and Vogel 2000). Many pathogenic bacteria use T4SS to translocate proteins and DNA-protein complexes to prokaryotic and eukaryotic cells (Christie and Vogel 2000; Hofreuter et al., 2000; Cascales and Christie 2004; Sexton et al., 2004). Members of this family include those involved in bacterial conjugation, pathogenic transfer of DNA, and the secretion of protein virulence factors. Most of the type IV effector translocation systems inject their substrates directly into the eukaryotic cytosol. This type of translocation is a dominant virulence mechanism of the phytopathogen *Agrobacterium tumefaciens*, and of several medically important pathogens, including *H. pylori*, *Brucella spp.* and *Bartonella spp.* (Figure 8).

Type V secretion systems include the autotransporter system (type Va or AT-1), the two-partner secretion pathway (type Vb), and the recently described type Vc system (also termed AT-2) (Sopasakis et al., 2004). Proteins secreted via these pathways have

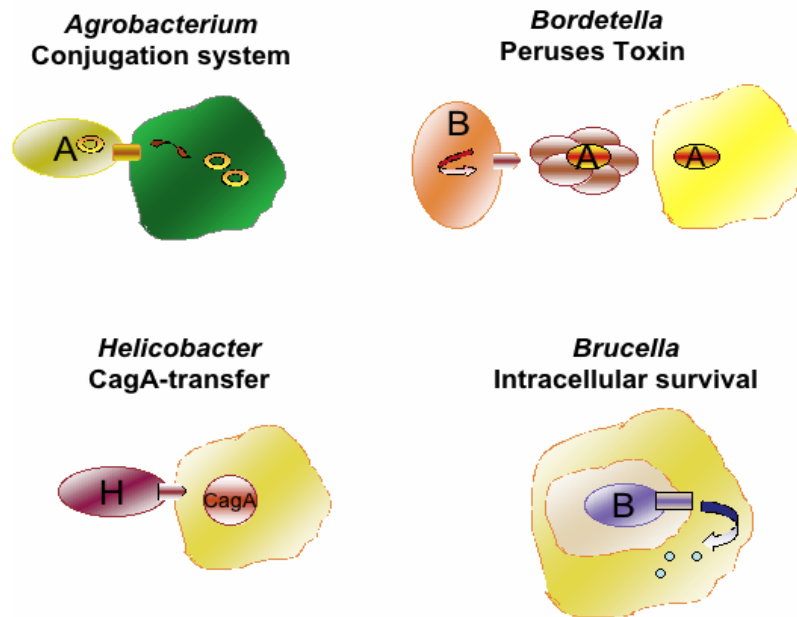


Figure 8. Examples of medically important pathogens that use Type IV secretion systems (T4SS) to translocate effector molecules and virulent factors into host cells.

similarities in their primary structures as well as striking similarities in their modes of biogenesis.

### *Classification of T4SS*

The T4SS have been classified into three subfamilies based on function: (1) conjugation systems mediating DNA transfer to recipient cells by cell-to-cell contact; (2) the effector

translocation system that transfers effector molecules to eukaryotic target cells; and (3) ‘DNA uptake or release’ systems mediating the exchange of DNA with the extracellular milieu (Cascales and Christie 2004). Most conjugation and effector translocation systems transfer DNA, DNA-protein complexes, or protein substrates by a cell-contact-dependent mechanism. The ‘DNA uptake or release’ system delivers DNA substrates to extracellular milieu, as in the F plasmid conjugation system of *Neisseria gonorrhoeae*, or acquires DNA substrates from the extracellular environment as that of the DNA uptake mediated by *Helicobacter pylori* competence system (Hofreuter et al., 2000; Hofreuter et al., 2001; Hofreuter et al., 2003).

Besides the classification schemes based on function, the T4SS have been grouped as type IVA, type IVB, and ‘other’ (Christie and Vogel 2000). The conjugation system comprises the largest type IVA subgroup, sharing common ancestries with the *A. tumefaciens* VirB/D4. Several medically important pathogens including *Helicobacter pylori*, *Bordetella pertussis*, *Brucella spp.*, and *Bartonella spp* (Ding et al., 2003), are classified into the type IVA. The type IVB is represented by the plasmid Collb-P9 Tra and the Dot-Icm of *Legionella pneumophila*.

### ***Subunits of the Multiprotein Complexes in T4SS***

Bacterial type IV secretion systems are multiprotein complexes composed of up to 11 proteins named VirB1 to VirB11 (Figure 9). Protein complexes of T4SS can be grouped into three major groups based on their function: the pilus at the bacterial surface (VirB2

and VirB5); a pore that spans the membrane (VirB3, VirB6, VirB7, VirB8, VirB9, and VirB10); and two ATPases (VirB4 and VirB11). The transporter forms a secretion channel and often a pilus structure that spans from the inner membrane of the bacterium through the outer membrane and into the extracellular space (Christie 2004). The pilus is composed of the major subunit VirB2 and the minor subunit VirB5. Other VirB proteins are believed to form the remainder of the transport apparatus to connect the pilus to the outer membrane and may form a continuous bridge from the outer membrane to the inner membrane of the bacterium (Christie and Cascales 2005).

VirB1 is a periplasmic protein that is processed to a secreted C-terminal fragment. It commonly associates with macromolecular surface structures as pili and flagella in the T2SS, T3SS and T4SS (Christie and Cascales 2005). VirB1 was identified as a putative lytic transglycosylase. Such lysozyme-like activity has been proposed to be important for hydrolysis of peptidoglycan and the proper formation of a channel that is filled by the other VirB proteins (Mushegian et al., 1996). In *Brucella abortus*, VirB1 is dispensable for T4SS function (den Hartigh et al., 2004).

VirB2 is the major subunit of the pili and an essential component of the secretion channel (Berger and Christie 1994). It locates to both membranes and the periplasm. VirB2 contains an unusually long signal peptide (~5 kDa). Cleavage of the signal peptide results in a small, hydrophobic polypeptide containing conserved multiple Gly residues dispersed along the polypeptide. This mature VirB2 of *A. tumefaciens* undergoes a unique cyclization reaction through formation of a covalent bond between the N-terminal Asp and C-terminal Glu residues (Sagulenko et al., 2001). The cyclized

pilins serve as the building blocks for pilus polymerization and stabilize the pilus structure in *A. tumefaciens* (Haase and Lanka 1997; Lai and Kado 1998). However, it was reported that VirB2 from *E. coli* do not undergo cyclization (Lai and Kado 1998; Lai 2002). There is no ultra structural information for any T4SS pilin subunit yet.

VirB3 is an essential virulence protein (Berger and Christie 1994), which localizes predominantly to the outer membrane. VirB3 has a short polypeptide chain with one or two TMS near the N- terminal (Jones, Shirasu et al. 1994). Studies have shown that the VirB3 subunits assemble as a functional complex with the VirB4 ATPase at the inner membrane (Christie and Cascales 2005).

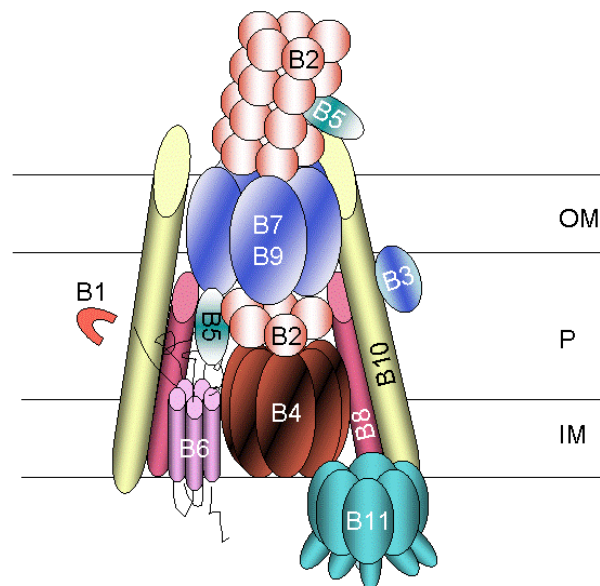


Figure 9. Subunits of the multiprotein complexes in T4SS. OM: outer membrane; P: periplasma; IM: inner membrane. The figure is constructed base on the protein-protein interactions detected by the yeast two hybrid systems (Christie 2004).

VirB4 and VirB11 are inner membrane-associated proteins, and VirD4 is a cytoplasmic protein, all of which possess ATPase activity (Krause et al., 2000). VirB4 and VirB11 contain a consensus Walker A box, the nucleotide-binding domain that is critical for transport (Atmakuri et al., 2004). These two proteins may provide the energy for the biogenesis of the transporter or perhaps for the transport process itself through the hydrolysis of ATP. VirB4 is the largest T4SS component (~90 kDa for a monomer molecule) and is essential for virulence (Dang et al., 1999). It is also highly conserved among T4SS components, i.e. 31% identity between *A. tumefaciens* and *B. suis*. It localizes at the base of a trans-envelope in the inner face of the cytoplasmic membrane. Its short N-terminal domain is exposed to the periplasm and interacts with VirB8 of the VirB5-VirB8 complex. Stabilized and properly oriented VirB5 forms complex with VirB2, a key complex in the pilus formation (Yuan et al., 2005), suggesting that VirB4 plays an important role in VirB2-VirB5 pilus formation. It has been shown that the interaction between VirB3 and VirB4 is required for complex localization in the outer membrane (Jones et al., 1994). VirB4 was also suggested to interact with other T4SS components such as VirB1, VirB8, VirB10, and VirB11 (Krall et al., 2002). VirB11 was identified as an essential component of T4SS and is the virulence factor of many pathogenic bacteria (O'Callaghan et al., 1999; Schmiederer and Anderson 2000; Baron et al., 2002; Cascales and Christie 2004; Christie 2004; Remaut and Waksman 2004; Sexton et al., 2004). It presents a good drug target for developing antimicrobial drugs because of its essential function in T4SS.

VirB5 subunits are exported to periplasm and localize extracellularly as components of the pili (Schmidt-Eisenlohr et al., 1999; Christie and Cascales 2005). VirB5 was shown to cofractionate with VirB2 indicating that VirB5 may be directly involved in pilus assembly (Schmidt-Eisenlohr et al., 1999). It has been proposed that VirB5 might function as a periplasmic chaperone to deliver pilin from the inner membrane reservoir to the outer membrane by a route independent of the virB-encoded mating channel (Lai et al., 2000).

VirB6 is a highly hydrophobic inner membrane protein with a periplasmic N-terminus, five TMS, and a cytoplasmic C-terminus (Jakubowski et al., 2003; 2004). It plays an important role in the assembly of a stable secretory apparatus in T4SS (Berger and Christie 1994; Hapfelmeier 2000; Jakubowski et al., 2003) and participates directly in substrate trafficking (Jakubowski et al., 2004). The large central periplasmic loop P2 of VirB6 was found to be responsible for DNA substrate translocation in *A. tumefaciens*. It has been proposed that loop P2 might adopt a specific secondary structure that is required for the substrate interaction (Jakubowski et al., 2004). The N-terminal and C-terminal regions were found to be essential for substrate transfer to the periplasmic and outer membrane-associated VirB2 and VirB9 (Jakubowski et al., 2004).

VirB7 subunits are small lipoproteins found in only a subset of the T4SS systems, although there are other type of lipoprotein common to T2SS and T3SS (Sagulenko et al., 2001). VirB7 of *A. tumefaciens* localizes extracellularly at the outer membrane and assembles as a homodimer through the formation of a disulfide bridge and then interacts



with VirB9 to stabilize several other VirB proteins (Baron et al., 1997; Sagulenko et al., 2001). N-terminal Cys15 of VirB7 plays an important role in lipid modification which is essential for pilus formation (Sagulenko et al., 2001). VirB7 from *H. pylori* HP0532 also localizes extracellularly, involving in the formation of a large sheathed filament in the Cag T4SS (Tanaka et al., 2003). Studies showed that extracellular VirB7 homodimer tightly associated with the T-pilus in *A. tumefaciens* and could be co-purified with VirB2 (Sagulenko et al., 2001).

VirB8 is found in the inner membrane of most type IVA systems. VirB8 was shown to interact with VirB1, the putative transglycosylase (Ward et al., 2002). A three-dimensional structure of a periplasmic fragment of *B. suis* VirB8 was solved (Terradot et al., 2005). The structure contains a large extended  $\beta$ -sheet and five  $\alpha$ -helices organized in a globular fold. VirB8 might contribute to the T4SS apparatus biogenesis by first recruiting the transglycosylase to punch holes in the peptidoglycan, and then recruiting the structural components of VirB9 and VirB10 to the site for assembly (Jakubowski et al., 2005).

VirB9 possess a cleavable signal peptide and is exported across the inner membrane to the outer membrane. The subunits are mostly hydrophobic and are located in the periplasm and outer membrane, forming a portion of the secretion channel that extends from the inner membrane to the outer membrane (Jakubowski et al., 2005). VirB9 of *A. tumefaciens* is composed of three functional domains, a highly conserved periplasmic N-terminal domain, a less conserved central domain, and a well conserved C-terminal domain. The N-terminal domain is required for both channel activity and pilus

biogenesis. The C-terminal domain possesses several TMS and may associate with the outer membrane. The C-terminal domain of the VirB9 forms a disulfide bridge with the VirB7 to form a heterodimer that stabilizes the VirB9 structure (Jakubowski et al., 2005). It has been shown that the VirB7-VirB9 heterodimer interacts with the inner membrane protein VirB10 to form a VirB7-VirB9-VirB10 complex (Cascales and Christie 2004; Jakubowski 2005). However, the interaction between VirB9 and VirB10 seems to be dynamic and driven by a conformational change in VirB10.

VirB10 is an inner membrane protein associated with proteins located in the periplasm. It possesses a proline-rich region, which is predicted to form an extended structure in the periplasm (Thorstenson et al., 1993). VirB10 also possess protein-protein interaction motifs, such as coiled-coils near the TMS and highly conserved hydrophobic residues near the C-terminal domain. It has been proposed that VirB10 interacts with other inner membrane proteins such as VirB8 and VirB4 (Das et al., 2000; Christie and Cascales 2005). VirB10 also interacts with the outer-membrane-associated VirB7-VirB9 dimer (Beaupre et al., 1997; Christie 2005). The crystal structure solved for a periplasmic fragment of *H. pylori* reveals an elongated  $\alpha$ -helical projection from a  $\beta$ -barrel (Terradot et al., 2004).

The *Brucella* virB operon contains one additional gene, virB12, which has been shown to be essential for virulence (Boschiroli et al., 2002b). VirB12 contains a lipoprotein consensus sequence and a predicted signal peptide. No homolog has been found in other classic T4SS (Boschiroli et al., 2002b). The function of this protein in either transport or virulence is unknown.

### ***Biogenesis of the T4SS***

A general T4SS assembly pathway was proposed and refined (Christie 2001) based on biochemical studies in *A. tumefaciens* VirB/D4 conjugation system. In the model, it was suggested that pilus formation initiates at the inner membrane and proceeds outward through the periplasm to the outer membrane. An alternative model suggests that the pilus subunits are translocated from the periplasm to outer membrane through a chaperone before the pilus complex formation (Christie et al., 2005).

Recently, a four-stage biogenesis pathway was proposed for the VirB/D4 T4SS: Stage I, core complex formation; Stage II, pilus-associated protein recruitment; Stage III, recruitment of VirB11 ATPase; and stage IV, the pathway bifurcation (Christie et al., 2005).

Stage I involves the formation of the core complex. The core complex containing VirB4, VirB7, VirB8, VirB9, and VirB10 subunits assembles across the cell envelope (Christie et al., 2005). It has been shown that the core subunits can be cofractionated as a large complex (> 500kDa) in the gel filtration columns (Krall et al., 2002). VirB7 and VirB9 are small outer membrane lipid protein participating in T-pilus assembly in *A. tumefaciens*. First, VirB7 assembles as a disulfide-cross-linked homodimer and then interacts with VirB9 to form VirB7-VirB9 hetero-multimers. Second, both the VirB7 homodimer localized at the outer membrane and the VirB7-VirB9 hetero-multimers interact with the bitopic inner membrane proteins VirB8 and VirB10 through contact with the VirB9 subunits (Anderson et al., 1996; Baron et al., 1997; Sagulenko et al., 2001).

Stage II involves the recruitment of pilus-associated proteins. The core complex recruits subunits VirB2, VirB3, and VirB5 for pilus assembly (Christie 2005). Recently, a network of stabilizing interactions for formation of a VirB2-VirB5 complex was identified (Yuan et al., 2005). VirB4 is the largest component of T4SS and forms a homomultimeric complex which is essential for virulence (Watarai et al., 2001). VirB4 was shown to interact with VirB1, VirB8, VirB10, and VirB11 (Ward 2002). VirB4 has been found to bind to the periplasmic domain of VirB8 and is required for the assembly of pilus-associated proteins with VirB3, VirB6, and VirB8 (Yuan et al., 2005). VirB4 binds to VirB8 and stabilizes VirB3 and VirB8. The stabilized VirB8 interacts with VirB5 in the periplasm. Stabilization of VirB5 and VirB3 through interaction with VirB6 enables VirB5 to complex with VirB2 and thereby impact pilus biogenesis (Hapfelmeier et al., 2000; Yuan et al., 2005).

Stage III is associated with the recruitment of VirB11 ATPase. VirB11 was shown to be essential for secretion channel formation and pilus production (Lai et al., 2000). VirB11 ATPase localizes at the cytoplasmic face of the inner membrane and supplies energy from ATP hydrolysis to drive organelle assembly and substrate translocation at the cell envelope (Rashkova et al., 2000). The cytosolic VirB11 homohexamer undergo ATP-dependent conformational changes that likely affect protein-protein interaction and the formation of the pilus subunits. It was proposed that VirB11 are recruited to the core structure, where they stimulate the formation of a transenvelope composed of an inner membrane platform that across the periplasm, and an outer membrane complex (Christie et al., 2005).

Stage IV is the pathway of the bifurcation. Stage IV is a bifurcation process in which the assembly pathway produces a pilus or a secretion channel (Christie 2005). It has been proposed that VirB2, pilin monomers, are added to the base of the nascent polymer of the stage III structure (Christie et al., 2005). The energy-consuming subunits, VirB4 and VirB11, would drive conformational changes required for channel gating. This process is most likely driven by energy supplied through VirB11 because the Walker A mutant of VirB11 shows disruption of pilus biogenesis in *B. suis* (Yuan et al., 2005). Other factors may also be required for channel activity, such as the substrate binding to the receptor (Christie et al., 2005).

### ***Models of the Translocation Pathway in T4SS***

Three working models have been proposed to describe the possible machine architectures and translocation pathway (Christie et al., 2005): (1) a one-step model using a transenvelope channel, (2) a two-step ‘ping-pong’ model for transferring substrates across the inner membrane to the outer membrane, (3) the ‘shoot and pump’ model, in which the substrates are recruited and translocated across the inner membrane through a protein export apparatus.

The first model involves recruitment of secretion substrates and transfers them through an inner membrane channel (Christie et al., 2005). It has been suggested that the energetic subunits, VirB4 and VirB11, would energize conformational changes required for channel gating (Middleton et al., 2005).

The ‘ping-pong’ model was proposed such that the T-DNA was recruited by VirD4 and transferred to the VirB11 chaperone (ping) where it was refolded and retro transferred back to VirD4 (pong) by VirB11 (Atmakuri et al., 2004). Next, VirD4 uses ATP energy to translocate the DNA-protein substrate across the inner membrane through interaction with VirB6 and VirB8 (Atmakuri et al., 2004).

The ‘shoot and pump’ model was initially proposed by Llosa to describe bacterial conjugation, suggested that two inner membrane translocases are involved in the translocation (Llosa et al., 2002). It postulated that VirD4 recruits the T-DNA to the secretion apparatus and then transfers only the relaxase component to VirB11, which unfolds the relaxase through a chaperone activity to deliver the relaxase across the inner membrane (shoot) through interaction with other VirB proteins (Atmakuri et al., 2004). Simultaneously, VirD4 uses ATP energy to drive the T-strand across the membrane (pump), releasing the particle to the secretion channel (Llosa et al., 2002; Atmakuri et al., 2004). *Brucella spp* lacks the VirD4 homolog, so the energy sources most likely are from either VirB4 or VirB11. Of these models, the ‘shoot and pump’ model is especially appealing. This model accommodates all experimental findings to date (Christie and Cascales 2005) .

### ***Effectors Translocation by the T4SS***

Although members of the type IV family share structural homologies, they display diversity in the nature of the substrates that they transport. *A. tumefaciens*, a plant pathogen causing tumorous growth in plant tissue, uses the type IV secretion system to

transfer T-DNA and several effector proteins to plant cells (Christie 2004). *Helicobacter pylori*, a causative agent of gastric pathologies such as peptic ulcer disease and gastric adenocarcinoma uses a related system to deliver the 145kDa CagA protein to mammalian cells. CagA is the only virulence protein shown thus far to be translocated by the *H. pylori* CagA T4SS. The translocated CagA undergoes tyrosine phosphorylation to form a cylindrical structure and seems to induce cytoskeletal rearrangements in the host cell (Segal et al., 1999). *Bordetella pertussis*, the causative agent of whooping cough, exports the six-subunit pertussis toxin (PT) across the bacterial outer membrane to the extracellular milieu and establishes contact with the mammalian cell (Baron et al., 2002). So far, it is not known how the T4SS in *Brucella spp.* recruit and translocate their effector molecules across the inner membrane.

The bacterial effectors of the secretion system of *Brucella* have not been identified yet. However, some surface exposed and secreted proteins were screened from *B. abortus* by an N-terminal protein-capturing system using the CAT fusion scan (Marchesini et al., 2004). Some fusions displayed notably reduced secretion levels in a virB mutant background, suggesting the requirement of a complete VirB apparatus for the secretion. Secretion of the fusion BvrR, a transcriptional regulator protein that is essential for *B. abortus* virulence (Sola-Landa et al., 1998), was found to be associated with intact VirB expression. Secretion of the N-terminal fragment of BvrR fused to CAT was diminished in virB1 and virB10 mutants (Marchesini et al., 2004). The *B. abortus* BvrS/BvrR system has been shown to play a role in the homeostasis of the bacterial membrane (Lopez-Goni et al., 2002). It has been proposed that modification

of LPS is responsible for the damages of the outer membrane in BviS/BviR mutants, causing severe attenuation in *B. abortus* mutant strains (Lopez-Goni et al., 2002; Manterola et al., 2005).

The flagellar hook protein (FlgE), an extracellular component of flagella, has been described as being secreted to the culture media of several bacteria species such as *Salmonella typhimurim* (Komoriya et al., 1999), *Bordetella bronchiseptica* (Tu et al., 2001), and *H. pylori* (Bumann et al., 2002). Secretion of CAT-fused FlgE is notably reduced in the virB1, virB10, and virB11 mutant background, respectively (Marchesini et al., 2004). It has been shown that the *Brucella* T4SS and flagellar apparatus are tightly regulated along the growth curve in growth media (Sieira et al., 2000). The expression and assembly of the flagella or pili of T4SS are both energy dispersive processes that require intricate regulation controls to allow their expression and assembling at the very precise steps of the infection (Muir and Gober 2002). A quorum sensing-related transcription regulator (vjbR) was proposed to regulate the expression of both virB operon and flagellar genes either during vegetative growth or during intracellular infection (Delrue et al., 2005).

Most of the type IV effector translocation systems inject their substrates directly into the eukaryotic cytosol. The *A. tumefaciens* T-DNA conjugation system and the *H. pylori* CagA translocation system are thought to export substrates in one step across the membrane directly to the eukaryotic cytosol. This type of translocation is now recognized as a dominant virulence mechanism of the phytopathogen *A. tumefaciens*, and of several medically important pathogens, including *H. pylori*, *L. pneumophila*,



*Brucella spp. and Bartonella spp.* A subfamily of the Ptl system of *B. pertussis* exports its protein substrate, pertussis toxin, independently of host-cell contact. The *Bordetella pertussis*, the causative agent of whooping cough, is thought to export pertussis toxin in two steps across the cell envelope to the extracellular milieu. Secreted holotoxin then binds to the mammalian cell membrane (Christie 2001).

## **CHAPTER II**

### **STRUCTURE DETERMINATION BY X-RAY CRYSTALLOGRAPHY**

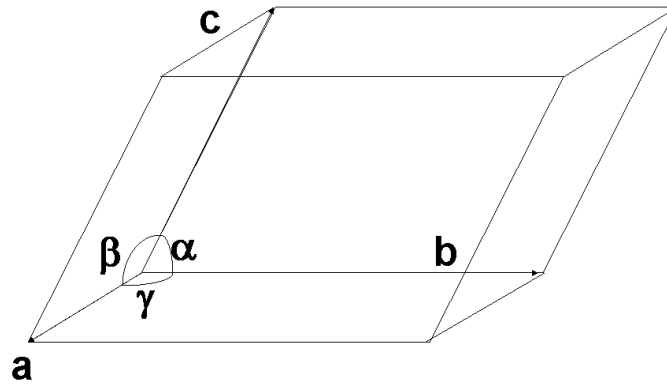
#### **Introduction**

Macromolecules are the major constituents of living cells. Proteins are the largest group of macromolecules and perhaps the most versatile of all biomolecules. Some proteins function as enzymes and others serve as structural elements, signal receptors, or transporters. Knowledge of the detailed three-dimensional structures of proteins and other macromolecules is vital to the understanding of cellular process and the functional roles of proteins/enzymes. X-ray crystallography techniques are widely used for the structural determination of macromolecules at atomic resolution. During the past decades, macromolecular X-ray crystallography has undergone dramatic development. Rapid progress in molecular biology, improved crystallization screens, more powerful synchrotron sources for data collection, high-speed computers and advances in computer software and programs have dramatically enhanced the efficiency of crystallographic structural determination and produced an exponential growth of the number of X-ray crystal structures solved. Of those 36,121 structures deposited in the Protein Data Bank (PDB) (by April 18, 2006), over 30,583 structures were solved by the X-ray crystallographic method. Continued advances in computing methods and technologies usher in the age of high-throughput structure determination.

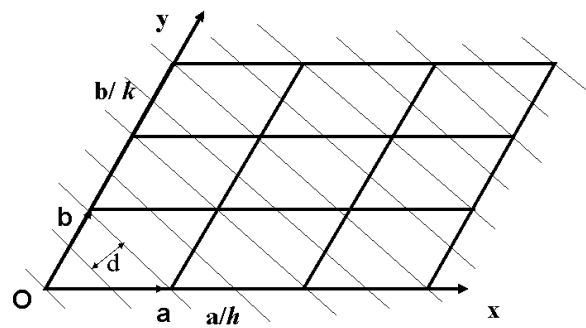
## Protein Crystals

A protein crystal is the result of the three-dimensional periodic packing of homogeneous protein molecules surrounded by solvent. The three-dimensional components of a crystal can be described as a repetition of identical unit cells (Rhodes 1993). In general, the unit cell is characterized by six parameters, three axial lengths  $a$ ,  $b$ ,  $c$  and three interaxial angles  $\alpha$ ,  $\beta$ ,  $\gamma$ . These six parameters are called unit cell parameters, which define a unit cell in the crystal lattice (Figure 10a). The vector in **a** direction is called the x-axis of the lattice; the y-axis is in **b** direction and the z-axis is in the **c** direction. The x-, y- and z-axes together form a coordinate system. Location of atoms within a unit cell can be described by their Cartesian coordinates  $x$ ,  $y$ ,  $z$ . The diffraction of x-rays by a crystal can be regarded as reflection against planes in the lattice. Many sets of these planes can be drawn through the lattice points. The planes in the same set are parallel and have the same perpendicular distance  $d$ . A set of lattice planes is determined by three indices  $h$ ,  $k$ ,  $l$  (also referred to as Miller indices). The planes cut the x-axis in **a**/ $h$ , y in **b**/ $k$ , and z in **c**/ $l$  sections (Figure 10b). The Miller indices  $h$ ,  $k$ ,  $l$  are integers that serve as the bases for the data processing.

The minimum free energy of packing and regular repeats in a crystal lattice results in a symmetric relationship between the molecules (Drenth 1999). There are seven three-dimensional coordinate systems that are used in describing crystals, including triclinic, monoclinic, orthorhombic, tetragonal, hexagonal and cubic. The triclinic crystals have the lowest symmetry and the cubic crystals have the highest symmetry. There are 230



(a) One unit cell in the crystal lattice



(b) Lattice plane in a two-dimensional lattice,  $h=2$ ,  $k=2$ .

Figure 10. Crystal unit cell and the lattice plane.

different ways to combine the allowed symmetry operations in a crystal, leading to 230 space groups (Deranth 1999).

Protein crystals form and grow in a supersaturated solution (Drenth 1999). In principle, there are four important determinants in protein crystallization. First is the purity of the protein. The purity requirement for protein crystallography is much more stringent in most cases. The more pure the protein is, the better the chance of crystal formation and growth. Second, a suitable solvent from which a protein can precipitate in crystalline form is selected. A solvent is usually a water-buffer solution. Third, the protein in solvent is brought to super saturation in which small nuclei form. Spontaneous nuclei formation is best achieved at a high degree of super saturation. However, to achieve crystal growth, super saturation should be kept at a low enough level to avoid formation of too many nuclei and too many small crystals (Drenth 1999). Fourth, crystals must grow to suitable size. In reality, protein crystallization is mainly a trial-and-error procedure.

There are various methods of growing protein crystals, all designed to increase the protein concentration in the solution slowly by slow evaporation, slow diffusion, or slow cooling. The most common method is vapor diffusion, including hanging drop diffusion and sitting drop diffusion. This method allows a saturated or nearly saturated solution to stand under conditions where the solvent evaporates slowly. The hanging drop method starts with a drop of protein mixed with precipitant suspended over a reservoir containing buffer and precipitant. The most commonly used precipitants are salt, high molecular weight polymers and organic solvent. When water diffuses from the drop to

the solution, the proteins in the drop reach a supersaturated condition for optimal crystal growth. The Microbatch method is another popular method to grow protein crystals. A drop of protein solution is put in inert oil and left to grow when the protein reaches its super saturation over time.

Once a crystallization condition has been identified, optimization may be needed in order to improve the size and quality of the protein crystal. Optimization is carried out by systematically changing the concentrations of the precipitants. Additives such as metals, small molecules and detergents may also be tested along with the optimized precipitants. In certain cases, pH screening can be used to optimize the protein crystals.

### **X-ray Diffraction**

The diffraction of X-rays by crystals was first discovered by Max-von in 1912, leading to one of the most fascinating development in life science. X-ray diffraction occurs as waves interact with a regular structure whose repeat distance is about the same as the wavelength of X-ray (Drenth 1999). When certain geometric requirements are met, X-rays scattered from a crystal can constructively interfere, producing a diffracted beam (Drenth 1999). In 1912, W. L. Bragg recognized a predictable relationship among several factors.

$$2d \sin \theta = n\lambda$$

where  $\lambda$  is the wavelength of the x-rays,  $d$  is the distance between successive lattice planes,  $n$  is an integer, and  $\theta$  is the angle between the incident beam and lattice plane.

When Bragg's Law is satisfied, constructive interference occurs, producing the respective reflections in the form of spots recorded on the image plate or CCD (charge coupled device area detectors) (Figure 11).

In x-ray crystallography, integrated intensities of the reflections are used to reconstruct the electron density map within the unit cell in the crystal by Fourier transformation with appropriate phase assignment. To achieve high accuracy in the reconstruction, a high degree of completeness as well as redundancy in diffraction data is necessary, meaning that all possible reflections are measured multiple times to reduce systematic and statistical error. The most efficient way to do this is by using an area detector that can collect diffraction data in a large solid angle.

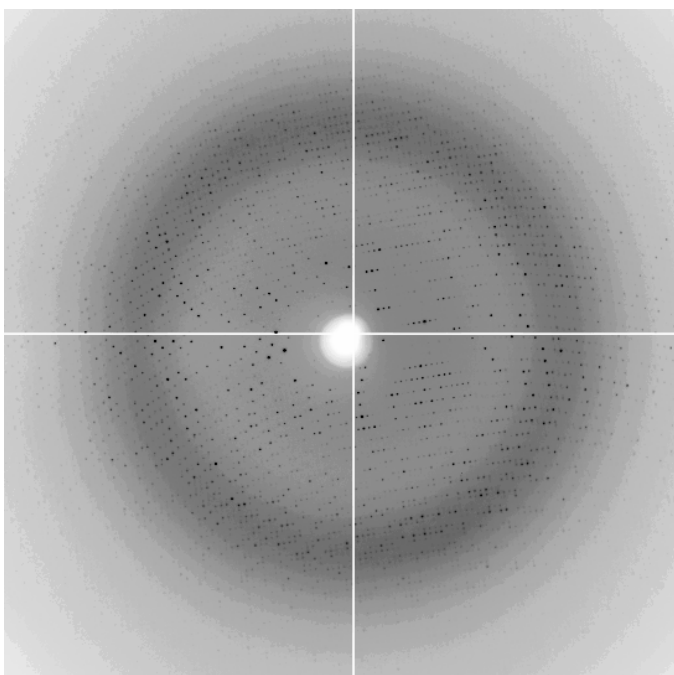


Figure 11. A single X-ray diffraction image generated from a protein crystal.

Two main pieces of hardware are required for the collection of X-ray diffraction data: an X-ray source and an X-ray detector. An X-ray generator in a home laboratory uses a rotating anode copper sealed in a tube. Cu produces K  $\alpha$  radiation at about  $\lambda = 1.541 \text{ \AA}$ . Synchrotrons are devices for creating circulating charged particles at nearly the speed of light. They generate high intensity radiation 10 to 1000 times stronger than that of a conventional X-ray tube. Synchrotron radiation allows the measurement of the weak diffracting amplitudes of protein crystals and for measurements at various  $\lambda$ . Radiation damage to protein crystals caused by synchrotron exposure can be minimized by flash cooling the crystal to cryogenic temperatures.

Charged Coupled Devices (CCD) and Image Plate (IP) detectors are the best-known 2D detectors that have high quantum efficiency, high saturation, and high stability (Drenth 1999). Image plates are coated with a thin layer of inorganic storage phosphor on their surface. X-ray photons excite electrons in the material to higher energy levels causing fluorescent light illumination. The light emitted is proportional to the number of photons from X-ray diffraction exposed to the particular area of the image plate. CCD is an electronic device that detects X-ray photons on a two-dimensional surface and processes the signal immediately after the detection. It provides the capability for faster, more accurate, automated data collection for use in macromolecular crystallography. It has enhanced efficiency for measuring diffraction patterns from crystals of macromolecules, especially at high resolution, when the X-ray intensities are weak (Walter et al., 1995). The output of the data collection consists of raw intensity data for each frame along with detector parameters.



## Data Processing

The ultimate goal of an X-ray diffraction experiment is to determine the 3-D structure of a protein molecule. The first step in data processing is to determine the unit cell parameters and space group symmetry of the crystal. It is crucial to define the space group of a crystal of unknown structure correctly because the subsequent calculations are based on the relationships implied by the space group symmetry.

There are several major steps involved in data analysis and data reduction from a single crystal. The first step is to visualize and preliminarily analyze the original unprocessed data, such as the shape of the diffraction spots, ice-rings, and twinning. Second, the diffraction pattern of a crystal has to be indexed before the refinement of the crystal and detector parameters. The intensity of each reflection in a single frame (or a few frames) has to be identified by its  $h$ ,  $k$ , and  $l$ , based on the cell parameters. Next, all diffraction maxima are integrated, scaled, refined and statistically analyzed. The HKL2000 (Otwinowski and Minor 1997), Mosflm, and CrystalClear are the most popular programs that are used for the data processing. The HKL2000 suite program contains XDISPLAY for image display and measurement, DENZO for auto-indexing, refinement and integration, SCALEPACK for data scaling, and HKLINT for the GUI interface. The output of the processing data (scaled data) is a list of all reflections with their Miller indices  $h$ ,  $k$ ,  $l$  and corresponding intensities and systematic errors.

### Phasing Method ----- Molecular Replacement

The intensity of the diffracted beam ( $h\ k\ l$ ) is proportional to the square of the amplitude of the structure factor  $F(h\ k\ l)$ . The structure factor is a function of the electron density distribution in the unit cell. The result of an X-ray structure determination is the electron density in the unit cell:

$$\rho(x, y, z) = \frac{1}{V} \sum_h \sum_k \sum_l F_{hkl} (hx + ky + lz + \alpha_{hkl})$$

In the equation,  $\rho(x,y,z)$  is expressed as a Fourier transformation of the structure factors  $F(h\ k\ l)$ .  $\rho(x,y,z)$  is the electron density at the point with coordinates ( $x,y,z$ ) in the unit cell,  $V$  is the volume of the unit cell,  $\alpha_{hkl}$  is the phase angle of the reflection ( $h, k, l$ ). Structure factors are directly related to the intensity  $I(h,k,l)$  of the corresponding reflection  $h, k, l$ :

$$I_{(hkl)} = |F_{hkl}|^2 \text{LP A}$$

where  $I_{hkl}$  is the integrated data in the form of intensities for each of the Bragg reflections,  $F$  is the structure factor,  $\text{LP}$  is a combined geometry and polarization factor and  $A$  is an absorption correction factor. The phase angles  $\alpha_{hkl}$  cannot be measured directly in the diffraction experiment. However, the phase information is required for solving the crystal structures. Two common methods, molecular replacement (MR) and multiple wavelength anomalous dispersion (MAD), have been used frequently to obtain the phase information necessary for solving the crystal structures.

Molecular replacement can be used to get initial phases if the structure of its homologous protein has been solved. In general, two major steps are used in the Molecular Replacement are known as the rotation and translation functions. The rotation function allows the correct orientation of the search molecule to produce maximal overlap with the target structure by comparing the Patterson self-vectors of the known and unknown structures at different orientations of the search model (Drenth 1999). The rotation matrix calculated from the rotation search can be applied to the coordinates of the search molecule. The resulting model then can be used for the translation function to correctly determine related symmetry elements of the target crystal.

The success of the MR phasing strategy is mainly dependent on the similarity between the search model and the structure to be determined. The higher the sequence similarity to the search model, the higher the probability that the structure will be solved by MR phasing. In general, a 30% identity to the search model is considered minimal in finding the right solution by using MR phasing.

MOLREP developed by Alexei Vagin is an automated program for molecular replacement (Vagin and Teplyakov 1997). It is especially advantageous for the rotation function search when different unit cells are present in the search model and the unknown structure. The orientation and position of the model obtained from the rotation and translation search can be refined by the rigid-body refinement already incorporated in MOLREP. The best solution is written out based on the highest correlation coefficient.

Phaser is a crystallographic program for phasing macromolecular crystal structures using maximum likelihood algorithm (Read 2001). The Automated Molecular Replacement in Phaser is a very robust program for solving most structures by using relatively simple strategies.

EPMR is another crystallographic molecular replacement program developed by Charles Kissinger (Kissinger et al., 1999). The program finds molecular replacement solutions by using an evolutionary search algorithm (Kissinger et al., 1999). Once an initial set of random solutions is generated, the correlation coefficient between the observed structure factor  $F_o$  and the calculated structure factor  $F_c$  is calculated for each orientation based on the search model. A fraction of the highest scoring orientations are used to generate a set of new orientations by applying random alterations to the orientation angles and translations. The correlation coefficients of the new solutions are calculated and the search runs to the next cycle. At the end of this evolutionary optimization, a local rigid-body refinement is performed and the best solution is written out.

### **Phasing Method -----Multiple Wavelength Anomalous Dispersion (MAD) Phasing**

The anomalous scattering method has been widely used for solving protein structures. The anomalous scattering by an atom is due to the fact that its electrons cannot be regarded as completely free electrons (Hendrickson 1991). If heavy atoms are present in a protein structure, the consequence of their anomalous scattering results in the

differences in intensities measurements between a reflection  $h\ k\ l$  and its Bijvoet pair  $\bar{h}\ \bar{k}\ \bar{l}$ . The heavier the atom, the stronger the effect of the anomalous scattering becomes. Wide varieties of elements have been used as anomalous scatter makers. Selenium is the most often used marker atom for MAD phasing because of the successful production of selenomethionyl (SeMet) proteins (Hendrickson et al., 1990). The advantage of MAD phasing is that it exploits additional anomalous redundancy not only by using anomalous (Friedel- or Bijvoet-) differences within each data set, but also by employing dispersive anomalous differences between data sets recorded under different wavelengths (Hendrickson 1991).

Anomalous scattering or dispersion occurs when the wavelength of the incident X-rays is near that of an absorption edge of the heavy metal. The X-ray absorption edge-scan for the anomalous marker atom (Se in this case) defines optimal wavelengths in the MAD experiments. For a MAD experiment with a single absorption edge, three wavelengths can be chosen, a peak point at the wavelength with maximal  $f''$ , an inflection point with maximal  $f'$ , and a remote point that is away from the absorption edge.

The X-ray scattering power will depend on the number of electrons in the particular atom. The X-ray scattering power of an atom decreases with an increasing scattering angle and is higher for heavier atoms. Its anomalous scattering can be written as

$$f_{\text{anom}} = f + \Delta f + if''$$

$\Delta f$  is the change in the electron scattering factor along the horizontal axis in the Argand diagram and  $if''$  along the vertical axis.

The structure factors  $F_{PH}(h\ k\ l)$  and  $F_{PH}(\bar{h}\ \bar{k}\ \bar{l})$  for the heavy atom derivative of a protein are different and have a different phase angle due to their anomalous scattering.

$$\Delta|F|_{anom} = \{|F_{PH}(h\ k\ l)| - |F_{PH}(\bar{h}\ \bar{k}\ \bar{l})|\} f'/2f''$$

$\Delta|F|_{anom}$  is the difference between the amplitudes of the structure factor for the reflections  $hkl$  and  $\bar{h}\ \bar{k}\ \bar{l}$  (Bijvoet or Friedel pairs), scaled up with the factor  $f'/2f''$ .

The changes in the intensities of reflections caused by the anomalous scattering are very small. Differences of a few percent can be observed between  $|F(hkl)|$  and its Friedel opposite  $|F(-hkl)|$  at the same wavelength (Bijvoet differences) and the same  $|F(hkl)|$  at different wavelengths (Dispersive differences). To obtain a usable anomalous signal, the data must be measured with a significantly better (lower) noise level, which can be determined by deriving the Bijvoet ratios from measured centric reflections. By comparing the Bijvoet differences and the Dispersive differences, initial phase information can be obtained for solving the structure of the protein crystal.

SHELXD (Schneider and Sheldrick 2002) and HYSS (Gross-Kunstleve and Adams 2003) direct methods can be used for solving heavy atom substructures.

The quality of the scaled data need be evaluated using XTRIAGE (Zwart 2005) before the SHELXD or AutoSHARP phasing. The analysis includes unit cell parameter, systematic absences and the determination of the space group and the maximum resolution for which significant anomalous signal is present. XPREP or HYSS can generate an input file (.ins) and an hkl file to be used in SHELXD later.

SHARP/AutoSHARP and SOLVE/Phaser are automated programs for solving macromolecular structures based on reduced, merged and scaled data from SAD,

SIR(AS), MIR(AS) and MAD experiments (Online [www.globalphasing.com/SHARP](http://www.globalphasing.com/SHARP)).

The program calculates phase probability distributions for all reflections in the dataset and can detect disordered sites using likelihood-based residual maps.

### **Model Building and Refinement**

Once a structure solution has been obtained either through molecular replacement or MAD phasing, the electron density map can be calculated. The final step of model building and refinement can proceed based on the calculated map.

The initial calculated electron density map from either MR or MAD is either biased or incorrect. Errors have been introduced during data collection, data processing and phasing. Refinement allows us to obtain the calculated structure factor ( $F_c$ ) and compare it with the observed structure factor ( $F_o$ ) from the X-ray experiment. The quality of the structure model is indicated by a residual factor (R-factor) of which is based on following equation:

$$\text{R-factor} = \frac{\sum |F_o| - |F_c|}{\sum |F_o|}$$

The higher the similarity between the observed and calculated structure factors, the lower the value of the R-factor and the better the quality of the model. One of the aims of model building and refinement is to bring the R-factor to its lowest value.

During model building, the structure model is manipulated using graphic interfaces to adjust the atomic positions based on the electron density maps.

XtalView is a complete package for building the molecular model (McRee 1999). It has a simple but comprehensive windows based interface. Xtalview contains XtalMgr, the central control program that launches all other applications and organizes the files, and the Xfit user interface, a model-building and map viewing program. Manual fitting programs such as Xtalview also allows for changes to the structure that are outside the radius of computational convergence. For example, the rotamer search can fit side chains into the electron densities. Once the correct rotamer is chosen, the refinement program in Xtalview can re-adjust the local main chain conformation correctly.

Xtalview also allows individual change of amino acid residues into correct sequence and refines locally using geometric and real space refinement based on the electron density map.

The resulting model is subjected to computational refinements to localize atoms to the most probable positions by applying constraints and restraints to some parameters. For example, stereochemical restraints are incorporated in most refinement programs. Bond lengths, bond angles, torsion angles and other chemical properties used in restrained refinement are referred as stereochemical restraints. Constraints include anisotropic thermal parameters used in the refinement (Winn et al., 2003).

REFMAC5 is based on the maximum likelihood refinement formalism to minimize the coordinate parameter differences (Murshudov et al., 1997). The likelihood function for macromolecular structures including prior phase information and experimental standard uncertainties or possibilities is implemented. The overall parameters of likelihood and the atomic parameters are refined sequentially in the program. The



indicators of a successful refinement include the value of figure of merit (FOM), R factor and R free, and the correlation between maps generated from the model and the final map derived from refined structural coordination.

The maps derived from MR phases can be significantly biased because the reflection phase angles ( $\alpha_{hkl}$ ) are not directly measured. The SHAKE&WARP is a program that combines multiple bias-reduction methods into a single web service. The strategies include omitting parts of the model, the perturbation of the model coordinates, and, most importantly, the averaging of six maps which resulted from differently perturbed starting models (Perrakis et al., 2001). The improved unbiased map can be used to further refine and improve the model.

The quality of the refined structure can be further checked with program PROCHECK (Laskowski et al., 1993). PROCHECK is a validation program used to assess the geometry of the residues in a given protein structure compared with stereochemical parameters derived from well-refined, high-resolution structures. The checks also make use of "ideal" bond lengths and bond angles derived from small molecule structures in the Cambridge Structural Database, CSD.

# CHAPTER III

## STRUCTURAL STUDIES OF *Mtb*KatG, KatG[S315T] MUTANT, AND *Mtb*KatG COMPLEXED WITH KCN AND INH\*

### Introduction

*M. tuberculosis* KatG is an 80 kDa bifunctional enzyme exhibiting a predominant catalase activity and also a substantial peroxidase activity with broad specificity (Heyme et al., 1993) (Welinder 1992a) (Zhang et al., 1992). It uses a single active site to catalyze both catalase and peroxidase reactions and to remove hydrogen peroxides from the biological system efficiently to protect bacterial cells from damage due to reactive peroxide(s) generated by host macrophages (Manca et al., 1999). The peroxidase function of KatG is believed to play a critical role in the activation of INH (Zhang and Young 1993). Most INH resistance in clinical isolates results from mutations in the *katG* gene (Saint-Joanis et al., 1999), leading to the elimination or reduction of catalase or peroxidase activity (Heym et al., 1995; Musser 1995; Rouse et al., 1995; Rouse et al., 1996), resulting in lack of IHN activation. Transformation of *M. smegmatis* and *M.*

---

\*Part of the data reported in this chapter is reproduced in part with permission from "Hydrogen peroxide-mediated isoniazid activation catalyzed by *Mycobacterium tuberculosis* catalase-peroxidase (KatG) and its S315T mutant." (2006) Zhao X, Yu H, Yu S, Wang F, Sacchettini JC, Magliozzo RS, Biochemistry **45**(13): 4131-40. Copyright 2006 American Chemical Society.

*tuberculosis* with wild-type katG gene restored INH susceptibility to resistant isolates (Zhang et al., 1993), confirming that the product of KatG enzyme participated in INH action.

Some mutations in KatG associated with INH resistance result in a significant decrease in its catalase or peroxidase activity, while others show no significant change in enzyme activity (Saint-Joanis et al., 1999) (Jakopitsch et al., 2003b). The most common mutation accounting for over 50% of INH-resistance in clinical isolates is the S315T substitution (van Soolingen et al., 2000) (Saint-Joanis et al., 1999). The S315T mutant produces only moderately reduced catalase or peroxidase specific activity in vitro (2-fold and 4-fold, respectively), which does not explain 200-fold increase in MIC for strains carrying this mutation (Heyme et al., 1993). Furthermore, *M. tuberculosis* strains carrying the S315T mutation maintain normal virulence (Alexander et al., 2002), a finding that emphasizes the difficulty in dealing with INH-resistant infections. In contrast to those reports in which the mutant did not behave differently from wild type enzyme, it has been demonstrated that KatG can efficiently catalyze INH-NAD adduct formation in the presence of very dilute hydrogen peroxide while the S315T mutant enzyme shows poor function under similar conditions (Zhao et al., 2006). These observations raise interesting questions about the structural and functional origins of resistance in the mutants. Studies show that purified KatG[S315T] point to a 200-fold reduction in affinity for INH in the resting enzyme and poor turnover of the drug with compound I in the mutant (Kapetanaki et al., 2003).

Despite the importance of *M. tuberculosis* KatG in the physiology of mycobacteria, and its importance in INH action, the detailed mechanisms by which *Mycobacterium tuberculosis* KatG catalyzes hydrogen peroxide and activates INH have not been precisely elucidated. The identity of the active forms of INH that is responsible for bacterial killing is not fully known. The substrate-binding site located in *Mycobacterium tuberculosis* KatG has not been identified. It is not known how the electrons transfer between the enzyme and the substrate. In order to better understand the structure and function of KatG, and to begin to define the structural origins of INH resistance due to mutations in the *katG* gene, the x-ray crystallographic structures of the wild-type and S315T mutant of KatG from *M. tuberculosis* were pursued, along with substrate soaked or co-crystallized with the wild-type enzyme.

## **Materials and Methods**

### ***Crystallization***

The *M. tuberculosis* KatG and the KatG[S315T] mutant used in these studies were prepared from overexpression in *E. coli* strain UM262 (*katG* minus) supplied by our collaborator Dr. Magliozzo at the Department of Chemistry, Brooklyn College and The Graduate Center of the City University of New York, Brooklyn, New York. The bacteria were grown in presence of  $\delta$ -aminolevulinic acid, the heme biosynthetic precursor. The purified enzyme was dialyzed with 25mM Tris-HCl, pH7.5, 100mM

NaCl and concentrated to 16-24 mg/ml. All protein samples used for crystallization trials were less than one week old.

General reagents were obtained from Sigma. Polyethylene glycol (PEG) 4000 was from Fluka. Crystal Screen I&II and MemFac and PEG/Ion crystal screen kits were from Hampton Research. HYDRA 96 high-throughput robotic system was from Robbins Scientific.

The sitting-drop vapor diffusion method was performed by using a HYDRA 96 well high-throughput robotic system. Equal volumes of protein solution were mixed with reservoir solution containing ionic solvent with varied pH, precipitant, and additive. 1  $\mu$ l of protein sample and 1  $\mu$ l of crystallization buffer were injected into each well of the 96-well INTELLI-plate. The plates were incubated at 16 °C. Micro crystal clusters of *M. tuberculosis* KatG were initially obtained in 100mM sodium acetate pH4.6, 12% PEG4000 at protein concentration of 11 mg/ml one week after the initial crystal screen. Optimization grids of varied concentrations of precipitant (PEG 4000, 5-24%), sodium acetate (50-200mM at pH4.6), and protein concentration (11-24mg/ml) were screened to improve the size and quality of the crystals by the sitting-drop vapor diffusion method using 24-well plates. Each well of the 24-well plate contains a mixture of 4 $\mu$ l protein solution and 4 $\mu$ L crystallization buffer in a small well and 500 $\mu$ L solution in the reservoir. Thin plate-like crystals were obtained from the well containing 6% PEG4000, 100mM NaAcetate, pH4.6 and 16mg/ml of protein. Additional detergent screens were performed by using detergent screen kits from Hampton Research. 1  $\mu$ l of each detergent screen solution from the kit was added into each well of the 24-well plate containing 10

ul mixture of the protein and crystallization buffer in each well. *Mtb*KatG crystals were improved to a bigger size and better diffraction in the presence of 6% PEG 4000, 100mM NaAcetate, pH 4.6, and 0.17mM n-Dodecyl- $\beta$ -D-maltoside (Figure 12). The crystals were flash frozen at 120K after quick transfer into paratone-N, a cryoprotectant. *Mtb*KatG mutant S315T crystals were grown under the same condition as for the native enzyme.

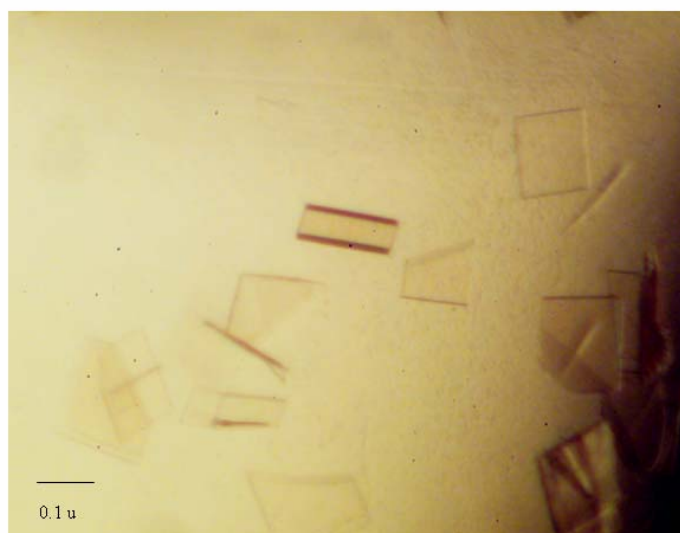


Figure 12. Single plate-like crystals of *Mtb*KatG.

The structure of wild-type *Mtb*KatG soaked in INH was investigated in order to elucidate the mechanism of INH activation. Both short soaked (5 min in 10mM INH) and long soaked (4 hours in 10mM INH) crystals were analyzed. INH-soaked with KatG

crystals were prepared by adding 1  $\mu$ L of 100mM INH to 10  $\mu$ l of a droplet containing crystals in mother liquor. The crystals were allowed to soak with INH for 5 minutes to 4 hours before quickly frozen in liquid nitrogen.

Since attempts to soak the substrate into the crystal failed to produce INH bond structure, co-crystallization trials were set up. However, the oxidation of INH by *Mtb*KatG is an ongoing process and its product, the isonicotinic radical is unstable. Cyanide binds to heme protein and often be used to probe the accessibility to the heme active site (Jakopitsch et al., 2005). It could be used to compete with INH for its binding site and slow down the INH oxidization. 1mM KCN was added to the co-crystallization solution. Both KCN and INH plus KCN co-crystals were investigated. 10 mM INH was added to 24 mg/ml (0.3mM) of KatG with or without KCN present. The mixture was incubated for 30 minutes on ice and then crystallized in the same condition as that of the wild-type enzyme.

### ***Data Collection and Structure Determination***

X-ray diffraction studies were conducted using an R-axis IV ImagePlate at the Center for Structural Biology, Albert B. Alkek Institute of Biosciences and Technology (IBT), Houston, Texas and a MacScience DIP2030b image plate detector coupled with a Rigaku X-ray generator at the department of Biochemistry & Biophysics at Texas A&M University. For high-resolution data collection, the Advanced Photo Synchrotron (APS) and the Advanced Light source (ALS) were utilized.

Integration and scaling of the X-ray data was performed using the HKL2000 containing XdisplayF/DENZO/Scalepack software packages (Otwinowski and Minor 1997). The crystal structure of *Mtb* KatG was solved by molecular replacement using the program MOLREP (Vagin 1997) in the CCP4 package (Collaborative Computational Project 1994). *Burkholderia pseudomalli* KatG (BpKatG) (1MWV) (Carpena et al., 2003) was used as the search model.

### ***Model Building and Refinement***

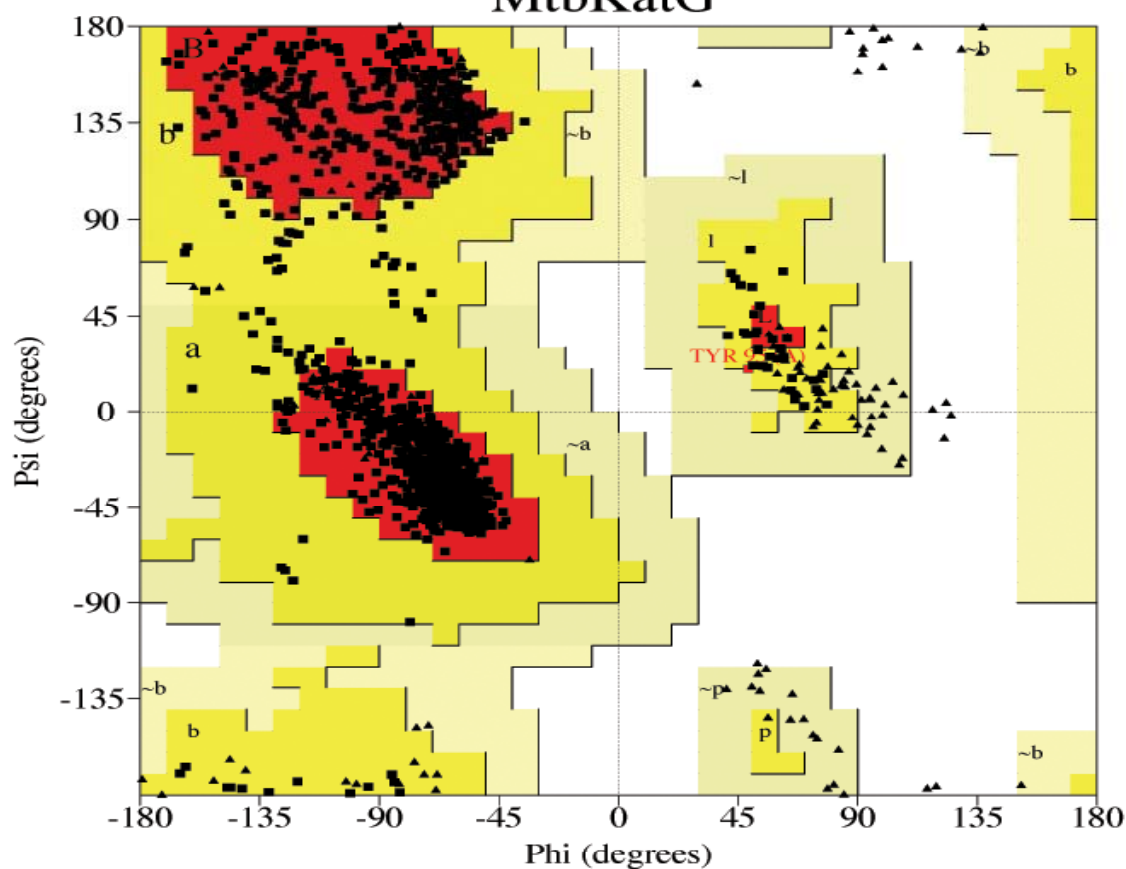
The resulting model from MOLREP was initially refined to 2.7 Å resolution with strict non-crystallographic restraints using the REFMAC5 program in the CCP4 suit (Collaborative Computational Project 1994), followed by model building using TEXTAL (Ioerger et al., 2003). The model was refined using the Simulated Annealing in CNS (Brunger et al., 1998) with further building and refinement in Xtalview (McRee 1999).

The phases of wild-type *Mtb*KatG were improved and extended to a resolution of 2.0 Å with the program SHAKE&WARP (Reddy et al., 2003). The resulting map shows clear continuity over the complete length of *Mtb* KatG from Met26 to Arg740 with the exception of a break in density in one subunit (chain B) in the region of Ala506 to Ala507. All refined residues from both chains fall into the energetically favorable regions of the Ramachandran plot by using program PROCHECK (Laskowski et al., 1993) (Figure 13).



PROCHECK

## Ramachandran Plot MtbKatG



### Plot statistics

Residues in most favoured regions [A,B,L]	1066	90.2%
Residues in additional allowed regions [a,b,l,p]	115	9.7%
Residues in generously allowed regions [~a,~b,~l,~p]	1	0.1%
Residues in disallowed regions	0	0.0%
-----		
Number of non-glycine and non-proline residues	1182	100.0%
Number of end-residues (excl. Gly and Pro)	1072	
Number of glycine residues (shown as triangles)	152	
Number of proline residues	92	
Total number		

Based

and R-factor no greater than 20%, a good quality model would be expected to have over 90% in the most favoured regions.

Figure 13. Ramachandran plot of *MtbKatG*. The figure was generated using program PROCHECK.

## Results and Discussion

### *Overall Structure of MtbKatG*

The crystals of wild-type KatG belong to space group  $p4_22_12$  with cell dimensions  $a=b=150$  Å,  $c=154$  Å,  $\alpha=\beta=\gamma=90^\circ$  (Table 2). The structure was refined to a crystallographic R and  $R_{\text{free}}$  factors of 18.5% and 22.8%, respectively, with good geometry at a resolution of 2.0 Å (Figure 13).

The *MtbKatG* enzyme exists as a dimer in the asymmetric unit, containing 1418 amino acids, two heme b prosthetic groups (iron protoporphyrin IX) and 938 ordered water molecules. The asymmetric unit contains two protein molecules denoted as subunits A and B (Figure 14). The two subunits of the dimer are related by a non-crystallographic 2-fold symmetry. The dimer is roughly ellipsoidal with approximate dimensions of 100 Å x 70 Å x 50 Å. The dimer interface buries a total of 4380 Å<sup>2</sup> accessible surface area per subunit, corresponding to approximately 15% of the total surface of a single subunit, indicating the extensive contact between the two subunits. Three *cis* proline residues (proline 131, 219, and 501) were found in both subunits. The residue arginine 418 was found to have alternate side-chain conformations in one subunit. The structure of each subunit contains 22 alpha helices folded into two separate domains, an N-terminal domain (residues Met 26 to Val 423) and a C-terminal domain (from Ala 424 to Arg740). Using the same naming scheme of *HmKatG* (Yamada et al., 2002) and the yeast cytochrome c peroxidase (CCP) (Finzel et al., 1984), ten helices

Table 2. Data collection and structure refinement statistics for wild-type *Mtb*KatG

A. Data collection statistics	
Wavelength	0.9
Unit cell parameters	
a	150.1
b	150.1
c	153.7
Space group	P42212
Resolution limits	2.0
Unique reflections	105049
Completeness	99.0 (96.7) <sup>a</sup>
Rsym <sup>b</sup> (%)	8.3 (35.1)
I/sigma	26.2 (4.5)
B. Refinement statistics	
Resolution range	20.0-2.0
Working set reflections	
Test set size	5%
R cryst <sup>c</sup> (%)	19.8
R free <sup>d</sup> (%)	22.9
Protein-non-H atoms	12063
Number of water molecule	938
Rmsd of bond distances (A)	0.01
Rmsd of bond angles (deg)	1.05
Average B value	23.93

<sup>a</sup> Numbers in parentheses represent values in the highest resolution shell.

<sup>b</sup>  $R_{\text{sym}} = \frac{\sum_h \sum_i |I(h,i) - \langle I(h) \rangle|}{\sum_h \sum_i I(h,i)}$  where  $I(h,i)$  is the intensity value of  $I(h)$  for all  $i$  measurements.

<sup>c</sup>  $R_{\text{cryst}} = \frac{\sum ||F_o - F_c||}{\sum |F_o|}$ , where  $|F_o|$  and  $|F_c|$  are the observed and calculated structure factor amplitudes respectively.

<sup>d</sup>  $R_{\text{free}}$  is the same as  $R_{\text{cryst}}$  but calculated with 5% subset of all reflections that was never used in any refinement.

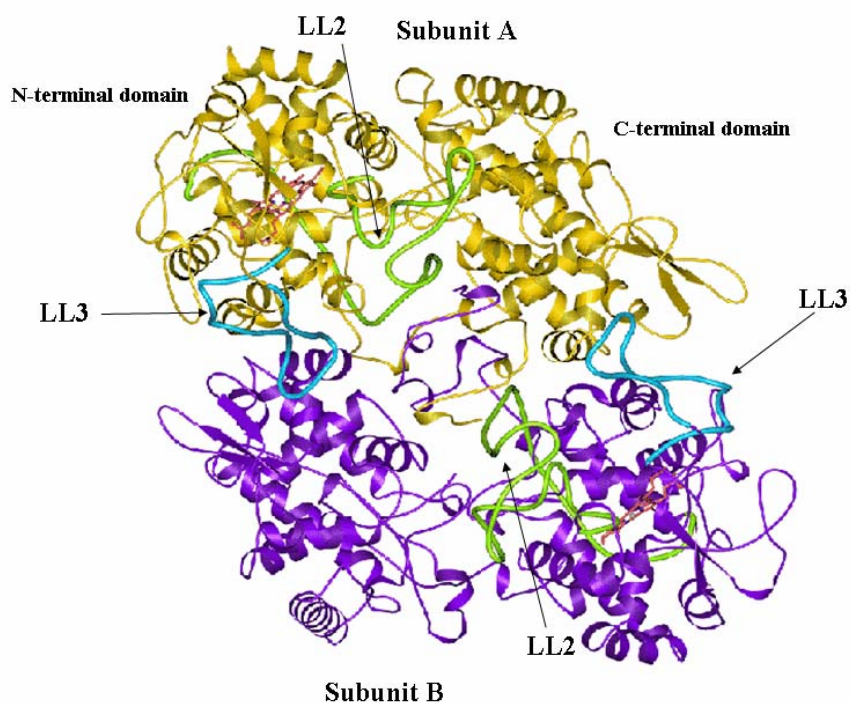


Figure 14. Overall structure of *MtbKatG*: Two monomers are labeled gold and purple. Loop LL2 is green and loop LL3 is blue. Heme b is colored red. The figure is constructed using MolScript (Kraulis 1991).

from each domain were assigned (Figure 15). Two extra helices (5-7 residues long) were also found in the N-terminal domain of each subunit and designated as helices A1 and C1. A functional heme group is buried inside a pocket located in between the helices B and the helices F in the N-terminal domain of each subunit. The side of the heme that faces the molecular surface is called proximal side and the side that faces the

heme from the second subunit is named the distal side. The heme pocket has a dimension of  $8 \times 6 \times 4 \text{ \AA}^3$  and its distal side connects to the molecular surface through a long substrate access channel (see below).

In addition to harboring a functional heme group, the N-terminal domain also plays a role in protein dimerization (Wilming 2001). It has been demonstrated by the yeast two-hybrid system that the first 99 amino acids of the N-terminal domain are responsible for the dimerization of the *Mtb* KatG. From the crystal structure of *Mtb*KatG, it has been clearly shown that two N-terminal arms of the dimer are oriented anti-parallel to each other with close contacts between residue Asn41 from subunit A and residue Lys 27 from subunit B and vice versa. The N-terminal arm of subunit A (residue Met26 to Asn41) runs into the C-terminal domain of subunit B and likewise, the N-terminal arm of subunit B turns into the C-terminal domain of subunit A, forming a domain-domain swapped structure (Figure 14). Aside from the contribution to dimer formation, no functional role has been assigned to this domain yet.

The catalase-peroxidases differ from the other Class I peroxidase enzymes in that they have three loop insertions defined as LL1, LL2, and LL3 in the structure of *Hm*CP (Yamada et al., 2002). Similar loops were found in *Mtb*KatG as well (Figure.14). Loop LL2 from Pro 194 to Asn 231 is located on the molecular surface with its near C-terminal end close to the distal heme pocket. Tyr 229 is located near the end of this KatG specific loop, providing the central side chain in the unique three amino acid adduct Trp-Tyr-Met found on the distal side of the active site of KatGs (see below). Mutation of residue Tyr 229 to Phe results in loss of catalase function (but enhanced

peroxidase activity) in the KatG enzyme (Jakopitsch et al. 2003a), suggesting that the loop is a key structural element that transforms a mono-functional peroxidase into a dual function enzyme. Loop LL2 also contains residues that are involved in formation of the substrate entrance channel leading to the distal heme pocket including Asp 194, Gln 233, Leu 205, Asn 231 and Gly 226 at the molecular surface. Arg 119 is located at the surface of the entrance opposite to Asp 194 and thus gives a low positive charge to the other side of the channel. The second large loop (LL3) from Pro 280 to Ile 313 is unique to KatGs as well. Thr 314 and Ser 315, which are adjacent to the loop, are located at the narrowest point of the substrate entrance channel (see below). Therefore, these loop insertions in the catalase-peroxidases provide structural features absent from CCP (Finzel BC 1984) in the Class I peroxidase family and have a major impact on the function of the KatGs.

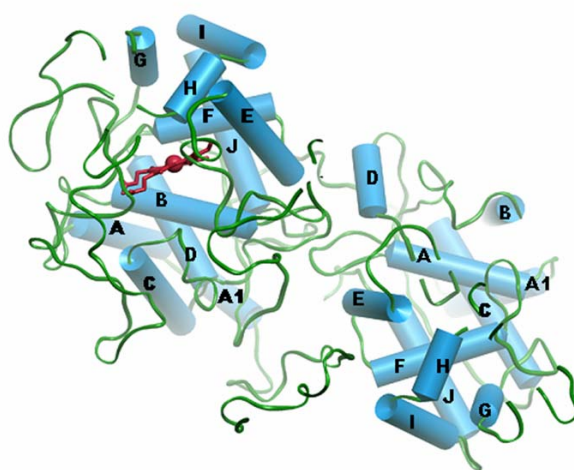


Figure 15. Ribbon diagram of one subunit in the *MtbKatG* dimer: 11  $\alpha$ -helices in each domain are labeled according to the naming scheme for CCP and *HmCP*. The heme b is colored red. The figure is generated using SPOCK (Christopher 1997).

### ***Heme Cofactor***

Each subunit of the KatG dimer contains a single molecule of the iron protoporphyrin IX cofactor buried in a deep pocket of the N-terminal domain. The protoporphyrin ring is moderately distorted into a saddle shape with pyrrole rings II and IV tilted to ward the proximal side and pyrrole rings I and III tilted toward the distal side of the heme (Figure 16). There is a small displacement of the iron towards the proximal His, about 0.2 Å out of the mean pyrrole nitrogen plane.

The heme iron is six coordinated. The fifth and sixth coordination positions are occupied by the side chain of His 270 from proximal side (2.2 Å) and a water molecule W261 of the distal side (2.9 Å) (Figure 16). The structure solved for KatG is consistent with the 6-coordinate iron in both subunits, despite the long water-iron bond length (2.9 Å), when compared with 2.5 - 2.7 Å in other peroxidases such as in LiP (2.7 Å) and *BpKatG* (2.5Å). The water molecule (W261) at the distal heme site may be considered poised in a position such that both 5 and 6-coordinate forms are accessible to the enzyme in the solution. It has been demonstrated that the heme iron in *MtbKatG* can be interchanged between the 5th and 6th-coordinate as a function of the conditions used for purification, storage, the pH, and the presence of INH (Kapetanaki et al., 2003).

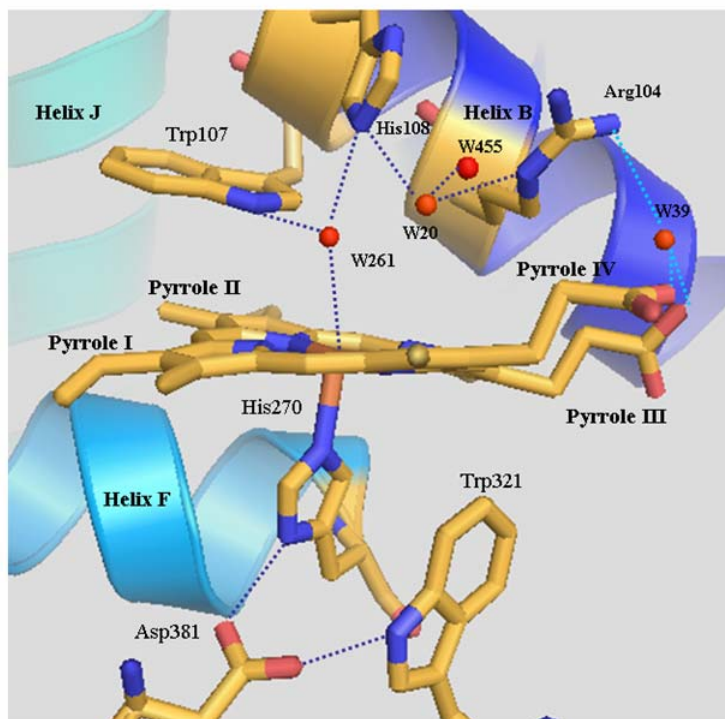


Figure 16. The heme active site of *MtbKatG*. Both distal and proximal active site residues are shown. The ordered water molecules at the distal heme site were colored red. Interactions are indicated by dashed lines. The figure was made using program PyMol (Delano 2002).

### ***Proximal Heme Binding Site***

The proximal side of the heme-binding pocket is lined by mostly hydrophobic residues from both helices F and J (Leu265, Phe252, Ile248, Ile266, His270, Thr275, Trp321, Asp381, Phe408, and Trp412).  $\alpha$ -helix F runs nearly parallel to the heme plane with its



closest contact to the heme plane at a distance of 2.2 Å in between the side chain of His270 and the heme iron (Figure 16). The proximal side of the heme binding site contains the catalytically important amino acid triad His270-Asp381-Trp 321 (Figure 16), typical of peroxidases in the Class I peroxidase family. The imidazole side-chain of His270 is perpendicular to the heme plane, with the nitrogen of the side chain forming an electrostatic interaction with the heme iron (2.2 Å). The indole ring of Trp 321 is parallel to the imidazole ring of His 270 at distance of about 3.5 Å. The oxygen atoms of the carboxyl group of the Asp 381 side chain are hydrogen bonded to N<sup>δ</sup> of His 270 (at distance of 2.8Å) and the indole nitrogen of Trp 321 (at distance of 2.6Å) so that protons can be shared within the triad of His-Asp-Trp. The presence of the hydrogen bonding at the proximal histidyl imidazole N<sup>δ</sup> is a conserved feature in the peroxidase family that contributes to the functional properties of the heme peroxidase enzyme (Finzel 1984).

### ***Distal Heme Binding Site***

On the distal side of the heme, the catalytically important residues Trp 107, His 108 and Arg104 are conserved in the class I peroxidase family as well. Figure 16 shows the disposition of these residues in the distal active site.

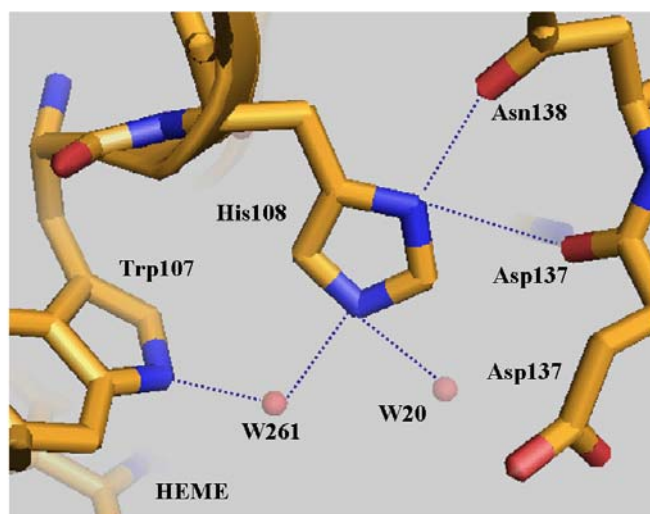
The indole ring of Trp107 lies parallel to the heme plane at distance of 3.5 Å lying over pyrrole ring II on the distal side of the heme (Figure 16). The imidazole ring of His108 is located perpendicular to the heme plane and about 5.6 Å to the heme iron, a distance consistent with the lack of evidence for a low spin heme iron in *MtbKatG*.

(Chouchane et al., 2000). The center structural water molecule, W261, is in between the heme iron (2.9 Å) and His108 (2.7 Å) on the distal side of the heme (Figure 16).

The imidazole ring of His108 is stabilized by two possible hydrogen bonds formed between N<sup>δ1</sup> of His108 and O<sup>δ1</sup> of Asn138 (2.7 Å) and the main chain oxygen atom of Asp137 (2.9 Å) (Figure 17a). The conserved distal histidine, which facilitates the deprotonation of H<sub>2</sub>O<sub>2</sub> and assists in the heterolytic cleavage of the O-O bond, is thought to be the essential feature of the heme peroxidase (Poulos et al., 1980). Mutation of the distal histidine or arginine interferes with formation of Compound I, while mutation of the tryptophan residue results in lost of catalase activity, with retention or even enhancement of peroxidase activity (Hillar 2000) (Regelsberger et al., 2000). The *Mtb*KatG structure presented here does not indicate a major deviation in the mechanism for Compound I formation between CCP and KatGs when considering the conserved residues on both the distal and proximal sides.

The extensive hydrogen-bond network formed around the side chain of the Arg104 may also play an important role with respect to the heme binding and reactivity towards hydrogen peroxide. The backbone carbonyl oxygen of Ala139 is within hydrogen bonding distance to both N<sup>η1</sup> (2.9 Å) and N<sup>η2</sup> (3.0 Å) of the Arg104 (Figure 17b). The disruption of these hydrogen bonds may account for the decreased INH activation (80%) in Ala139Pro mutant (DeVito and Morris 2003). The N<sup>η2</sup> of the Arg104 can also hydrogen bond to the main chain oxygen atom of Asp137 at 2.9 Å. Asp137 is located at the narrow neck of the substrate entry channel (see below). The N<sup>η1</sup> of the Arg104 is hydrogen bond to a solvent molecule (W39) (3.0 Å). This solvent molecule is located

(a). Hydrogen-bond network around distal His108



(b). Hydrogen-bond network around distal Arg104

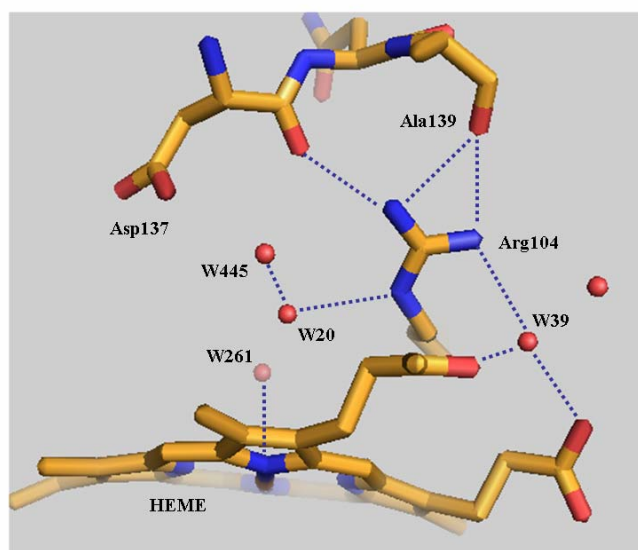


Figure 17. Hydrogen-bond networks at the distal site of *MtbKatG*. The figure is constructed using PyMol. The hydrogen bonding interactions are indicated by the blue dashed lines. The ordered water molecules were shown in red balls.

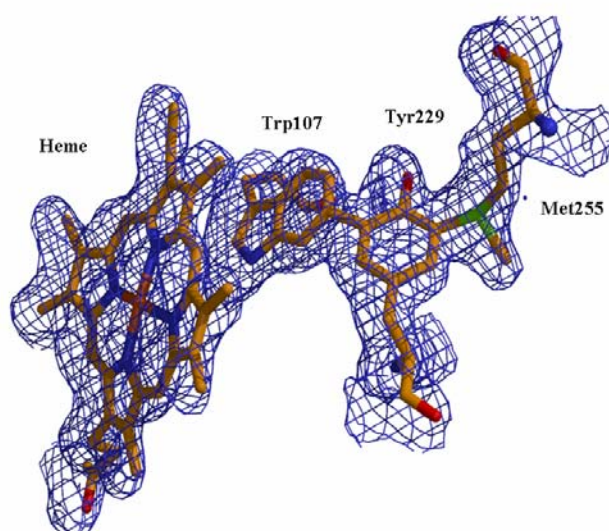
between the two propionate groups and forms hydrogen bonds with O<sup>1δ</sup> of the propionate of pyrrole ring III (2.7 Å) and O<sup>2α</sup> of the propionate at the pyrrole ring IV (2.7Å) (Figure 16).

A water molecule (W20) is hydrogen-bond to the N<sup>ε2</sup> of the imidazole of His 108, the N<sup>ε</sup> of Arg104 side chain and the third water molecule (2.5 Å) in the distal heme pocket, but is farther away from the center water molecule W261 (3.3 Å) (Figure 16). The coordination of the water molecules (W20 and W445) may represent a hydrogen peroxide binding site in the wild-type KatG. Both Arg104 and His108 are required for the peroxidase activity of *Mtb*KatG. Mutation of Arg104 or His108 results in a loss of peroxidase activity (Saint-Joanis et al., 1999).

### ***The Active Site Adduct***

The unique three amino acid adduct Trp-Tyr-Met is found in the *Mtb*KatG structure (Figure 18a). The adduct formed among side chains of the Trp107, Tyr229 and Met255 is located in the vicinity of the distal heme binding site (Figure 18b). The Tyr229 from the end of the KatG specific loop LL1 is the central residue of the adduct suggesting its role in this dual function enzyme. The bond length between C<sup>ε1</sup> of Tyr 229 and C<sup>η2</sup> of Trp 107 is 1.69 Å, which is the same as in *Hm*CP (1.68 Å) and *Bp*KatG (1.69Å). The bond distance between S<sup>δ</sup> of Met 255 and C<sup>ε2</sup> of Tyr 229 is 1.78Å, similar to the reported values of *Hm*CP (1.72Å) and *Bp* KatG (1.78Å). While the indole and phenol rings

(a) The electron density map of the adduct



(b) The Trp-Tyr-Met adduct at the active site.

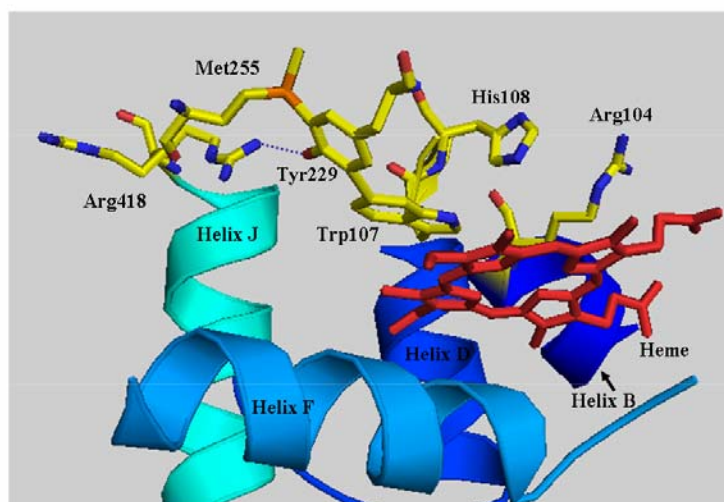


Figure 18 The Trp-Tyr-Met adduct. (a). The unbiased electron density map was calculated using SHAK&WARP, the bias removal server (Reddy et al., 2003). The map of the adduct was contoured at one sigma and the figure was constructed using Xtalview; (b). The Trp-Tyr-Met adduct and the distal active site residues were shown. The heme is colored red. The double conformations of the Arg418 side chains were also indicated in the figure. The figure was made in PyMol (DeLano 2002).

themselves are planar, the adduct is puckered with its shallow bottom close to pyrrole ring II of the distal heme. This adduct is located in a very hydrophobic environment with no possible access to solvent molecules except W261, the central water molecule to the indole nitrogen of the Trp107 in the distal heme pocket. This unusual distal side adduct was first identified in the crystal structure of *HmCP* (Yamada et al., 2002) and was more recently confirmed in the structure of *BpKatG* (Carpena et al., 2003). The existence of the adduct in *Synechocystis* KatG was also found in solution by mass spectrometry of tryptic digests (Jakopitsch et al., 2003a), demonstrating that the adduct is not an artifact and is a common feature of the catalase-peroxidases. Indeed, studies confirmed that the adduct is required for catalase but not the peroxidase activity (Jakopitsch et al., 2003b).

The double conformation of the side chain of Arg418 is located near the Trp-Tyr-Met adduct in between helices B and J in the N-terminal domain of each subunit (Figure 18b). In one conformation (50%), A guanidino group of Arg418 points toward Tyr229 and forms a hydrogen bond with O<sup>η</sup> of Tyr229 (3.1 Å), which is longer when compared to that of the *BpKatG* (2.9 Å) and *HmCP* (2.8 Å). The N<sup>η2</sup> of Arg418 also forms a hydrogen bond to the amide nitrogen atom of Met255 at a distance of 2.6 Å (Figure 18b). The interactions that stabilize the covalent bonds in the adduct are conserved features in KatGs when compared with two other published KatG structures. When Arg418 is in the alternative orientation, in its side chain points toward a large solvent channel (see below) and one water molecule replaces the Arg side chain and is hydrogen bonded to the hydroxyl of the Try229.

### ***Substrate Access Channels to the Active Site***

The molecular surface of *Mtb* KatG reveals at least two heme access channels in each subunit of the dimer. The first channel is a substrate entrance channel, analogous to the channel previously identified in *HmPC* (Yamada et al., 2002) and *Bp* KatG (Carpena et al., 2003). This major channel provides access to the distal side of the deeply buried heme cofactor (about 20 Å from the molecular surface) (Figure 19). This channel differs from that of the monofunctional catalases (beef liver catalase and HP11 from *E. coli*) or peroxidases (CCP and ARP). In catalases, the heme is buried more deep with longer substrate access routes (30-55 Å) (Reid et al., 1981). In contrast, the access channel in peroxidases is shorter (~10 Å) and is also less constricted (Finzel et al., 1984). The major access channel in *Mtb*KatG closes down from around 14 Å across at the surface of the molecule, to about 6 Å at its narrowest point near Ser315 where there is a bend into the distal side pocket. This channel is lined with mostly hydrophobic residues and a number of polar residues. The residues around the channel near the heme pocket are Thr 314, Ser 315, Asp 137, Leu 227, and Pro 232. The narrowest part of the channel is delimited by Ser 315 and the carboxyl group of Asp 137, which is about 10 Å from the heme iron. This narrow neck in the channel creates a steric barrier for access to the heme active site.

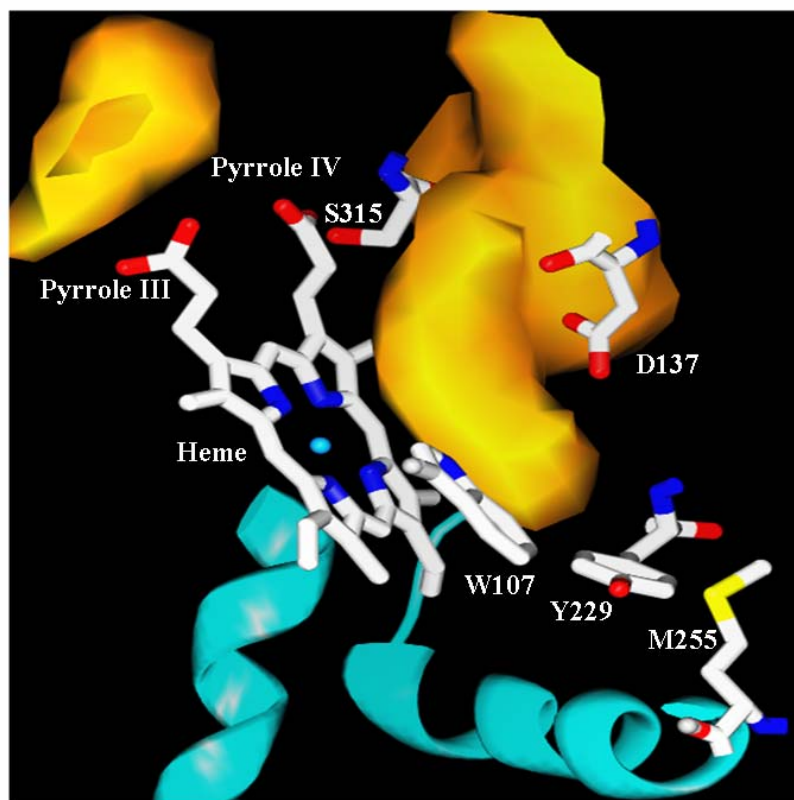


Figure 19. The access channels to the distal active site. Both major and minor substrate channels are colored gold. The picture was constructed using SPOCK with key active site residues and the heme being highlighted.

The second smaller channel found in each subunit of the dimer in *Mtb* KatG was not identified in the earlier KatG enzyme structures. The smaller portal lies approximately in the plane of the heme and comes close to the propionate group at pyrrole ring III (Figure 19). This portal is about 10 Å long and is formed by residues Gly99, Pro100, and Leu101 from one side and Asp94 and Phe368 from the other side. The portion of the



channel that leads to the molecular surface appears to be interrupted by the side chain of the distal Asp94 and Phe368, indicating that very small movements in the side chain may be able to open up or close down the small channel.

Both channels contain a large number of ordered water molecules. The existence of the two channels and the continuum of the water molecules in the channels suggest a model in which separate routes may be available for hydrogen peroxide (substrate) access and water and oxygen (products) release during the product turnover. It is reasonable to propose that the small portal facilitates release of the water or oxygen that was generated from hydrogen peroxide reduction without competition from incoming peroxide molecules.

A large U-shaped channel similar to the one in *Bp*KatG is found to exist in *Mtb*KatG as well (Figure 20a). The interesting feature of the channel is that it connects to the molecular surface through two funnels; one side may serve as entry and the other as exit. Arg418 is located at the bottom of this U-shaped channel (Figure 20). The Trp-Tyr-Met adduct is located right beside Arg418. The guanidino group of Arg418 has alternate conformations. In one conformation (50%), the side chain of Arg418 is directed toward the central residue Tyr229 of the adduct. In the conformation in which the side chain of the Arg418 is pointed toward the molecular surface, the channel is blocked or interrupted (Figure 20b). This channel may provide a direct access to the adduct through the side chain of Arg418. It has been suggested that this very well defined cavity might serve as a second substrate binding site in KatGs (Mo et al., 2004). It is possible that the tyrosine hydroxyl is deprotonated and forms a salt-bridge to the positively charged

Arg418 side chain, but it becomes neutral when the Arg side chain takes another conformation. The sulfate of Met255 in the adduct most likely carries a positive charge and would provide a driving force to draw electrons from the cationic groups. It has been proposed that the first hydrogen peroxide reacts with the KatG at the initial substrate-binding site (close to His108 and Arg104) to form compound I (Mo et al., 2004). The second hydrogen peroxide, which is located at the bottom of the U-shaped channel and hydrogen bonds to Try229 when the Arg418 side chain is in the orientation towards the channel, could serve as a reducing agent to oxidize compound I back to the resting enzyme through its interaction with the cationic cluster (Mo et al., 2004).

(a) U-channel

(b) U-channel interruption by Arg418 side chain

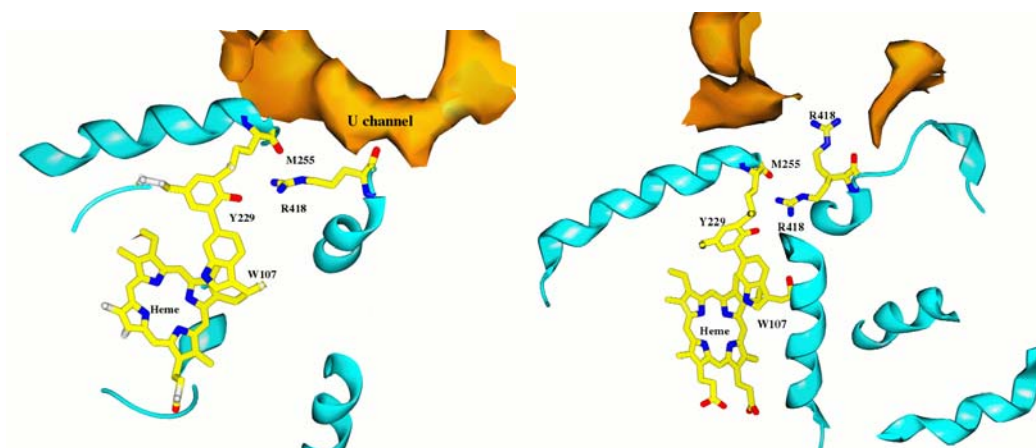


Figure 20. The U-shaped channel and the features of the alternate conformations of Arg418 side chain.

### ***Overall Structure of *MtbKatG*[S315T] Mutant***

The overall structure of *MtbKatG*[S315T] mutant is the same as the wild-type enzyme. The rms deviation for 715 C $\alpha$  atoms from each subunit, after superimposition of the two structures, is 0.29 Å. The first 25 residues from both subunits remain disordered and are not included in the refined structure. Crystallographic R and R<sub>free</sub> factors and other refinement statistics are similar to that in the wild-type *Mtb KatG* (Table 3). The quality of the model was verified by PROCHECK (Figure 21).

The electron density of the methyl group of the threonine 315 side chain is clearly seen even with Ser315 as the search model (Figure 22). The arrangement of catalytically important residues on both proximal and distal sides at the heme in KatG [S315T] is essentially the same as in the wild type enzyme. The distal side adduct of Trp-Tyr-Met side chains was found in both subunits in the mutant structure. This observation along with the very close alignment of all other heme pocket residues in the mutant compared to the wtKatG is consistent with the relatively unaltered catalase and peroxidase activities of the purified mutant enzyme.

### ***The Heme Cofactor in *MtbKatG*[S315T]***

The heme iron is five coordinated in *MtbKatG*[S315T] compared to a six coordinated heme from the wild-type enzyme. The ordered water molecule W261 occupying the sixth coordination position in the wild-type KatG disappeared from the mutant structure, leaving the heme iron five coordinated. Five data sets were collected

Table 3. Data collection and structure refinement statistics for *MtbKatG* [S315T]

A. Data collection statistics	
Wavelength	0.98
Unit cell parameters	
a	149.8
b	149.8
c	154.5
Space group	P42212
Resolution limits	2.1
Unique reflections	76312
Completeness	78.5 (64.0) <sup>a</sup>
Rsym <sup>b</sup> (%)	11.8 (23.8)
I/sigma	9.4 (2.1)
B. Refinement statistics	
Resolution range	20.0-2.1
Test set size	5%
R cryst <sup>c</sup> (%)	23.0
R free <sup>d</sup> (%)	27.6
Protein-non-H atoms	11749
Number of water molecule	596
Rmsd of bond distances (Å)	0.01
Rmsd of bond angles (deg)	1.39
Average B value	20.28

<sup>a</sup> Numbers in parentheses represent values in the highest resolution shell.

<sup>b</sup>  $R_{\text{sym}} = \frac{\sum_h \sum_i |I(h,i) - \langle I(h) \rangle|}{\sum_h \sum_i I(h,i)}$  where  $I(h,i)$  is the intensity value of  $I(h)$  for all  $i$  measurements.

<sup>c</sup>  $R_{\text{cryst}} = \frac{\sum ||F_o - F_c||}{\sum |F_o|}$ , where  $|F_o|$  and  $|F_c|$  are the observed and calculated structure factor amplitudes respectively.

<sup>d</sup>  $R_{\text{free}}$  is the same as  $R_{\text{cryst}}$  but calculated with 5% subset of all reflections that was never used in any refinement.

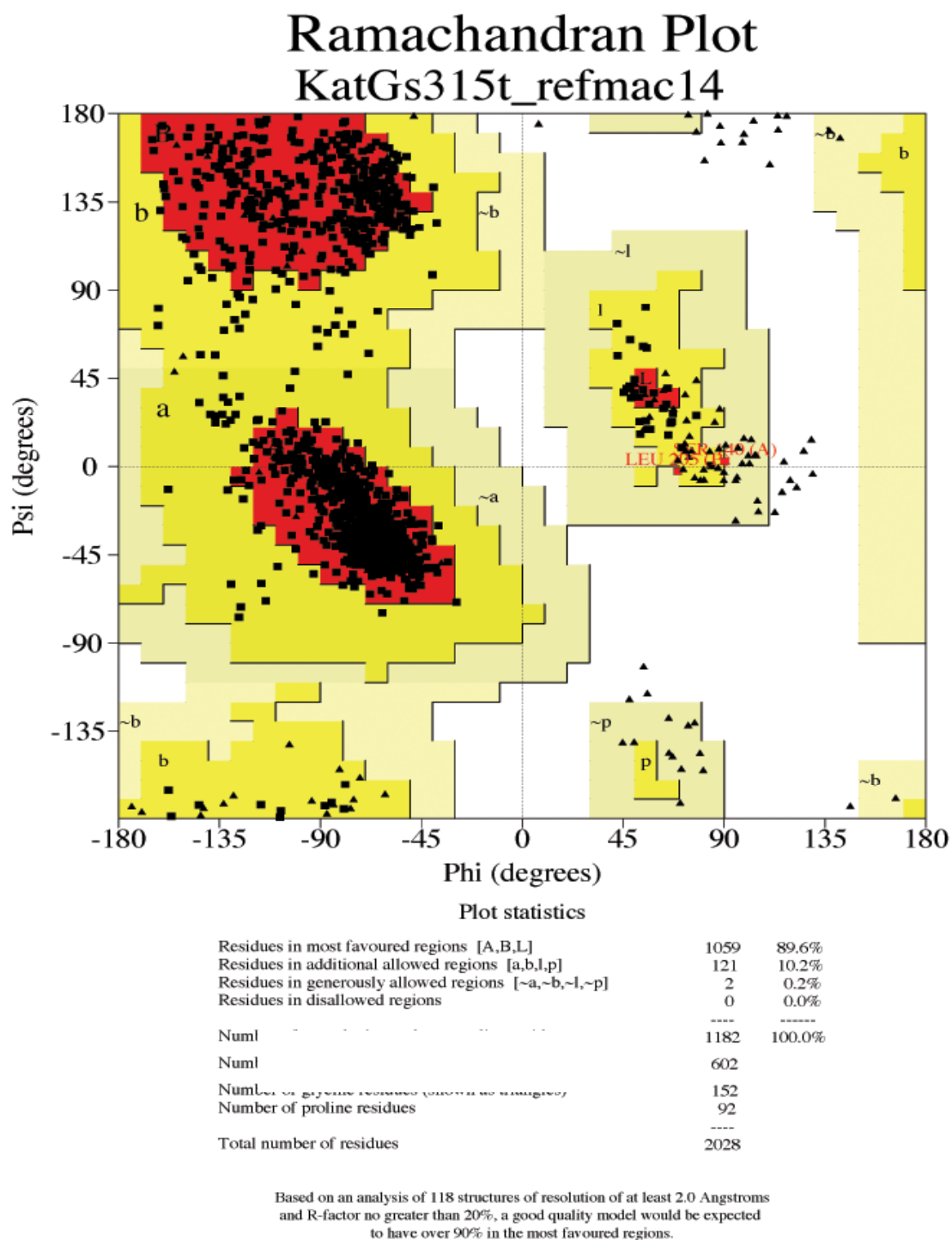


Figure 21. Ramachandran plot of the *Mtb*KatG [S315T] generated in PROCHECK.

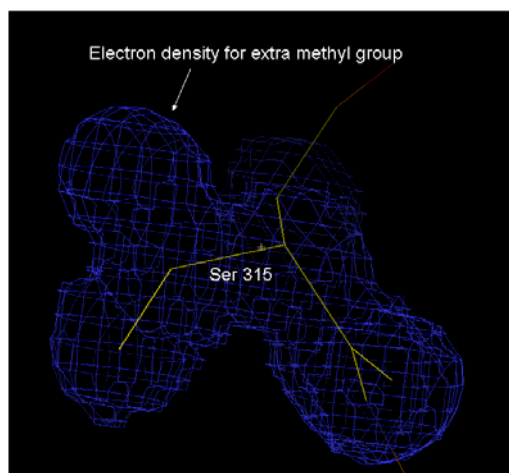


Figure 22. Electron density map showing the methyl group of the threonine 315 side chain in KatG[S315T]. The 2Fo-Fc electron density map was obtained by using wtKatG (Ser315) as the refinement model.

and processed to good qualities for both *Mtb*KatG and *Mtb*KatG[S315T] (Table 4). The missing water coordination consistently shows in all of the *Mtb*KatG[S315T] structures refined to date. There is clear electron density at the distal heme assigned as W261 and the water molecule has a refined B factor of 29.1 Å<sup>2</sup> (mean B factor for all atoms in the structure is 23.9 Å<sup>2</sup> for wt KatG) (Figure 23a). In contrast, there is no corresponding electron density in the mutant structure (Figure 23b). This coordination shift could be significant because the oxidation state or the redox potential of the heme differs in different coordination and may affect enzyme reactivity (Proshlyakov et al., 2000). Although not the focus of our study, EPR and resonance Raman spectroscopy was used to

analyze the electronic absorption spectrum to get some basic insight into the coordination environment and spin-state of the heme (Chouchane et al., 2003). It has been demonstrated that the heme iron in the wild-type KatG contains abundant 6-c heme iron, while the S315T mutant remains predominantly 5-coordinate (Kapetanaki 2003). They proposed that the S315T mutation weakens the hydrogen bond between His276 and the heme 7-propionate group and might result in an increase in nonplanar heme deformation, which leads to formation of the 5-coordination heme state (Kapetanaki et al., 2003).

Table 4. Multiple data collections and refinements for *Mtb*KatG and *Mtb*KatG[S315T]

	Beam line	Wave- Length	Resolution Å°	Completeness %	R-factor %	R-free %	Rmsd Å°	Rmsd Angles	B-factor Å <sup>2</sup>
wtKatG	APS <sup>a</sup> 14ID	0.98	2.0	99	19.8	22.9	0.01	1.26	23.9
wtKatG	APS 14BM	1.0	2.4	99	21.2	24.5	0.01	1.34	25.9
wtKatG	DIP <sup>b</sup>	1.5	2.7	97	23.8	26.7	0.02	1.43	30.1
S315T	IBT <sup>c</sup>	1.5	2.6	98	22.6	27.4	0.01	1.31	31.0
S315T	ALS <sup>d</sup>	0.90	2.1	79	23.0	27.6	0.01	1.39	20.3

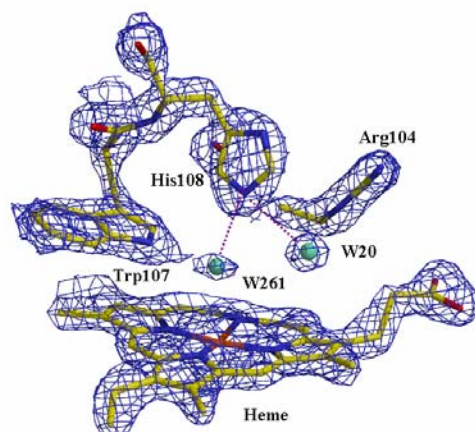
<sup>a</sup> Data collected from the Advanced Photo Synchrotron (APS) at Argonne National Laboratory, Chicago.

<sup>b</sup> Data collected using a MacScience DIP2030b image plate detector coupled with a Rigaku X-ray generator at Texas A&M University.

<sup>c</sup> Data collected using an R-axis IV ImagePlate at the Center for Structural Biology, Albert B. Alkek Institute of Biosciences and Technology (IBT).

<sup>d</sup> Data collected from the Advanced Light Source (ALS) at University of California, Berkeley.

(a) wtKatG



(b) KatG[S315T]

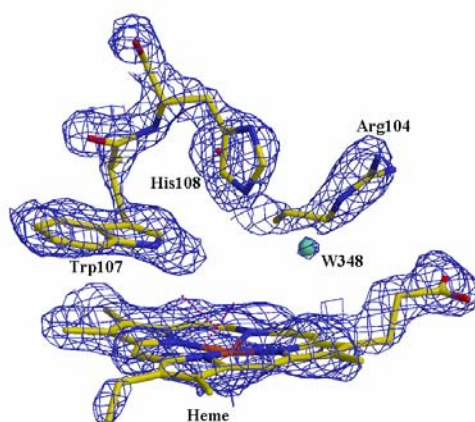


Figure 23. Distal heme environment comparison between *Mtb*KatG and KatG[S315T] mutant: (a) The 2Fo-Fc electron density map of wtKatG at 2 sigma contours with the model of the heme and distal side residues Arg104, Trp107 and His108 along with the water molecules superimposed. Hydrogen bonds are indicated by the broken lines. (b) The 2Fo-Fc electron density map of KatG[S315T] at 2 sigma with the model of the heme and distal side residues Arg104, Trp107 and His108 along with the water molecule superimposed.



### ***Substrate Access Channels in MtbKatG[S315T]***

The most important change in *MtbKatG*[S315T] is due to the presence of the methyl group of the side chain of threonine 315, which effectively limits the accessibility to the heme by constricting the dimensions of the narrowest part of the channel from 6 Å in the wtKatG to 4.7 Å in the mutant (Figure 24). It has been proposed that hydrogen peroxide passing through the access channel in the native KatG promotes the formation of a continuous flow of solvent and peroxide (Jones 2001). The steric constraints introduced by the KatG[S315T] mutant may hinder the continuous flow in the substrate access channel (Zhao et al., 2006).

The side chain of Arg418, which is located on the bottom of the U channel, has alternate conformations in wtKatG. However, this dual conformation seems to be not as well defined in the mutant structure. Refinement gives low occupancy (30%) for the conformation pointed towards Tyr229, the central residue of the Trp-Tyr-Met adduct and shows well defined electron density for the conformation with the side chain directed toward the molecular surface, consequently breaking the U-shaped channel. A similar channel was also found in *BpKatG* structure, suggesting a possible binding site for a substrate (Carpena et al., 2003). Unfortunately, the identity of the in vivo substrate remains unknown for both *BpKatG* and *MtbKatG*.

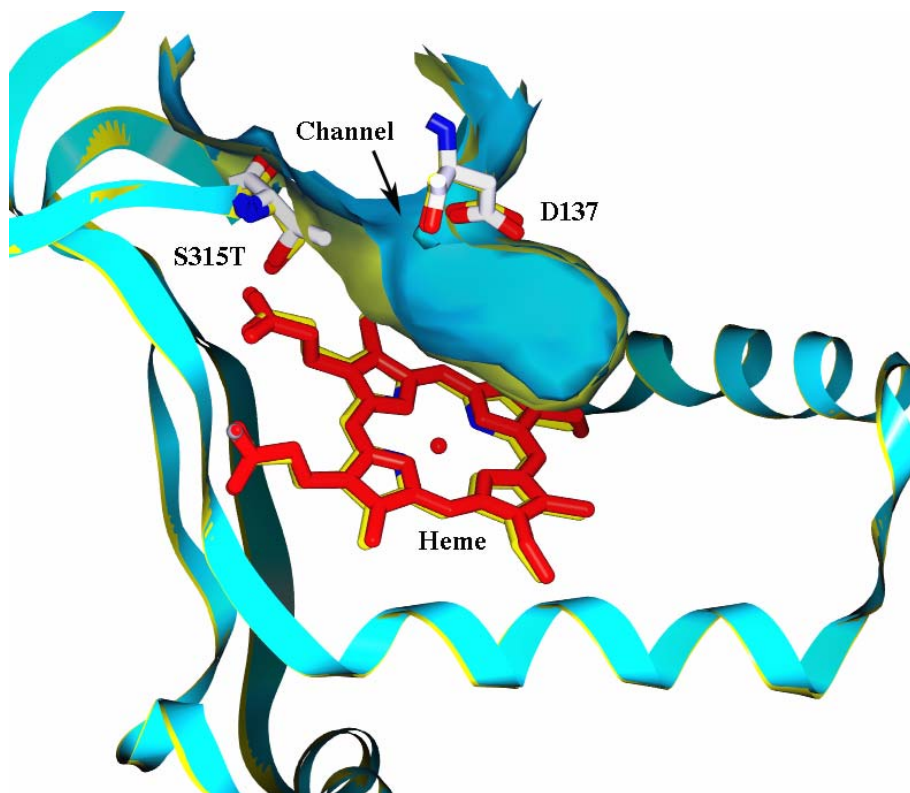


Figure 24. Structural comparisons of *MtbKatG* and KatG[S315T] mutant at the distal side of the substrate access channel. The figure was constructed using graphic program SPOCK with superimposed wt and mutant KatG PDB. Molecular surfaces were calculated and displayed in yellow for wt KatG and blue for the mutant S315T. The substrate access channel to the distal side of the heme was displayed within 12 Å distances to the heme by clicking through molecule surface in the SPOCK program. Asp137 and Thr315 residues of the mutant are colored by atom type. The heme is colored red in the mutant. The corresponding residues from *MtbKatG* are colored yellow. The ribbon diagram of the mutant was shown in blue and superimposed with that of *MtbKatG* in yellow.

It has been shown that mutation S315T produces only moderately reduced catalase (2-fold) and peroxidase specific activity (4-fold) *in vitro*. However, the MIC is increased about 200-fold for the S315T mutant strain compare to the wild-type enzyme (Heyme et al., 1993). In general, the catalase activity is measured spectrophotometrically by following the decrease in  $\text{H}_2\text{O}_2$  concentration at 240nm (Saint-Joanis et al., 1999) and the peroxidase activity can be determined spectrophotometrically by measuring the oxidation rate of *o*-dianisidine, a peroxidase substrate, to *o*-dianisidine quinonodimine at 460nm in presence of *t*-butyl hydroperoxide (Saint-Joanis et al., 1999; Zhao et al., 2006). Reduction can also be monitored qualitatively by means of the NBT (NitroBlue Tetrazolium) reduction assay (Hillar 1995). The radical formation in presence of INH can be detected by using NTB, which shows blue color when reduced by phenolic radicals (Wengenack et al., 2004). The isonicotinic acyl radical is unstable, the final product of the INH oxidation is proposed to be isonicotinic acid. Studies showed that the wild-type enzyme was more efficient than the S315T mutant at converting INH into isonicotinic acid (Wengenack et al., 1997; 2004). The structures of the wild-type KatG and S315T mutant solved here suggest that the replacement of threonine for serine produces steric effects that interfere with interaction between the enzyme and INH but do not interfere with formation of Compound I from small peroxide molecule such as  $\text{H}_2\text{O}_2$ . The drug binding within the heme pocket is a likely requirement for INH activation (Zhao et al., 2006).

### ***Structural Modeling of Clinically Significant Mutants***

INH resistance in *M. tuberculosis* clinical isolates has been associated with either the complete loss of the *katG* gene or deletions, insertions, and/or point mutations within the gene. The various clinically significant mutations in *MtbKatG* are listed in Table 5.

There are basically four types of mutations. The first category includes the KatG[S315T] which is located at the bottom of the narrow neck of the major substrate access channel (Figure 24). The KatG[S315T] mutant shows a minor change in catalase and peroxidase activity but a significant effect on INH activation (Saint-Joanis et al., 1999) due to the presence of the methyl group of the Thr 315 side chain, which effectively limits accessibility to the active site.

The second group of mutants includes the mutations that are located at the distal heme side, including R104L, H108Q, N138S and A139V (Figure 25a). This type of mutation shows significantly reduced catalase activity due to the interruption of the hydrogen bonding networks that are crucial for catalase activity (Ghiladi et al., 2005). Both arginine 104 and histidine 108 residues were shown to play essential roles in compound I and compound II formation (Dunford 1999). The mutation of arginine 104 and histidine 108 has been shown to be associated with disruption in Met-Tyr-Trp adduct formation, although the presence or absence of the adduct does not appear to correlate with INH resistance (Ghiladi et al., 2005).

The third category includes the mutants located at the proximal side of the heme (Figure 25b). The proximal mutants show significantly decreased catalase and peroxidase activity (Rouse et al. 1995; Rouse 1996).

The fourth type of mutation is the R418G mutation that is located in the U-shaped channel (Figure 20). This type of mutation shows abolished catalase activity but retained peroxidase activity (Mo 2004). The guanidino group of Arg418 forms a hydrogen bond with O<sup>η</sup> of Tyr229, the central residue of the Met-Tyr-Trp adduct. The N<sup>η2</sup> of Arg418 also forms a hydrogen bond to the amide nitrogen atom of Met255. Mutation of this residue may lead to disruption of the hydrogen-bond networks that are required for the formation of the adduct as well as for the catalase activity of the enzyme.

The remainder of the mutations appear to be located either on the surface of the protein or at the dimer interface, where they may play a role in the electron-transfer pathway, or in governing enzyme dimerization (Ghiladi et al., 2005). Comparison of catalase and peroxidase activity along with their INH sensitivity does not demonstrate an apparent correlation between catalase activity and INH resistance in this type of mutation.

### ***Structural Analysis of Substrate Soaked and Co-crystallized MtbKatG Crystals***

Table 6 lists the data sets that have been collected and processed for various substrates soaked or co-crystallized with *MtbKatG* crystals.

The structure of the wild-type *MtbKatG* crystal soaked with INH was investigated in order to elucidate the mechanism of INH activation. Crystals that were soaked for both short (5 min) and long (4 hr) durations with 10mM INH were analyzed. No significant change was observed in either structure. Although there were new electron densities

Table 5. INH sensitivity and catalase-peroxidase activity of *Mtb*KatG mutants

Classification	Mutation	Catalase activity $10^6 \times M^{-1} \cdot S^{-1}$	Peroxidase activity $10^4 \times M^{-1} \cdot S^{-1}$	INH sensitivity <sup>a</sup>	References
	wt <sup>b</sup> KatG	0.7	1.2	0.05 ug/ml	Saint-Joanis, 1999
Substrate channel	S315T	0.3	0.5	5 ug/ml	Saint-Joanis, 1999
Distal heme side	R104L	0.2	0.1	>500ug/ml	Rouse, 1996
	H108Q	ND	0.1	>500ug/ml	Rouse, 1996
	N138S	ND	0.1	>500ug/ml	Rouse, 1996
	A139V	0.6	0.4	0.1 ug/ml	Pym, 2002
Proximal heme side	H270Q	ND	0.1	>500ug/ml	Rouse, 1996
	W321G	ND	0.09 <sup>d</sup>	>500ug/ml	Mo, 2004
	D381G	ND	ND	>500ug/ml	Rouse, 1996
U channel	R418G	ND	0.6 <sup>d</sup>	<sup>e</sup>	Mo, 2004
others	S140N	1.5	1.6	0.5 ug/ml	Rouse, 1996
	T275P	ND	0.3	>500ug/ml	Rouse, 1996
	L148R	0.2	0.1	>500ug/ml	Rouse, 1996
	R463L	0.6	0.9	1.0 ug/ml	Saint-Joanis, 1999
	R463G	1.3	0.9	0.5 ug/ml	Rouse, 1996

<sup>a</sup> Data from (Rouse 1996; Pym 2002)

<sup>b</sup> wt, wild type.

<sup>c</sup> ND, not detected.

<sup>d</sup> data were converted for comparison.

<sup>e</sup> It did show INH resistance, however, the exact number was missed in the reference.

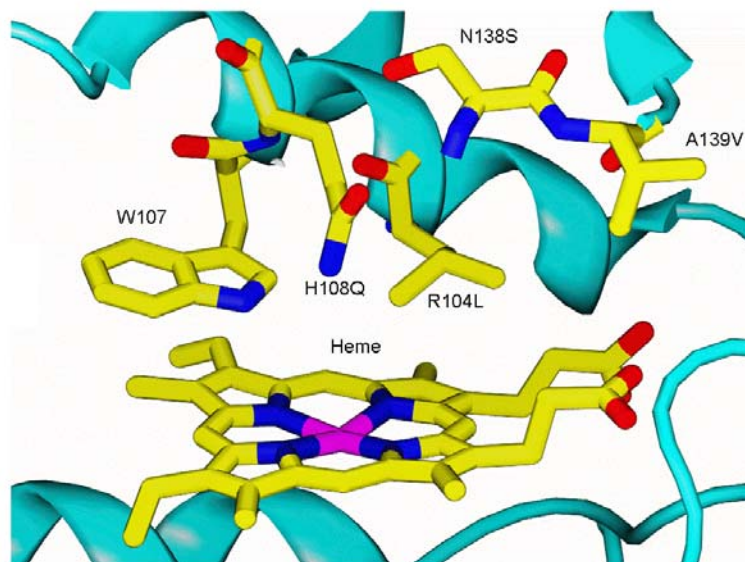
Table 6. Data collections and structure refinements for substrates soaked or co-crystallized *Mtb*KatG

	Beam line	Wave-length	Resolution Å	Completeness %	R-factor %	R-free %	Rmsd Å	Rmsd Angles	B-factor Å <sup>2</sup>
wtKatG + INH	DIP <sup>a</sup>	1.5	2.7	99	24.9	28.7	0.01	1.26	33
S315T +INH	IBT <sup>b</sup>	1.5	2.8	100	19.8	24.6	0.01	1.40	35
wtKatG + KCN	ALS <sup>c</sup>	0.9	2.0	97.8	27.4	31.7	0.08	1.59	30
wtKatG +KCN +INH	DIP	1.5	2.6	88.9	19.2	26.3	0.01	1.10	45
wtKatG +KCN +INH	IBT	1.5	2.7	99.5	18.5	23.1	0.01	1.26	23
wtKatG +KCN +INH co-crystl	DIP	1.5	2.9	88.6	20.1	27.3	0.01	1.12	41.5
wtKatG +INH	IBT	1.5	2.6	99.5	22.4	28.9	0.01	1.14	21
wtKatG +BHA	DIP	1.5	2.7	98.6	19.2	25.6	0.01	1.33	29
wtKatG +NADH	DIP	1.5	2.9	98.9	18.9	30.1	0.04	2.27	31
wtKatG +NAD <sup>+</sup>	IBT	1.5	2.3	92	37.4	41.7	0.04	2.75	27
wtKatG +NADH co-crystal	DIP	1.5	2.7	88.5	21.2	26.3	0.01	1.10	38

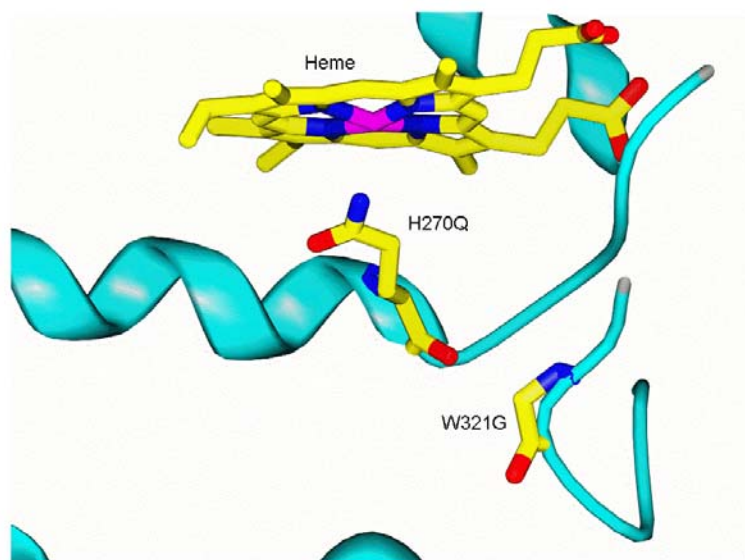
<sup>a</sup> Data collected using a MacScience DIP2030b image plate detector coupled with a Rigaku X-ray generator at Texas A&M University.

<sup>b</sup> Data collected using an R-axis IV ImagePlate at the Center for Structural Biology, Albert B. Alkek Institute of Biosciences and Technology (IBT).

<sup>c</sup> Data collected from the Advanced Light Source (ALS) at University of California, Berkeley.



(a). distal site mutations



(b). proximal site mutations

Figure 25. Structure modeling of clinically significant mutants. The figures were made using SPOCK.



found in both structures of INH soaked and co-crystallized crystals, the relative weaknesses of the density and its extent suggest either low occupancy or, possibly, multiple binding sites. We were unable to identify densities that could be confidently assigned to the drug molecule.

The oxidation of INH by *Mtb*KatG is an ongoing process and its product, the isonicotinic radical is not stable. This may contribute to the unsuccessful detection of a KatG-INH complex. Cyanide binds to the heme protein and is often used to probe the accessibility to the heme active site (Jakopitsch et al., 2005). It could be used to compete with INH for its binding site and slow down the rate of INH oxidization (Battistuzzi et al., 2005). 1 mM KCN was added to 0.3mM wtKatG enzyme and incubated on ice for 5 minutes before adding 10mM INH for the co-crystallization. The mixture was incubated for 30 minutes on ice and then crystallized in the same condition as that for the wild-type enzyme. Both KCN and INH plus KCN co-crystals were investigated.

X-ray diffraction data for the *Mtb*KatG co-crystallized with KCN-INH were collected using an in-house MacScience DIP2030b image plate detector coupled with a Rigaku X-ray generator at a resolution of 2.9 Å. A total of 120 frames were collected using one degree oscillation per frame under cryogenic conditions.

The overall structure of *Mtb*KatG-KCN-INH is the same as that of the wild-type enzyme. The rms deviation with respect to the wtKatG is 0.25 Å for 715 C $\alpha$  atoms from each subunit. The refined model of *Mtb*KatG-KCN-INH has a crystallographic R and R<sub>free</sub> factors of 20.1% and 27.3%. Other data collection and refinement statistics are similar to that in wt KatG (Table 7). The quality of the model was verified by

PROCHECK for the *Mtb*KatG-KCN-INH structure. An analysis of the main-chain geometry with a Ramachandran plot showed that all residues in both subunits fall within the energetically allowed region (Figure 26). There were no major conformational changes between structures of the wtKatG and the *Mtb*KatG-KCN-INH based on the analysis of the superimposed structures, especially at the distal heme binding pocket (Figure 27). The only exception was that the imidazole side-chain of His108 rotated about 15 degrees when compared with the *Mtb*KatG structure (Figure 27).

A region of undefined electron density was initially located in close proximity to the Pyrrole I of the distal heme after molecular replacement with the wtKatG and several refinements in CCP4. An unbiased electron density map was obtained using SHAKE&WARP. The resulting map showed an electron density that could contain an aromatic compound. The INH structure was fit and refined into the density (Figure 28). The pyridine ring of INH was parallel to the heme plane at distance of 3.6 Å. The distance between the carbonyl oxygen of INH and the heme iron is 3.7 Å. The surrounding region of the potential INH binding site was mainly composed of hydrophobic and aromatic residues including Ile228, Phe252, Tyr229, Trp107 and the heme. The pyridine ring of INH was also parallel to the indole ring of Trp107 at a distance of 3.2 Å. The carbonyl oxygen of INH was shown to form a hydrogen-bond to the N<sup>ε1</sup> of the indole of Trp107 (Figure 28). The pyridinyl nitrogen atom of INH was shown to form a hydrogen bond with the nitrogen atom of Tyr229 (Figure 28), the center residue of the Trp-Tyr-Met adduct. The carboxyl group of Asp 137 forms a hydrogen

Table 7. Data collection and structure refinement statistics for wt *Mtb*KatG-KCN-INH

A. Data collection statistics	
Wavelength	1.541
Unit cell parameters	
a	150.4
b	150.4
c	154.5
Space group	P42212
Resolution limits	2.9
Unique reflections	35205
Completeness	88.7 (62.4) <sup>a</sup>
Rsym <sup>b</sup> (%)	23.5 (68.1)
I/sigma	4.4 (1.2)
B. Refinement statistics	
Resolution range	30.0-2.9
Working set reflections	
Test set size	5%
R cryst <sup>c</sup> (%)	20.1
R free <sup>d</sup> (%)	27.3
Protein-non-H atoms	11771
Number of water molecule	633
Rmsd of bond distances (Å)	0.01
Rmsd of bond angles (deg)	1.12
Average B value	41.5

<sup>a</sup> Numbers in parentheses represent values in the highest resolution shell.

<sup>b</sup>  $R_{\text{sym}} = \frac{\sum_h \sum_i |I(h,i) - \langle I(h) \rangle|}{\sum_h \sum_i I(h,i)}$  where  $I(h,i)$  is the intensity value of  $I(h)$  for all  $i$  measurements.

<sup>c</sup>  $R_{\text{cryst}} = \frac{\sum ||F_o - F_c||}{\sum |F_o|}$ , where  $|F_o|$  and  $|F_c|$  are the observed and calculated structure factor amplitudes respectively.

<sup>d</sup>  $R_{\text{free}}$  is the same as  $R_{\text{cryst}}$  but calculated with 5% subset of all reflections that was never used in any refinement.

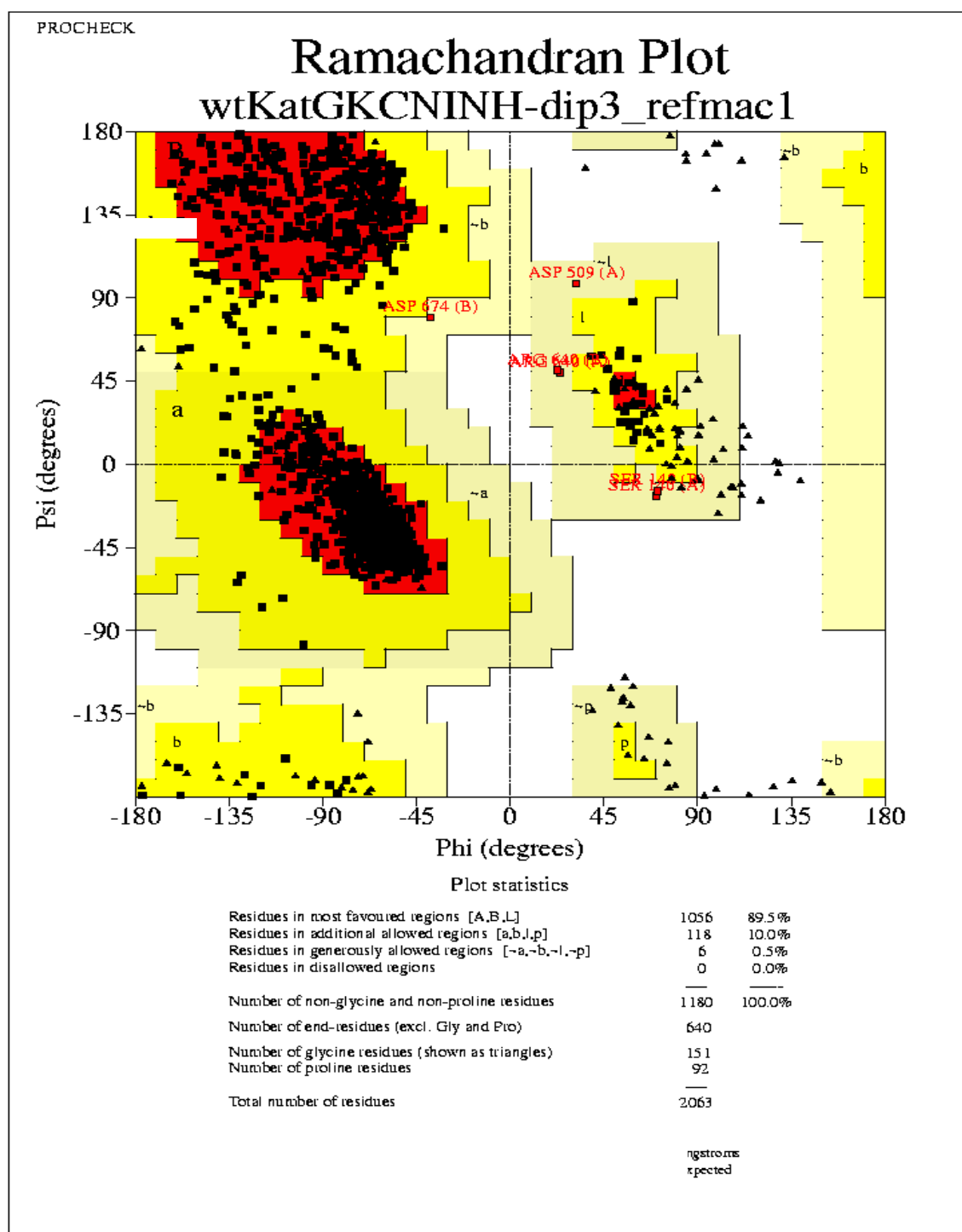


Figure 26. Ramachandran plot of *Mtb*KatG-KCN-INH structure. The figure was generated using PROCHECK.

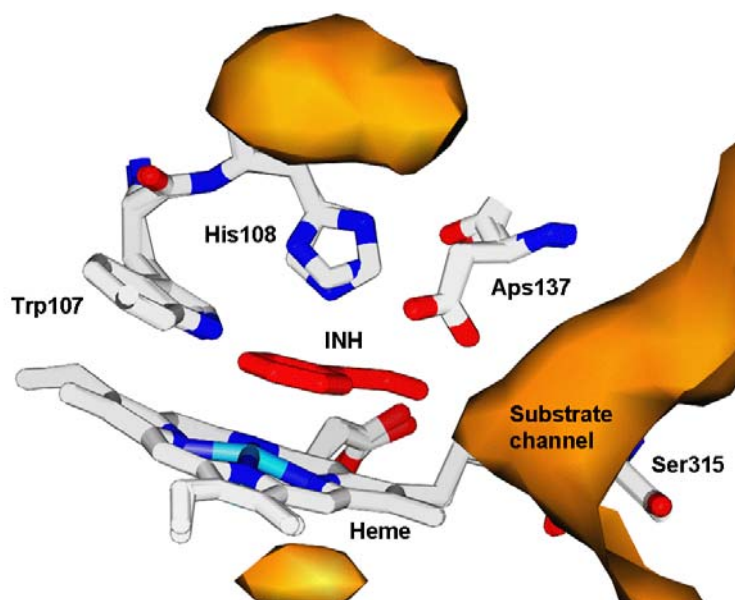


Figure 27. View of INH binding at the distal heme binding pocket in close proximity to the substrate channel. Superimposed *MtbKatG* and *MtbKatG*-KCN-INH residues at the active site were shown to be identical from the two structures with an exception of His108, which showed 15 degree rotation in the *MtbKatG*-KCN-INH compared to that of the *MtbKatG*.

bond to the nicotinamide-NH<sub>2</sub> group of INH. These interactions place INH in a remarkably good position for INH activation. Indeed, Asp137 has been proposed to play a key role in the binding and activation of INH (Jakopitsch et al., 2003b). A possible mechanism for the oxidation of INH might involve protonization or deprotonization by the Asp137 side-chain, polarization of the nicotinamide-NH-CO group resulting from electrons withdrawal by the Trp-Tyr-Met adduct or the electron-deficient heme, and the formation of the pyridine carbonyl and hydrazine radicals.

The density of KCN was not identified in the structure. One reason might be the resolution of the structure. The *MtbKatG*-INH-KCN data set was collected at home source to a resolution of 2.9 Å with average B factor of 41.5 Å<sup>2</sup>. It is not very reliable to define such a small molecule at this resolution. Another possible explanation is that KCN might have a low binding affinity to the heme at low pH (personal communication with Dr. Magliozzo). Studies have shown that pH affects the binding affinity of HCN to the cytochrome c peroxidase (CCP) (Foshay et al., 2004). In their studies, they also found that mutation of the distal histidine to lysine in CCP also affects the binding affinity of HCN to the enzyme. The distal mutant H52K has a higher affinity for HCN than does native CCP (Foshay et al., 2004).

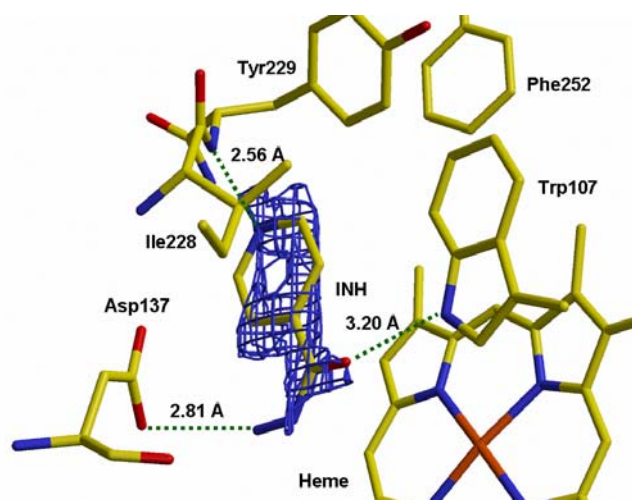


Figure 28. View of the environment surrounding INH binding site. The Fourier-difference map (Fo-Fc) was generated at 1  $\sigma$  contour level in Xtalview. Interactions of INH with its surrounding residues at the heme active site. The green dots indicate the possible hydrogen bonding interactions.

## Summary

In an effort to elucidate the molecular mechanism of INH activation and the relationship between drug resistance and the function of catalase-peroxidase, we have solved the X-ray crystallographic structures of the *Mtb*KatG, S315T mutant, and INH co-crystallized *Mtb*KatG. The crystals of *Mtb*KatG belong to space group  $p4_22_12$  with cell dimensions  $a=b=150$  Å,  $c=154$  Å,  $\alpha=\beta=\gamma=90^\circ$ . The structure of the wild-type enzyme was refined to a crystallographic R and  $R_{\text{free}}$  factors of 18.5% and 22.8%, respectively, to a resolution of 2.0 Å. The structure of the S315T mutant was refined to a crystallographic R and  $R_{\text{free}}$  factors of 23.0% and 27.6%, respectively, to a resolution of 2.1 Å. The overall structure of *Mtb*KatG[S315T] mutant is the same as the wild-type enzyme. The arrangement of catalytically important residues on both proximal and distal sides of the heme in KatG [S315T] is essentially the same as in the wild type enzyme. The distal side adduct of Trp-Tyr-Met side chains was found in both the wild-type and mutant structures. Our results provide a detailed picture on how the S315T mutation affects the function of the enzyme. The heme iron in the S315T mutant is 5-coordinate instead of 6-coordinate in the wtKatG. It has been shown that the oxyferrous wtKatG, either as Compound I or Compound II, is capable of oxidizing INH, while the oxyferrous KatG[S315T] is incapable (Ghiladi 2004; Ghiladi et al., 2005). The structures of the wild-type KatG and S315T mutant solved here suggest that the replacement of threonine for serine produces steric effects that interfere with interaction between the enzyme and INH but do not interfere with formation of Compound I from small peroxide molecule such as  $\text{H}_2\text{O}_2$ .

The drug binding within the heme pocket is a likely requirement for INH activation (Zhao et al., 2006).

The structure of the wtKatG co-crystallized with INH was investigated to identify the substrate binding site in the enzyme. The wild-type enzyme was treated with KCN, an inhibitor for a heme containing enzyme, before the co-crystallization with INH. The overall structure of the wtKatG-INH remained the same as that of the wtKatG. An INH molecule was fitted and refined into a region of electron density located in close proximity to the Pyrrole I of the distal heme. The pyridine ring of INH is located parallel to the heme plane. The carbonyl oxygen of INH forms hydrogen bond with N<sup>ε1</sup> of the indole ring of Trp107 and the pyridinyl nitrogen of INH forms hydrogen bond with the nitrogen atom of Tyr229. Both Trp107 and Tyr229 are involved in the distal adduct formation. The nicotinamide-NH<sub>2</sub> group of INH forms a hydrogen bond with the carboxyl group of Asp137, a key residue that has been proposed to play a role in the binding and activation of INH (Jakopitsch et al. 2003b). Our data revealed an excellent position for INH binding and activation through interaction with Asp137 and the distal adduct, although the electron density for the INH molecule is weak. Future work would be to determine structures of Compound I, Compound II and Compound III by using the KatG[Yy229F] mutant to elucidate the catalytic mechanism of the enzyme.



## CHAPTER IV

### STRUCTURAL AND FUNCTIONAL STUDIES OF VIRB11 FROM *BRUCELLA ABORTUS*

#### Introduction

VirB11 is a putative ATPase localized to the cytoplasmic side of the inner membrane (Thorstenson et al., 1993). The function of VirB11 is essential for the virulence of many pathogenic bacteria including *Helicobacter pylori*, which causes gastritis and peptic ulcers, *Bordetella pertussis*, which is responsible for whooping cough, and *Brucella spp*, which causes animal brucellosis (Covacci et al., 1999; O'Callaghan et al., 1999; Delrue et al., 2001; Baron et al., 2002; Schulein and Dehio 2002; Cascales and Christie 2004; Celli and Gorvel 2004). It has been proposed that VirB11 either acts as an assembly factor for the T4SS or that it is responsible for the translocation of substrate molecules across the membrane (Sagulenko et al., 2001). VirB11 is required both for pilus biogenesis and substrate secretion. Studies have shown that certain amino acid substitutions in VirB11 enables T-DNA transfer without pilus formation suggesting that VirB11 has dual functions (Sagulenko et al., 2001).

It has been suggested that putative ATPases from the type II and type IV secretion systems are evolutionarily related based on the identity and similarity scores from the sequence comparisons (Segal et al., 1999; Planet et al., 2001). Sequence alignments of VirB11 from several bacteria species are shown in Figure 29. Four conserved domains

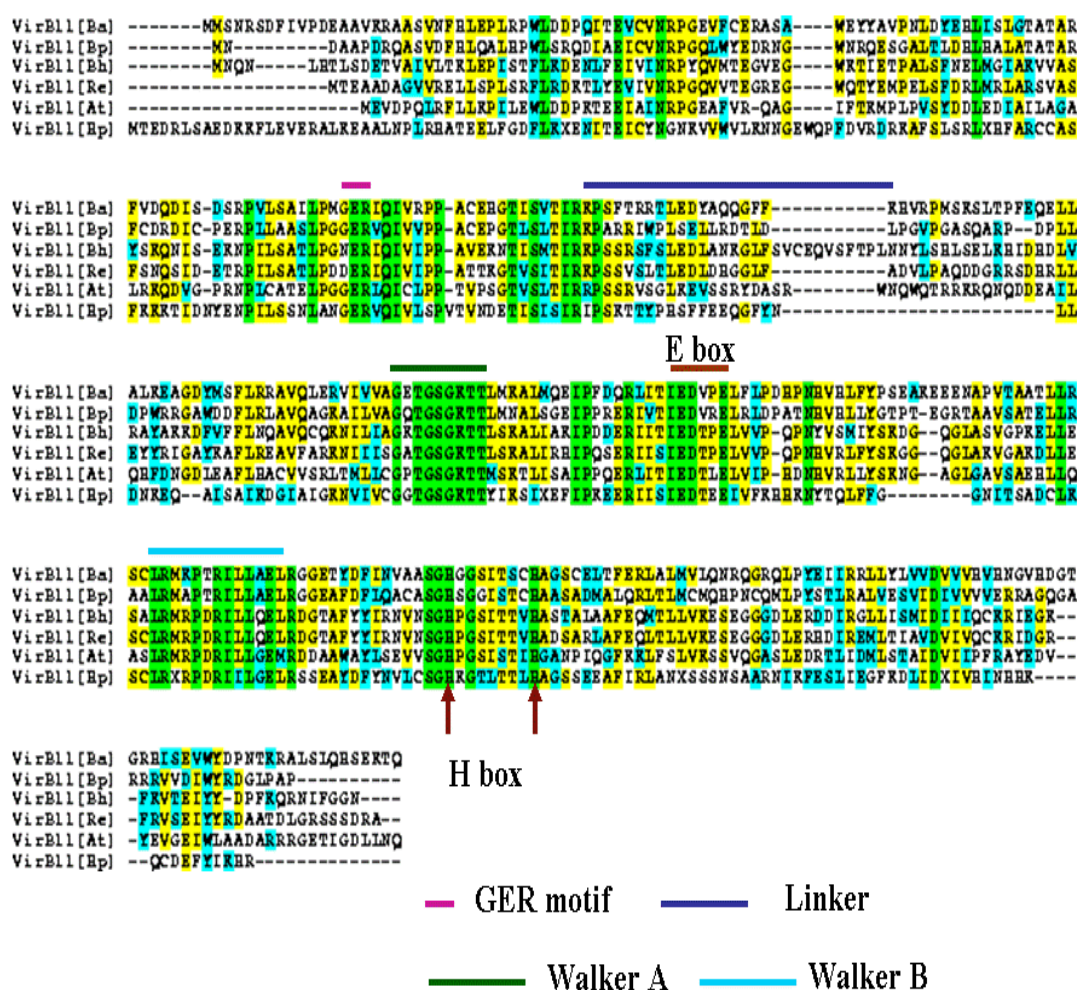


Figure 29. Sequence alignments of VirB11 from several bacterial species. The figure was generated using the Clustalw multiple sequence alignment program in Biology Workbench. VirB11 [Ba]: VirB11 from *Brucella abortus*; VirB11 [Bp]: VirB11 from *Bordetella pertussis*; VirB11 [At]: VirB11 from *Agrobacterium tumefaciens*; VirB11 [Hp]: VirB11 from *Helicobacter pylori*; VirB11 [Bh]: VirB11 from *Bartonella henselae*; VirB [Re]: VirB11 from *Rhizobium etli*.

have been found in all superfamily members, a Walker box A, a Walker box B, an Asp (or Glu) box and a His box (Rivas et al., 1997; Planet et al., 2001). Other amino acid sequences are also highly conserved, especially in the C-terminal domain. However, the linker region between the N-terminal and the C-terminal domain is less conserved (Figure 29). The exception is that Arg120, the first residue at the linker, is highly conserved. Other common features of the VirB11-like proteins include the lack of a transmembrane domain and amino-terminal export peptide signals.

VirB11 is thought to interact with other VirB proteins and undergo ATP-dependent conformational changes that are required for substrate transfer and pilus formation (Krause et al., 2000). It has been shown that VirB11 interacts with VirB4 directly to catalyze the substrate transfer to the VirB6 and VirB8 inner membrane channel in *Agrobacterium*. Studies also have shown that VirB11 interact with VirB1 (Hoppner et al., 2005).

The crystal structures of HP0525, a homolog of VirB11 in *H. pylori*, in complex with ADP or ATP $\gamma$ S, have been solved (Yeo et al., 2000; Savvides et al., 2003). The structure reveals that the protein is a homohexamer formed by double-stacked rings. Each monomer of the homohexamer is capable of binding a molecule of ATP at the interface between the N-terminal and C-terminal domains (Yeo et al., 2000). In the hexamer, the amino- and carboxyl-terminal domains form two rings, open on one side and closed on the other. It has been proposed that HP0525 functions as an inner membrane pore that opens and closes in response to ATP binding and hydrolysis (Krause et al., 2000). The structure of apo-HP0525 is significantly different from that of ADP-HP0525 complex,

revealing an asymmetric hexameric assembly, suggesting that the hexamers undergo dynamic conformational changes with cycles of ATP binding and ADP release (Savvides et al., 2003). The structures of ADP and ATP $\gamma$ S complexes are identical with rmsd 0.5 Å for 323 C $\alpha$  atoms, suggesting that nucleotide binding is responsible for ATP-induced conformational changes, not the product release (Savvides et al., 2003).

*Brucella* species are intracellular pathogens that cause long-lasting debilitating infections via inhalation of aerosolized particles. Lack of human brucellosis vaccine and the serious consequence of the disease have led to their recent classification as class B agents of bioterrorism. A fully functional T4SS is essential for bacterial survival. The spread of antibiotic resistant genes can also be attributed to the T4SS mechanism (Cascales and Christie 2003). VirB11 is one of the essential components of T4SS and presents a promising target for novel antimicrobial drug design. Understanding the molecular basis for the VirB11 of *B. abortus* requires a detailed analysis of the structure of VirB11 and its complexes with inhibitors and substrates. The function of VirB11 as an ATPase may vary from one organism to another depending on the type of effector molecules transported. In contrast to VirB11 of HP0525, in which the ATPase is mediating the 40 kDa CagA protein, the effector molecules that are transferred by VirB11 in *Brucella abortus* have not yet been identified. The primary aim of this study is to solve the crystal structure of VirB11 from *B. abortus*. The molecular features and structural determinants that dictate the activity of VirB11 may be elucidated from our structural studies and serve as the basis for understanding the mechanism of VirB11 in *B. abortus* virulence factor translocation.

The crystal structure of VirB11 from *H. pylori* revealed one ATP binding per monomer molecule. The functional roles of the second ATP binding motif, the Walker B motif, and the His box at the C-terminal domain were not clear. In an effort to better understand the molecular function of the *BaVirB11* and to test which functional groups are required for the ATPase activity of *BaVirB11*, seven mutants were generated based on the protein sequence alignment analysis (Table 8). The mutations include a GER motif mutation, a linker region mutation, a His box mutation, and a Walker A motif mutation. The presence of the nucleoside triphosphate binding motifs in all VirB11 proteins from different bacterial species reflects a common requirement for an energy source to drive the macromolecular translocation in the T4SS (Krause et al., 2000). Mutations of the conserved Walker A motifs were shown to abolish ATP binding and ATPase activities of *BaVirB11* and block the secretion of the substrates in *Brucella spp.* (Christie 1989; Turner et al., 1993; Stephens et al., 1995). In our studies, Walker A mutant K188Q showed dramatically decreased ATP hydrolysis activity due to the decreased ATP binding affinity to the mutant enzyme. These results along with the wild-type enzyme control were used to validate our experimental methods for testing other mutants on ATP binding and ATP hydrolysis activities. A linker region between the N-terminal domain and the C-terminal domain was shown to have a rigid-body rotation upon ATP binding and hydrolysis (Savvides et al., 2003). However, it is not known if the ATP binding or the ATP hydrolysis is the source for the rigid-body rotation. Surprisingly, the linker region mutation showed no effect on ATP binding but dramatically decreased ATP hydrolysis activity was found in our study, indicating it is

not directly involved in ATP binding. Structural analysis showed that Arg120 is shifted further away from the ATP-binding site and its side chain is located outside the coordination sphere of the ATP binding site as predicated from HP0525-ATP $\gamma$ S structure. The GER motif is conserved in VirB11 throughout type IV secretion systems. Similar motifs from human collagen type III and IV were shown to be responsible for protein-protein interaction, in which it bound to human integrin in a Mg<sup>2+</sup>-dependent manner (Raynal et al., 2006). R113 of HP0525 was proposed to play dual roles in ATP binding and hydrolysis: to provide complementary electrostatic interaction with ATP  $\gamma$ -phosphate and to interact with the catalytic Glu248, a conserved E box residue (Savvides et al., 2003). An equivalent mutant R101K of *Ba*VirB11 was generated to test this hypothesis. The R101K mutant was found to display a similar ATP binding affinity as the wild-type enzyme and abolished ATP hydrolysis activity, indicating that direct interaction of Arg 101 with the catalytic Glu is crucial for ATP hydrolysis activity. Based on our finding, we further proposed that the GER motif and the linker region are not directly involved in ATP binding. However, once an ATP binds, its negatively charged phosphate group interacts with the positively charged guanidine group of Arg in the wild-type enzyme. This interaction brings the N-terminal domain to its closed conformation through the flexible linker. The interactions are disrupted in the R120E and R101K mutants resulting in the N-terminal domains remain in their opened conformation.

Table 8. VirB11 mutants generated in this study

Mutant type	Mutation	Function	Reference
GER motif	R101K	Protein-protein Interaction;  ATP binding and hydrolysis	Raynal 2006  Savvides 2003
Linker region	R120E	Decrease in ATPase activity in HP0525, no effect on dimerization	Savvides 2003
Walker A	K188Q	ATP binding and hydrolysis	Christie 1989
Walker B	I281T	Abolishing in T-pilus formation	Sagulenko 2001
H box	H285R	Decrease in Pilus formation	Sagulenko 2001

## Materials and Methods

### *Enzymes, Chemicals, and Reagents*

Restriction endonucleases were purchased from Promega (Madison, Wis.) and New England Biolabs (Beverly, Mass.). Klenow fragment of *Escherichia coli* DNA polymerase I and T4 DNA ligase were purchased from New England Biolabs. PCR QuickChange® site-directed mutagenesis kits were obtained from Strategene. The

complementary pairs of oligonucleotide primers used for mutagenesis were synthesized by the Integrated DNA Technologies (IDT), Inc. (Woods Land, Texas). A peptide which contains seven amino acid residues from *BaVirB1* was synthesized by Sigma-Aldrich Chemical Co. (St. Louis, Mo.). Isopropyl- $\beta$ -D-thiogalactopyranoside, (IPTG), phenylmethylsulfonyl fluoride (PMSF), carbenicillin, kanamycin, Coomassie brilliant blue R250, malachite green, polyvinylalcohol, 5-bromo-4-chloro-3-indolylphosphate, desthiobiotin, 2-[4-hydroxy-benzenazo]-benzoic acid, ammonium molybdate tetrahydrate, ATP-agarose beads, glutaraldehyde, and selenomethionine were purchased from Sigma-Aldrich Chemical Co. Other common chemicals were obtained from VWR. A Bradford protein assay kit was from Bio-Rad Laboratories (Hercules, Calif.). Strep-Tactin Sepharose was purchased from IBA BioTAGnology (Germany). A Superdex200<sup>TM</sup> gel filtration column was from Pharmacia Biotech (Piscataway, N.J.).

### ***Plasmids and Bacteria Strains***

The pT7-7StrepII-VirB11 plasmid for the production of *Brucella abortus* VirB11 protein was kindly provided by Dr. Renee Tsois of University of California, Davis. The construct contains a N-terminally tagged StrepII followed by a Factor Xa cleavage site and the full length VirB11 gene (Hoppner et al., 2005).

The *E. coli* strain NovaBlue single® was used for plasmid transformation and manipulation and BL21(DE3) Novagen<sup>TM</sup> and B834(DE63) were used for protein overexpression.



### ***Mutagenesis***

The site-directed mutations in *BaVirB11* were generated following the PCR QuickChange® site-directed mutagenesis protocol of Stratagene. The pT7-7strep-VirB11 plasmid was used as the DNA template. The complementary pairs of oligonucleotides listed in Table 9 were used for the PCR amplification. For each 50ul reaction, it contained 800uM of the four (d)NTP, 10pmol of each primer, 1mM MgCl<sub>2</sub>, 1nmol of the template DNA and 1ul of Pfu (*Pyrococcus furiosus*) DNA polymerase from Stratagene. The PCR products were digested with the Dpn I restriction enzyme to break down the methylated parental template DNA before their transformation into Nova Blue competent cells (NovaGene). Five colonies from each mutant transformate were selected from LB plates supplemented with Carbenicillin (50ug/ml). Plasmid DNA was purified using the mini-prep kit from Qiagen. Mutations were confirmed from sequence analysis using the T7 promoter primer.

### ***Bacteria Culture***

The bacteria were grown overnight at 37 °C on Luria-Bertani (LB) agar plates (1 % tryptone; 0.5 % yeast extract; 0.5 % NaCl; 1.5% agar) containing carbenicillin (100 ug/ml). A single colony was picked to grow each 5ml culture in LB media containing 100ug/ml carbenicillin at 37 °C in a shaker at 200 rpm. 2 liter cultures were inoculated with the same media under vigorous shaking at 37 °C. When the cell density reached

Table 9. PCR primers used to generate *Brucella* VirB11 mutants

Primer name	Sequence	Mutant name
K188Qf K188Qr	CGAGACGGGATCAGGCCAGACCACACTGATG CATCAGTGTGGTCTGGCCTGATCCCGTCTCG	K188Q
$\Delta$ -GKT <sub>(187-189)</sub> f $\Delta$ -GKT <sub>(187-189)</sub> r	GGCGAGACGGGATCAACACTGATGAAAGCG CGCTTTCATCAGTGTGATCCCGTCTCGCC	$\Delta$ -GKT <sub>(187-189)</sub>
I281Tf I281Tr	CATGGCGGCAGCCTCACCAGTTGC GCAACTGGTGAGGCTGCCGCCATG	I281T
H285Rf H285Rr	ATCACCAGTTGCCGAGCCGGTTCGTGCG CGCACGAACCGGCTCGGCAACTGGTGAT	H285R
R120Ef R120Er	TCACGATCGAGAAGCCGTCTTTCACCCG CGGGTGAAAGACGGCTTCTCGATCGTGA	R120E
$\Delta$ -IR <sub>(119-120)</sub> f $\Delta$ -IR <sub>(119-120)</sub> r	ATCTCGGTTACGAAGCCGTCTTTCACCCG CGGGTGAAAGACGGCTTCGTAACCGAGAT	$\Delta$ -IR <sub>(119-120)</sub>
E209Kf E209Kr	CGCCTGATCACCATCAAGGACGTACCGGA TCCGGTACGTCCTTGATGGTGATCAGGCG	E209K
R101Kf R101Kr	CCTGCCGATGGGTGAGAAGATTGAGATTGTG CACAATCTGAATCTTCTACCCATCGGCAGG	R101K
$\Delta$ -ER <sub>(109-101)</sub> f $\Delta$ -ER <sub>(109-101)</sub> r	CCTGCCGATGGGTATTGAGATTGTGCGCCC GGGCGCACAATCTGAATACCCATCGGCAGG	$\Delta$ -ER <sub>(109-101)</sub>

OD<sub>595</sub> = 0.7-0.9, the culture flasks were placed on ice for 20 min to bring the culture to 18-20 °C. Protein expression was induced by adding 0.5 mM isopropyl-b-D-thiogalactoside (IPTG) to the culture and continued incubation at 18 °C under vigorous shaking for 12-16 hours. For overexpression of the selenomethionine (SeMet) labeled VirB11 and the VirB11[R120E] mutant protein, a 5ml LB culture from a single colony

was grown overnight at 37 °C. B834(DE63) cells were collected from the 5 ml LB media and used for inoculation of 2 liter LB culture. The cells were centrifuged in sterilized centrifuge bottles when OD<sub>595</sub> reached to 0.6-0.9 and then gently pelleted and washed with minimal media (M9). The cells were re-suspended in two of the 2 liter M9 media supplemented with 50ug/ml Carbenicillin and 100ug/ml of 19 amino acid mix and 40 ug/ml SeMet and grown two more hours to let OD<sub>595</sub> reach to 0.6-0.9 before inducing with 1 mM IPTG. The induction was carried out at 18 °C for 12-16 hours.

### ***Protein Purifications***

For Strep-Tactin Sepharose chromatography, bacterial cells (from 4 liter culture) were suspended in 40 ml ice-cold StrepII binding buffer containing 100 mM Tris-HCl, pH8.0, 150mM NaCl, 1 mM EDTA, plus 0.5 mM PMSF (phenylmethlsulphonylfluoride) and passed twice through a French pressure cell at 1000 p.s.i. The lysate was centrifuged (SS34 rotor, 60 min, 15 000 r.p.m. at 4 °C) to remove cell debris and unbroken cells. The N-terminal StrepII-fusion proteins were purified with a 4ml Strep-Tactin column following the instructions of the manufacturer (IBA) with some modifications. Specifically, the column was equilibrated with 5 bed volume of ice-cold StrepII binding buffer (100 mM Tris-HCl, pH8.0, 150mM NaCl, 1 mM EDTA). Cell extract was applied to the pre-equilibrated column and washed with 10 bed volumes of washing buffer containing 100mM Tris-HCl, pH8.0, 1M NaCl, and 1mM EDTA and then 5 bed volumes of binding buffer before elution with 2.5mM desthiobiotin (Sigma). The column can be regenerated using 1mM 2-[4-hydroxy-benzenazo]-benzoic acid and re-

equilibrated with 10 bed volumes of water. The fractions were collected and analyzed by SDS-polyacrylamide gel electrophoresis. The samples were pooled, dialyzed and concentrated to 7-10m/ml in a buffer containing 25mM Tris/HCl, pH8.0, 1 mM EDTA and 1mM DTT. Protein concentrations were determined using the Bradford dye binding assay (Bio-Rad) with bovine serum albumin as a reference.

The sample generated by affinity chromatography was applied to a pre-equilibrated Superdex200<sup>TM</sup> gel filtration column (100/16 XK) operated by an HPLC system (Amersham Pharmacia Biotech) using a buffer containing 25 mM Tris-HCl, pH8.0, 1mM EDTA, 1mM DTT. Proteins were eluted at a flow rate of 0.3ml/min and 2-ml fractions were collected. The same buffer and flow rate was used to calibrate the gel filtration column for the calculation of the molecular weight of the protein. The “gel filtration Calibration Kit” from Amersham Pharmacia Biotech was used for the molecular weight calibration. The molecular weight of proteins in the kit ranged from 13.7 to 669 kDa.

The pooled fractions were dialyzed for 4 hours or overnight against a buffer containing 25 mM Tris-HCl, pH8.0, 1mM EDTA, 1mM DTT. The protein sample was concentrated using an Amicon Ultra-15 (Millipore) centrifugal filter with 30kDa minimal molecular weight cut off. The freshly purified proteins were used for crystallization and ATP hydrolysis studies.

### ***Colorimetric ATPase Activity Assay***

The malachite green based colorimetric assay was used to measure inorganic phosphate released by the ATPase activity of VirB11 (Cogan et al., 1999). The colorless phosphomolybdate complex is formed at a low pH and then converted to a colored complex in the presence of an enhancer, the basic pH indicator dye malachite green. The phosphomolybdate complex is quantified spectrophotometrically.

The Malachite Green Reagent I was prepared by dissolving 50 mg malachite green (final concentration 0.76mM) and 0.17g polyvinylacohol (0.35% final concentration) in 50ml of water and filtering through 0.45um filter. The Malachite Green Reagent II contains 28mM ammonium molybdate tetrahydrate in 2.1M H<sub>2</sub>SO<sub>4</sub>. Equal volumes of the Malachite Green Reagent I and II were mixed right before the color development.

To prepare phosphate standards, sodium dihydrogen orthophosphate monohydrate (NaH<sub>2</sub>PO<sub>4</sub>·H<sub>2</sub>O) was dried overnight in an oven at 110° to remove water prior to making up standard solutions. A 1mM stock solution was prepared and a series dilution was obtained (500, 250, 150, 100, 50, 25, and 5uM stocks).

10xATPase Assay Buffer containing 100mM Tris-HCl, 100mM NaCl, 20mM MgCl<sub>2</sub>, 10mM DTT at pH 7.5 and 1mM ATP stock solution was prepared prior to the assay. The stop Buffer contained 0.5 M EDTA at pH 8.0. VirB11 enzyme of 10nM concentration was pre-incubated in a 1xATPase assay buffer for 10 minutes before the reaction.

The assay was performed in triplicate. Each reaction mix consisted of 200ul of 10x ATPase assay buffer, 200ul of the enzyme, 200ul of 1mM ATP and 1.5ml of water. For

those samples incubated with an inhibitor or a stimulator, the water volumes were changed accordingly. The phosphate standards were prepared in triplicate from the seven 5x stocks (described above) by addition of 400  $\mu$ l of each 5x phosphate standard to tubes containing the complete assay buffer, bringing their final volume to 2ml. The reaction mixtures were incubated at 30° for 5, 10, 20, 30, 60, 90 minutes. At each time interval, 200 $\mu$ l of each reaction mixture were transferred into 50  $\mu$ l of stop buffer, including the phosphate standards. The reaction was terminated by adding 100  $\mu$ l of stop buffer at 5 second intervals to all reactions, including the phosphate standards. 1.5ml of the Malachite Green Reagent was added to each reaction tube, mixed, and the color was allowed to develop for 5 min. The absorbance of the samples was read on a spectrophotometer at a wavelength of 610 nm. There are essential control conditions for the assay to eliminate contaminating background phosphate. Two control experiments were included in the ATP hydrolysis activity assays. A sample with the complete assay buffer components (but no VirB11) is required to account for spontaneous ATP hydrolysis. This was used as the blank on the spectrophotometer. The second control was to estimate the free phosphate contamination in the buffer system. In this control, the VirB11 was included in the assay buffer and the ATP substrate was left out.

### ***ATP Binding Assay***

ATP binding assays were performed following the protocol of Sexton (Sexton et al., 2004) with minor modification. 100 $\mu$ l of ATP-agarose beads (Sigma) were pre-washed with an ATP-binding buffer containing 25mM Tris-HCl, pH 8.0, 20mM NaCl, 1mM

EDTA, 1mM DTT, and 2mM MgCl<sub>2</sub>. 15ug of each protein sample was added to the ATP-agarose and incubated on ice for 30 minutes. The ATP-agarose beads were washed twice with an ATP-washing buffer containing 25mM Tris-HCl, pH 8.0, 0.5M NaCl, and 2mM MgCl<sub>2</sub>. The ATP-agarose-bound proteins were eluted by adding 100ul of 10mM ATP in an ATP-binding buffer and incubated for 30 minutes. The eluted proteins were boiled in a SDS-gel-loading buffer for 5 minutes. The samples were run on 12-15% SDS-PAGE and stained by Coomassie blue.

### ***Covalent Cross-linking of VirB11 subunits***

The covalent cross-linking experiments were carried out to determine the oligomer state of VirB11 mutants following the protocol of Krause (Krause et al., 2000). 15uM VirB11 and its mutants were incubated with various concentrations (100; 300; 500uM) of glutaraldehyde at 25 °C for 90 minutes in the buffer containing 20mM sodium phosphate, pH 7.0, 1 mM DTT, 50mM NaCl, 50% glycerol, 10mM MgCl<sub>2</sub>, and 0.5mM ATP. Reactions were stopped with 3.5M urea (final concentration). Denatured samples were subjected to SDS-electrophoresis and the gels were stained with Serva Blue R.

### ***Crystallization and Data Collection***

Sitting-drop vapor diffusion crystallization screenings were performed by using HYDRA 96 high-throughput robotic system (Robbins Scientific) with commercially available screens from Hampton Research (Crystal Screen 1&2, MembFac, and PEG/Ion crystal

screen kits). Equal volumes (1  $\mu$ l) of protein solution at 7mg/ml concentration were mixed with a reservoir solution containing ionic solvent with varied pH, precipitant, and additive.

*B. abortus* VirB11 native crystals were obtained at 18 °C from a solution containing 10% w/v PEG-4000, 0.1M HEPES, pH7.5, 0.1 M NaCl. Small plate-like crystals formed in a few days. Larger plate-like crystals grew in the well in which an additional 10% protein was added two weeks after the initial crystal plate set-up. The Se-Met derivative crystals were formed in the solution containing 10% w/v PEG-4000, 0.1M HEPES, pH7.5, 0.1M NaCl, 1mM MgCl<sub>2</sub>, 3% ethanol at the protein concentration of 9 mg/mL.

ATP analogous inhibitor bound crystals were also obtained with the same condition as used for Se-Met VirB11 in presence of 5mM Amp-PCP or 5mM ADP $\beta$ S.

The crystals were flash cooled to 120K after the progressive transfer to a series of cryoprotectant solutions containing 15 to 35% ethylene glycol in mother liquor. Crystals of the native and the Se-Met derivative VirB11 belong to space group C2 with unit cell dimensions of  $a=123.1$  Å,  $b=233.2$  Å,  $c=107.3$  Å, and  $\beta=123.6^\circ$ . The solvent content of the unit cell was estimated to be 52%, with six molecules per asymmetric unit. A set of high resolution data was collected to 2.7 Å at Beamline 19ID, the Advanced Photon Source in Chicago. Initial molecular replacement methods failed to produce any solution using the homolog model, HP0520 as the search model. Later, MAD data were collected to a resolution of 2.9 Å at Beamline 23ID, Structural Biology Center at the Advanced Photon Source in Chicago. This single crystal was used for MAD data sets collection at



the wavelength of  $\lambda=0.936$ ,  $0.979$ , and  $1.005$  Å, respectively. Diffraction data were indexed and integrated using program HKL2000. Attempts to use multiple wavelength data sets to solve the structure were not successful due to the weak diffraction nature of the *BaVirB11* crystals. Data analysis shows the anomalous signal is only good to  $5.3$  Å between data sets collected at the peak and the inflection wavelength. In addition, out of more than 100 crystals screened, only a few diffracted to resolution higher than  $4$  Å, and most of the diffracting crystals were highly mosaic with mosaicity range from  $1.5$  to  $6$  degrees. The analysis of the Patterson function by XTRIAGE (Zwart et al., 2005) revealed a significant off-origin peak (21%), indicating possible pseudo translation symmetry.

Hexagonal shaped crystals were obtained from a solution containing 18%PEG400, 0.1M HEPES, pH7.5, and 0.1M  $\text{MgCl}_2$ . The native diffraction data used to solve the structure of *BaVirB11* was collected on an R-AXIS image plate detector (Rigaku-MSD) at the wavelength  $1.5418$  Å. The crystal were formed in a solution containing 5mM *BaVirB1* peptide that has been shown to interact with VirB11 (Hoppner et al., 2005). A total of 180 frames have been collected at 1 degree oscillation. Integration and scaling of the X-ray data was performed using the HKL2000. The hexagon crystal belongs to space group R3 with unit cell dimensions of  $a=110.58$  Å,  $b=110.58$  Å,  $c=347.29$  Å, and  $\alpha=90^\circ$ ,  $\beta=90^\circ$ , and  $\gamma=120^\circ$ . The solvent content of the unit cell was estimated to be 50.4%, with four molecules per asymmetric unit.

### ***Structure Determination and Refinement***

The structure of *BaVirB11* was solved using a local collected data set that resulted in space group (R3) to a maximum resolution of 3.6 Å. An initial structural search model was constructed from HP0520 (PDB access code: 1OPX) by deleting the N-terminal domain and converted those non-conserved C-terminal domain residues into alanine. Molecular replacement searches were carried out in PHASER (McCoy et al., 2005) using the mixed C-terminal domain as the search model. Initial refinement was performed using Phenix-refine in Phenix packages (Adams et al., 2002). The refined map was used for *auto-tracing* to convert all residues into *BaVirB11* sequence. The *auto-tracing* was carried out in program COOT (Emsley and Cowtan 2004). The resulting model was further refined using simulated annealing in Phenix. An unbiased map obtained from SHAKE&WARP and a 2Fo-Fc map from REFMAC was used for model building using XTALVIEW. The missing N-terminal domain was slowly built in and the refined model was used as a search model for molecular replacement searches using the high resolution data set (2.7 Å) collected from 23ID beam line at APS, Chicago. The model building and refinements were carried out in Xtalview and REFMAC in CCP4.

## Results and Discussion

### *Protein Purification*

In order to carry out structural studies of VirB11, it is essential to produce large quantities of highly pure (>95%) protein. The solubility and expression level of *B. abortus* VirB11 are low. To overcome this problem, protein expression was induced with 0.5M IPTG at 16.0 °C for 12-16 hours.

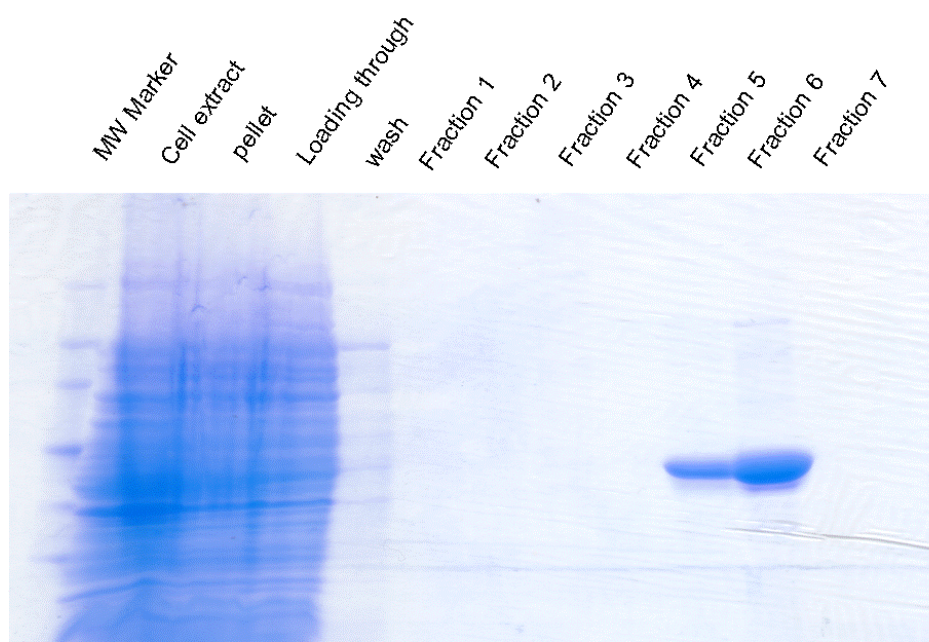


Figure 30. One step Strep-tactin affinity purification of *BaVirB11*. The collected fractions were analyzed by SDS-polyacrylamide gel electrophoresis and stained by Coomassie blue.

The N-terminal StrepII-fusion proteins were purified through a Strep-Tactin column (4ml). The purification protocol was modified to improve the purity of the protein by increasing the washing stringency with a high salt buffer. The Strep-Tactin column was washed again with a low salt buffer before eluted with 2.5mM desthiobiotin. The modified purification protocol allows us to obtain over 95% pure proteins from single step purification (Figure 30).

The Strep-Tactin column purified VirB11 was also subjected to Superdex200<sup>TM</sup> gel filtration chromatography. VirB11 eluted from Superdex200 gel filtration appears to form hexamers as indicated by the molecular weight marker (Figure 31). The chromatography of the gel filtration purification is shown in figure 32 with the calibrated molecular weight marker indicated. However, the protein purified from a gel filtration column did not form crystals.

The mutant proteins were over-expressed and purified by a one step Strep-Tactin purification protocol as used for the wild-type enzyme. However, three amino acid deletion mutants  $\Delta$ -GKT<sub>(187-189)</sub> and  $\Delta$ -IR<sub>(119-120)</sub> showed little expression in *E. coli* and failed to be purified to large quantity for further studies.

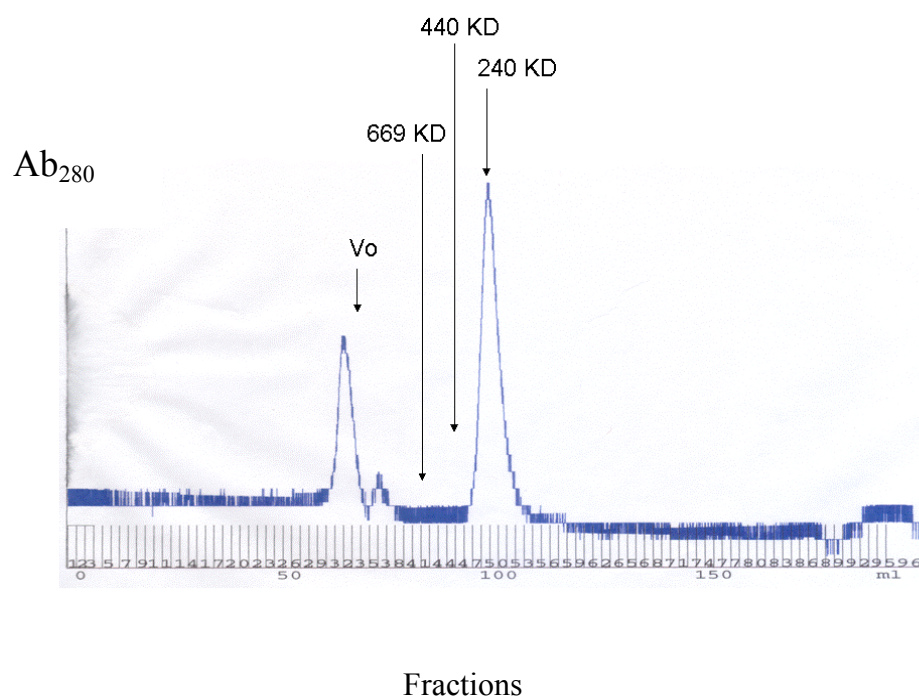


Figure 31. Chromatography of the gel filtration purification. The arrows indicate the size of the elute based on the gel filtration calibration. Vo represents the molecules eluted at void volume.

### ***Colorimetric ATPase Activities and ATP-agarose Binding Studies***

To gain insight into the domain requirement for *BaVirB11* function, seven functional mutations of *BaVirB11* were generated (Table 8), isolated and tested for their ATPase activities and ATP binding affinities. Two of the double mutants  $\Delta\text{-GKT}_{(187-189)}$  and  $\Delta\text{-IR}_{(119-120)}$  produced little soluble proteins and were not included in the biochemical characterization.

ATPase activity was determined by measuring the release of phosphate ions that are the result of ATP hydrolysis. Formation of the green-colored phosphomolybdate-Malachite green complex was detected by a spectrophotometer at OD<sub>610</sub>. A standard curve was performed using KHPO<sub>4</sub> solutions of known concentrations and was used to determine the amount of phosphate released in the assay. The relative ATPase activity was calculated with the wild-type enzyme activity as 100%. The relative ATP hydrolysis activities of the VirB11 and its mutants are shown in Figure 32.

The mutant proteins of *BaVirB11* were evaluated for their ATP binding activities by using ATP-agarose binding assay as described in the material and methods section. The samples were subsequently separated by SDS-PAGE and subjected to Coomassie blue staining. The amount of ATP-agarose bound protein can be visualized and are shown in Figure 33.

The most prominent feature in the amino acid sequences of the VirB11 is the presence of a conserved ATP binding motif, Walker A. Studies have shown that mutations of invariant residues within the Walker A region in the VirB11 of *Helicobacter pylori* block the substrate transfer to recipient cells, and the purified mutant proteins show defect in ATP binding and hydrolysis (Berger and Christie 1994; Krause et al., 2000). Our Walker A mutant K188Q of *BaVirB11* showed dramatically decreased ATP hydrolysis activity (5% active compared with the wild-type enzyme) (Figure 32). The ATP-agarose binding assay confirmed that the loss of ATP hydrolysis activity in the Walker A mutant resulted from the decreased ATP binding affinity to the enzyme

(Figure 33). These results along with the wild-type enzyme control were used to validate the experimental methods.

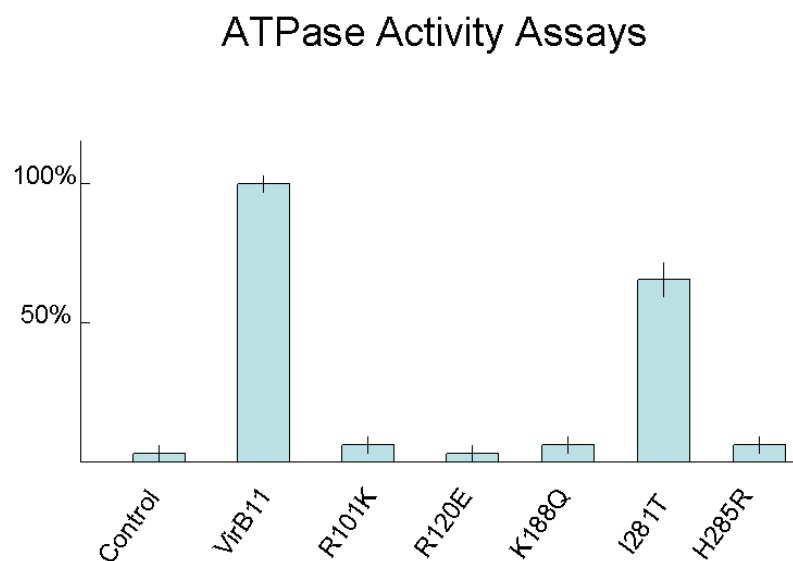


Figure 32. ATPase activities of *BaVirB11* and its mutants. All assays were performed with the enzyme at a final concentration of 1nM. Each reaction mixture was incubated for 10 minutes prior to the addition of ATP. Data were plotted as % label as Pi release with the wild-type enzyme as 100%.

H285R is a His-box mutant. The equivalent mutation in *A. tumefaciens* was shown to affect T-pilus formation *in vivo* (Savvides et al., 2003). The residues in His-box were shown to function catalytically ATP hydrolysis (Savvides et al., 2003). The mutant

displayed a weaker ATP binding affinity (Figure 33) and decreased ATP hydrolysis activity (Figure 32), conforming the direct involvement of His285 in the nucleotide binding and hydrolysis.

The I281T mutant has been regarded as an uncoupling mutant (I265T in *A. tumefaciens* VirB11) that shows no effect on substrate transfer but abolishes the formation of the T-pilus (Sagulenko et al., 2001). However, the ATP binding affinity and ATPase activity of the mutant enzyme have not been shown before. It is not clear why this mutant can translocate substrates efficiently while the pilus formation is disrupted. Sequence alignment reveals that I281 is located in between the two His-box residues H277 and H285 and is highly conserved among T4SS bacteria species (Figure 29). Mutation of I281T affected ATP-binding to the same degree as that of the H285R mutant (Figure 33), indicating I281T binds to ATP at a lower affinity than that of the wild-type enzyme. In contrast to the H285R mutant, the I281T retains its ATP hydrolysis activity to about 70% active as that of the wild-type enzyme (Figure 32). This result explains the retained substrate transfer effect of the I281T mutant. However, it is not known how this mutation affects the pilus formation *in vivo*.

Mutations in the GER motif (R101Q) and the linker region (R120E) of VirB11 completely abolish the ATP hydrolysis activity of the enzyme (Figure 32). The interesting question is how the single site mutation in these regions could affect the enzymatic activity of the VirB11 so dramatically. It has been shown that a non-hydrolysable ATP analog binds to HP0525 in between the interface of the N-terminal domain and the C-terminal domain, and the linker Arg is in close proximity to the ATP



## ATP-binding assays

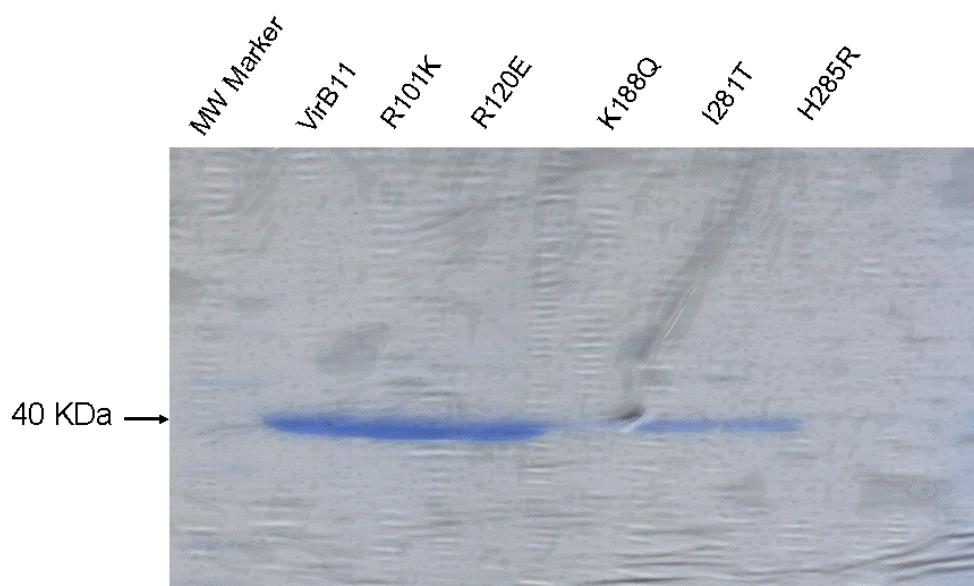


Figure 33. Comparisons of *BaVirB11* and its mutants on ATP-agarose binding. ATP binding assays were performed to determine the ATP binding affinity to the enzyme. ATP-agarose beads were pre-washed with an ATP-binding buffer and each protein sample was added to the ATP-agarose and incubated. The enzyme bound ATP-agarose beads were washed twice with an ATP-washing buffer before eluted with 10mM ATP. The eluted protein samples were run on 12-15% SDS-PAGE and stained by Coomassie blue. The darker band indicates higher affinity of the enzyme to ATP and the lighter band implies the weaker binding.

binding site in the ATP $\gamma$ S-HP0525 complex structure (Savvides et al., 2003). One possibility is that the single site mutation at the linker region might affect ATP binding due to the close proximity to the ATP binding site. To our surprise, the binding affinities of the ATP-agarose to these two mutants are similar to that of the wild-type

enzyme (Figure 33), indicating that mutation in the GER motif or the linker region has no effect on ATP binding. It would be possible that the N-terminal domain of *BaVirB11* organized differently than that of HP0525 so that the linker region is not in close contact to the ATP binding site. Crystal structure analysis may provide a clue to the conformation of the N-terminal domain and the flexibility of the linker region. It has been shown that ATP binding to the Walker A motif is responsible for the conformational changes in the N-terminal domain, not the hydrolysis of ATP (Savvides et al., 2003). A possible explanation for the decreased ATP hydrolysis activity in the linker mutation is that conformational changes at the N-terminal domain upon ATP binding are required for ATP hydrolysis activity. It is likely that the R120E mutation disrupts the flexibly linker and locks the N-terminal domain in one conformation. The binding of ATP to the mutant protein brings no change in the conformation of the linker region and the N-terminal domain, consequently, ATP hydrolysis is disrupted.

VirB11 protein forms stable homohexameric rings capable of ATP binding and hydrolysis (Sexton et al., 2004). To assess the ability of each *BaVirB11* mutant protein to form stable homohexamer, the covalent cross-linking experiments were implemented as described in the Material and Method section. Purified wild-type enzyme was used as a positive control. The cross-linking experiments were repeated three times under various protein concentrations. The proteins were completely dialyzed into a phosphate buffer at pH 7.0. Some protein precipitated during the dialysis and concentration process. Each of the single site mutants generated from this study were capable of forming a stable hexameric complex as indicated by the molecular weight on the SDS-

PAGE (data are not shown), suggesting that the decreased ATP hydrolysis activity in mutant proteins was not a result from the disruption in the formation of the homo-hexamers.

### ***Structure Determination of BaVirB11***

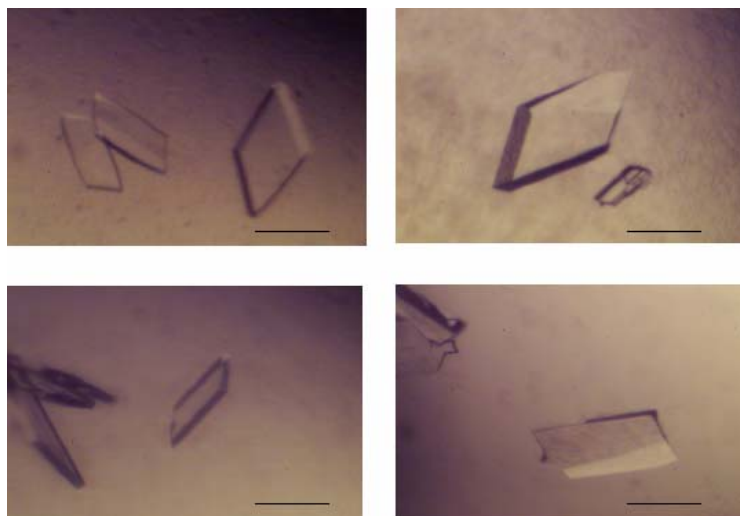
*B. abortus* VirB11 native crystals were obtained at 18 °C from a solution containing 10% w/v PEG-4000, 0.1M HEPES, pH7.5, 0.1 M NaCl. Larger plate-like crystals (Figure 34a) grew in the well in which an additional 10% protein was added two weeks after the initial crystal plate set-up. Hexagonal shaped crystals were obtained from a solution containing 18%PEG400, 0.1M HEPES, pH7.5, and 0.1M MgCl<sub>2</sub> (Figure 34b). The native diffraction data used to solve the structure of *BaVirB11* was collected on an R-AXIS image plate detector (Rigaku-MSD) at the wavelength 1.5418 Å. A total of 180 frames have been collected at 1 degree oscillation. Integration and scaling of the X-ray data was performed using the HKL2000. The hexagonal crystal belongs to space group R3 with unit cell dimensions of  $a=110.58$  Å,  $b=110.58$  Å,  $c=347.29$  Å, and  $\alpha=90^\circ$ ,  $\beta=90^\circ$ , and  $\gamma=120^\circ$ . The solvent content of the unit cell was estimated to be 50.4%, with four molecules per asymmetric unit.

The structure of *BaVirB11* was solved in space group R3 using the molecular replacement method discussed in the Materials and Methods section. The asymmetric unit contains 4 monomers. The model has been refined to R/R<sub>free</sub> of 36.5%/39.7% to a resolution of 3.6 Å with N-terminal residues 1 to 98 missing. This partial model was

used as a search model against a data set collected in the C2 space group to a higher resolution (2.7 Å). The asymmetric unit in this C2 space group contains 6 molecules. The model has been built and refined to contain residues 18 - 348 in each monomer with R/Rfree of 35.6%/40.5% (Table 10). The six subunits in the asymmetric unit differ slightly from each other with a root-mean-square deviation (RMSD) of 0.63 Å for C $\alpha$  atoms between subunit A and B, 0.72 Å between subunit B and C, 0.31 Å between B and D, 0.34 Å between B and E, and 0.42 Å between B and F. Subunit B is the best refined subunit with the highest real space correlation among the six monomers. All of the descriptions of the VirB11 monomer in the following section are based on the refined subunit B.

### ***Structure of the Monomer***

The *Ba*VirB11 monomer contains two domains, an N-terminal domain and a C-terminal domain connected by a linker (Figures 29 and 35). Both of the N- and C-terminal domains of *Ba*VirB11 align well with the corresponding domain in HP0525 (Figures 29 and 36). The topology of both structures, *Ba*VirB11 and HP0525, is similar (Figure 37). The N-terminal domain of *Ba*VirB11 can be superimposed to the



(a) *BaVirB11* crystals --- plat-like crystals in C2 space group



(b) *BaVirB11* crystals --- hexagonal crystals R3 space group

Figure 34. Crystals of the *BaVirB11*.

Table 10. Data collection and structure refinement statistics for *BaVirB11*

	Possible Liganded	Unliganded
A. Data collection statistics		
Wavelength	1.541	0.94
Unit cell parameters		
a	110.6	123.1
b	110.6	233.2
c	347.3	107.3
Space group	R3	C2
Resolution limits	3.6	2.7
Unique reflections	22656	63355
Completeness	88.2 (64.0) <sup>a</sup>	98.2 (89.0) <sup>a</sup>
Rsym <sup>b</sup> (%)	11.8 (23.8)	11.8 (23.8)
I/sigma	8.9 (1.1)	6.5 (1.5)
B. Refinement statistics		
Resolution range	30.0-3.6	30.0-2.7
Test set size	5%	5%
R cryst <sup>c</sup> (%)	36.5	35.6
R free <sup>d</sup> (%)	39.8	40.5
Protein-non-H atoms		11987
Number of water molecule	0	188
Rmsd of bond distances (Å)	0.01	0.01
Rmsd of bond angles (deg)	1.79	1.69
Average B value	79.5	69.64

<sup>a</sup> Numbers in parentheses represent values in the highest resolution shell.

<sup>b</sup>  $R_{\text{sym}} = \frac{\sum_h \sum_i |I(h,i) - \langle I(h) \rangle|}{\sum_h \sum_i I(h,i)}$  where  $I(h,i)$  is the intensity value of  $I(h)$  for all  $i$  measurements.

<sup>c</sup>  $R_{\text{cryst}} = \frac{\sum ||F_o - F_c||}{\sum |F_o|}$ , where  $|F_o|$  and  $|F_c|$  are the observed and calculated structure factor amplitudes respectively.

<sup>d</sup>  $R_{\text{free}}$  is the same as  $R_{\text{cryst}}$  but calculated with 5% subset of all reflections that was never used in any refinement.

Corresponding domain of HP0525 with an RMSD of 1.7 Å for C $\alpha$  atoms over 69 aligned residues. Superimposing of the C-terminal domains from both structures results in an RMSD of 1.3 Å for 110 C $\alpha$  atoms aligned indicating that the C-terminal domain is more conserved than the N-terminal domain.

The N-terminal domain is comprised of residues 18 to 119. Arg18 is the first residue for which interpretable electron density is visible. The N-terminal domain is composed of a six-stranded antiparallel  $\beta$  sheet forming a polar surface that is involved in the protein-protein interaction between the subunits. This interaction is used extensively for the oligomerization of the protein (Savvides et al., 2003). One helix-turn-helix motif (residue 20 to 34) and a longer  $\alpha$  helix (residue 66 to 81) form a convex face against the one side of the  $\beta$  sheet on the N-terminal domain (Figure 35). The  $\beta$ 6 strand runs antiparallel in between  $\beta$  5 and  $\beta$  1 and extends to the linker region. The linker could serve as a spring with a very well balanced N-terminal domain as a hammer head. The observed conformational variability and flexibility of the N-terminal domain in HP0525 could be facilitated by the conserved topological fold of the protein (Savvides et al., 2003).

Two major differences in the N-terminal domain between *BaVirB11* and HP0525 are found. First, the beginning part of the helix  $\alpha$ 1 that extends far out from the core of the protein in HP0525 is disordered in *BaVirB11*. Second, unlike in HP0525, a short helix-turn-helix motif is formed by residue 20 to 34 in the N-terminal domain of *BaVirB11* (Figure 35). This helix-turn-helix motif, also called  $\alpha$  -  $\alpha$  Corner, is a common feature

of hydrophobic interactions. Amino acid side chains at the interface between elements of secondary structure are shielded from water ( Nelson 2000). Interestingly, this helix-turn-helix motif is packed against the hydrophobic side of the N-terminal  $\beta$  sheet, creating a very hydrophobic environment.



Figure 35. Ribbon diagram of the structure of *BaVirB11* monomer. Secondary structural elements are labeled from  $\beta 1$  to  $\beta 13$  for  $\beta$  sheets and  $\alpha 1$  through  $\alpha 9$  for  $\alpha$  helices; a linker is indicated in dark blue. The figure is constructed using program SPOCK.



The C-terminal domain, made up of residue 140 to 346, exhibits a topology with a central  $\beta$  sheet composed of seven  $\beta$ -strands. Five  $\beta$ -strands run parallel in the middle section in the order of  $\beta$  8– $\beta$  10– $\beta$  11– $\beta$  7– $\beta$  12 (Figure 35). Two outer strands  $\beta$  9 and  $\beta$  13 run anti-parallel to its adjacent strand  $\beta$  8 and  $\beta$  12, respectively. The central  $\beta$  sheet is surrounded by six  $\alpha$  helices from both sides of the  $\beta$  sheet. Helices  $\alpha$  4 and  $\alpha$  5 are at one side of the central  $\beta$  sheet and flank the  $\beta$  7 strand on both ends. Helices  $\alpha$  6 through  $\alpha$  9 are packed against the  $\beta$  sheet from the other side. The C-terminal domain contains all four characteristic sequence motifs identified in all members of the T2SS and T4SS superfamily (Planet et al., 2001): the Walker A (P loop), Walker B, His box and Glu box that involved in nucleotide binding (Figure 37).

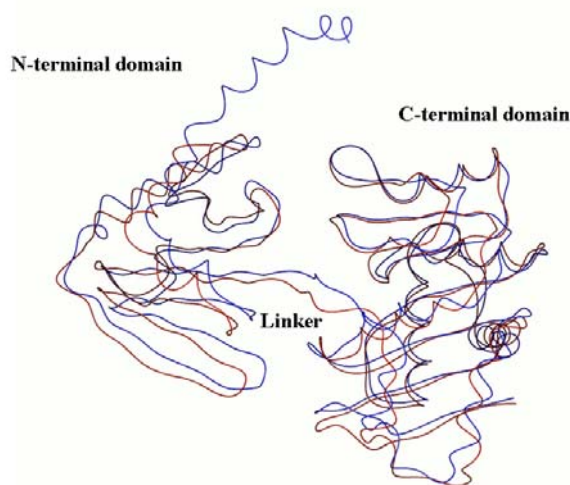


Figure 36. Superposition of HP0525 monomer model (dark blue) and the best refined *BaVirB11* structure (brown). The structures are shown in coil representation.

The two domains are linked by an extended loop between residues 120 and 139 between  $\beta 6$  strand and  $\alpha 4$  helix (Figure 35). The linker starts from the  $\beta 6$  strand in the N-terminal domain cross the interface of the two domains to the outer rim of the C-terminal domain. Sequence alignments reveal that the linker is not conserved among the T4SS (Figure 29). It shows variable length in different bacterial species ranging from 10 to 20 residues. Superimposing *BaVirB11* and HP0525 shows that the linker in *BaVirB11* rotates about 10 degree away from the C-terminal domain resulting in the N-terminal domain shifting further away from the C-terminal domain (Figure 36).

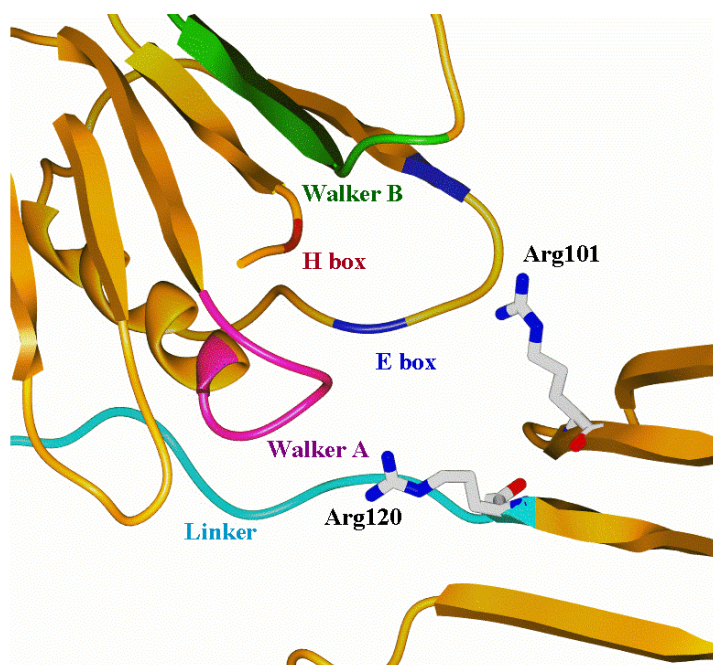


Figure 37. A magnified view of the NTD-CTD interface. The figure is constructed from the subunit B of the hexamer by using the program SPOCK. The linker is colored in blue; Walker A in violet; E box in dark blue; H box in red, and Walker B in green. The side chains of Arg101 and Arg 120 are also high lighted.

### ***Structure of the BaVirB11 Hexamer***

*BaVirB11* protein exists as a homo-hexamer in solution (Figure 31). In the crystal structure, the hexamer is constructed from one of the two trimers in the asymmetric unit by the 2-fold crystallographic symmetry operation. A ribbon diagram of the resulting ring structures are illustrated in Figure 38. A surface diagram showing the electrostatic potential of the hexamers is presented in Figure 39. The hexamer is formed by two layers of rings illustrated by coloring the N- and C-terminal domains differently (Figure 38). The C-terminal domains form a wheel-like ring with an inner hole about 10 Å in diameter and outer rim of ~100 Å in diameter (Figure 39a). The N-terminal domains are positioned counter-clockwise in between two adjacent C-terminal domains forming an outer ring that lies on the top of the C-terminal ring (Figure 38). The inner funnel of the N-terminal ring is ~40 Å in diameter and the outer rim is ~100 Å in diameter. The chamber formed by these two layers of rings has a volume of ~ 70000 Å<sup>3</sup>. The outer surface of the N-terminal ring is flat and the C-terminal surface is more rugged (Figure 39b).

The N-terminal domain protrudes from the C-terminal domain, resulting in no direct contact between the two domains in the same subunit except in the linker interface (Figure 39b). The subunit-subunit interface is extensive, mainly in between the adjacent C-terminal domains and in between an N-terminal domain and its adjacent C-terminal domain. The C-terminal domain to C-terminal domain interaction makes a major contribution to the oligomerization of the protein. The buried interface of the adjacent C-

terminal domains is  $910 \text{ \AA}^2$ . This interface is mainly made up by  $\alpha 8$  from one subunit and  $\alpha 7$  and  $\alpha 9$  from the adjacent subunit. The NTD-CTD interaction is located in between  $\alpha 6$  and  $\beta 9$  from one C-terminal domain and the loop that flanks the  $\beta 5$  and  $\beta 6$  in the adjacent N-terminal domain. The interface in this region buries  $716 \text{ \AA}^2$  of surface area. The ATP binding pocket is located at the interface of the N-terminal domain and the C-terminal domain (Figure 39b).

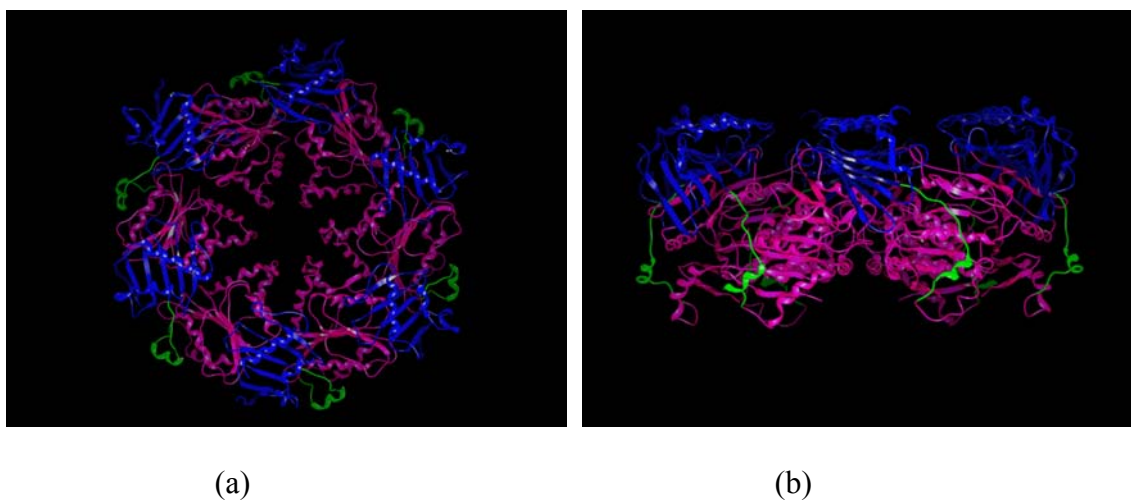
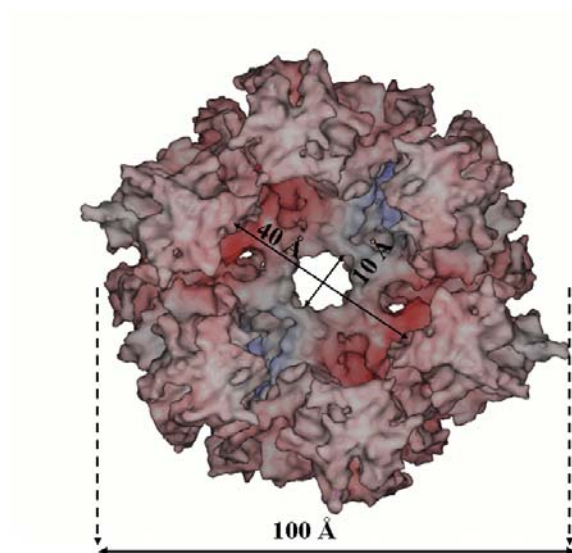
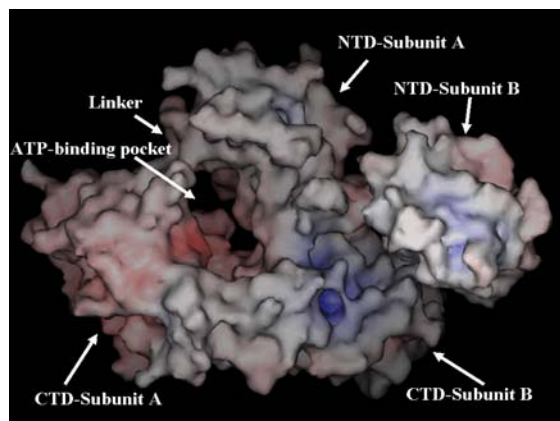


Figure 38. Ribbon diagram of the *BaVirB11* hexamer. The N-terminal domain is colored in dark blue; the C-terminal domain is shown in magenta; the linker is presented in green. (a). Ribbon diagram of the *BaVirB11* hexamer viewed down from the ring formed by the N-terminal domains. (b). Side view of the *BaVirB11* hexamer. The figure is obtained by rotating the *BaVirB11* hexamer shown in (a)  $90^\circ$  up along the horizontal axis of (a).



(a)



(b)

Figure 39. Surface of the *BaVirB11* was displayed using the program SPOCK. Color coding to represent charge is that blue is for the positively charged region, red is for the negatively charged region, and white is for the hydrophobic region. (a). Surface of the *BaVirB11* hexamer viewed down from the N-terminal side to show a large chamber and a small opening. The dimensions of the chamber are indicated. (b). Surface view of subunit-subunit interface.

### *Structural analysis of the BaVirB11 mutants*

The BaVirB11 structure allows the loss of function associated mutations to be explained. Seven of such mutants were generated and five mutants containing a single-site mutation were analyzed for their functionality as reported in the previous section. K118Q, a mutation in the Walker A motif, abolishes the ATP-binding and ATPase hydrolysis activity. R101K, a mutation in the GER motif, was shown to retain the ATP-binding activity (Figure 33). However, the ATPase hydrolysis activity was disrupted (Figure 32). Arg120 is a conserved residue located at the end of the  $\beta$  6 strand in the N-terminal domain and at the beginning of the linker (Figures 29 and 36). R120Q mutant was shown to have a normal ATP-binding affinity when compared with the wild-type enzyme (Figure 33). The ATP hydrolysis activity of R120Q was found to be greatly reduced (Figure 32). The I281T mutation was found to have reduced ATP-binding affinity but retained most of its ATP hydrolysis activity (Figures 32 and 33). The H285R mutation was shown to be inefficient in ATP binding and hydrolysis (Figures 32 and 33).

Figure 40 shows an unbiased electron density at the linker region around the  $\beta$ 5 and  $\beta$  6 sheets to confirm reliable structural analysis in the region. Gln103 and Arg101 from  $\beta$ 5 and Ser116, Thr118, Arg120 and Arg123 from  $\beta$ 6 form a charged surface on one side of the  $\beta$  sheet (Figure 41). The other side of the  $\beta$  sheet is highly hydrophobic, made up of residues Ile125, Ile104, Ile115, Val117 and Ile119 (Figure 41). The charged residues Arg101 and Arg120 are located at the interface of the N-terminal and C-

terminal domains in close proximity to the ATP binding site, but are not directly involved in ATP binding (Figures 36 and 42). Superimposition of HP0525-ATP $\gamma$ S complex structure to the *BaVirB11* reveals that the nucleotide-binding environments of the two proteins are similar. Five mutants generated in this study and their equivalent residues in the structure of HP0525-ATP  $\gamma$ S complex are highlighted for comparison (Figure 42). Lys184 of the HP0525 is a conserved residue in the P loop region. The side chain of Lys 184 interacts directly with the  $\gamma$ -phosphate and plays an important role for ATP binding and hydrolysis (Savvides et al., 2003). The equivalent residue Lys 188 of *BaVirB11* is found in a similar position and its side chain is within the coordination sphere of the ATP  $\gamma$ -phosphate.

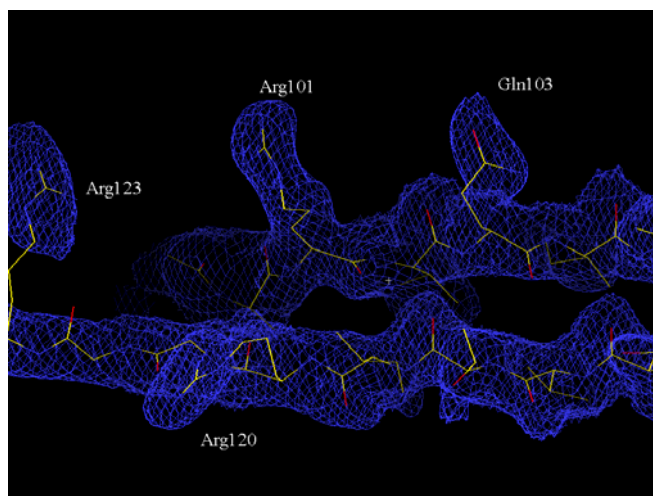


Figure 40. Selected section of the electron density map at the linker region. The  $\beta 5$  and  $\beta 6$  sheets are presented to show very well refined Arg101 and Arg120 residues. Unbiased electron density was calculated using SHAK&WARP, the bias removal server (Reddy 2003). The map was contoured at one sigma and the figure was generated using Xtalview.

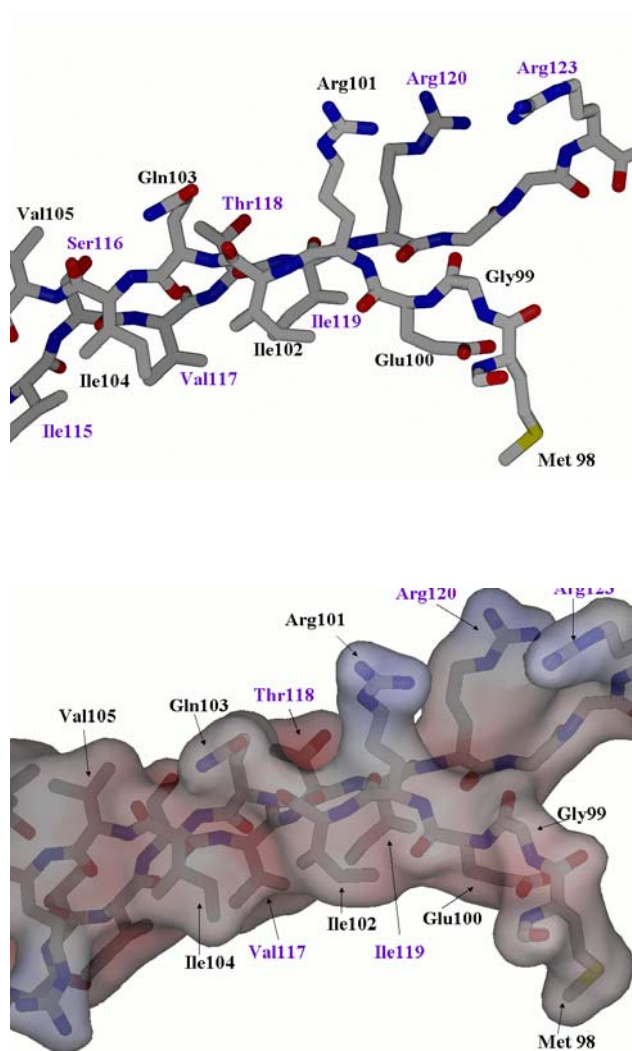


Figure 41. A model of the represented region defined in the figure. Residues from  $\beta 5$  sheet are labeled in black and the residues from  $\beta 6$  sheet and the linker region are labeled in purple. Surface of the model is shown in a transparent mesh and displayed by colored surface potential. Color coding to represent charge is that blue is for the positively charged region, red is for the negatively charged region, and white is for the hydrophobic region.



Replacing the positively charged Lys with a negatively charged Glu disrupts the favorable ionic interactions between the mutated residue and the  $\gamma$ -phosphate of ATP, blocking the ATP-binding and hydrolysis. The imidazole ring of the His285 of the *BaVirB11* flips 90° in respect to the equivalent residue (His273) of the HP0525- ATP  $\gamma$ S (Figure 42). The significance of this change is unknown. It might be caused by a low quality of the structure refinements in the region. The H285 brings more positive charges to the ATP-binding pocket. Mutation of the His285 to an Arg showed a weaker binding affinity for ATP and decreased ATP hydrolysis activity. Although the replaced Arg side chain could supply the positive charges to the ATP binding pocket, the role of the His285 in cleaving the  $\gamma$ -phosphate group and release of ADP as a product is not replaced by the Arg mutation. R113 of HP0525 was proposed to play dual roles in ATP binding and hydrolysis: to provide complementary electrostatic interaction with ATP  $\gamma$ -phosphate and to interact with the catalytic Glu248, a conserved E box residue (Savvides et al., 2003). An equivalent mutant R101K of *BaVirB11* displays a similar ATP binding affinity as the wild-type enzyme (Figure 33) and abolished ATP hydrolysis activity (Figure 32), indicating that direct interaction of Arg 101 with the catalytic Glu is crucial for ATP hydrolysis activity. Arg101 may be involved in product release through interaction with the catalytic Glu residue. Arg120 of *BaVirB11* was found to have the

largest conformational change among the residues proposed with functional mutations (Figure 42). This large conformational change is due to the movement of the flexible linker (Figures 39 and 42). Arg120 is shifted further away from the ATP-binding site and its side chain is located outside the coordination sphere of the ATP binding site as predicated from HP0525-ATP $\gamma$ S structure (Figure 42). R120E of *BaVirB11* exhibits completely diminished ATP hydrolysis activity (Figure 32). However, the mutant displays a similar ATP-binding affinity as the wild-type enzyme (Figure 33), indicating Arg120 is not directly involved in ATP binding. It is possible that the negative charges introduced by Glu to replace the positively charged Arg side chain affect the flexibility of the linker. In the wild-type enzyme, once an ATP molecule binds to the ATP-binding site, the positively charged guanidino group of Arg120 interacts with the negatively charged phosphate group of ATP to bring the N-terminal domains to the closed conformation through movement of the flexible linker. This movement is disrupted in the R120E mutant because the negative charges introduced by glutamic acid repel to the ATP phosphate groups. This may result in the N-terminal domains remaining in their open conformation when ATP binds in the mutant enzyme.

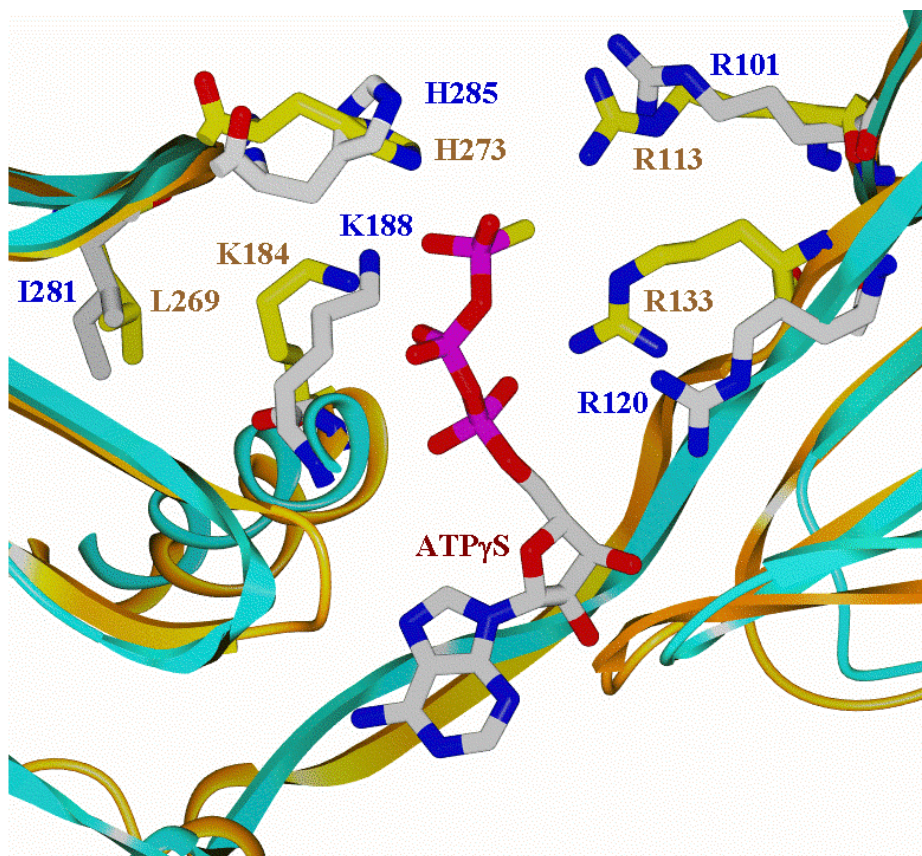


Figure 42. Superimposition of HP0525 and *BaVirB11* at the ATP binding site. The active site architectures of the two proteins are shown. Ribbon of the *BaVirB11* is colored in cyan. Ribbon of the HP0525 is in gold. Five residues that had been mutated in this study are shown in default color in which white is for carbon atoms, red for oxygen and dark blue for nitrogen. The corresponding residues of the HP0525 are in the same color as that of *BaVirB11* except carbon atoms are colored yellow. The ATP $\gamma$ S molecule from HP0525 structure is indicated.

## Summary

VirB11, an ATPase, has been identified as an essential component of the T4SS that mediates the translocation of virulence factors of many pathogenic bacteria into eukaryotic cells (O'Callaghan et al., 1999; Schmiederer and Anderson 2000; Baron et al., 2002; Cascales and Christie 2004; Christie 2004; Remaut and Wakdman 2004; Sexton et al., 2004). It presents an excellent drug target for the development of antimicrobial drugs, as inhibitors of VirB11 would essentially disarm the function of the T4SS. In the thesis, a series of structural and functional studies have been initiated to elucidate the molecular features and structural determinants of the *BaVirB11*. Structure of *BaVirB11* was found to exist as a homohexamer formed by two layers of rings, a wheel-like inner ring formed by the C-terminal domains and an outer ring constituted by the N-terminal domains. The two rings are connected through a linker that is in between the N-terminal domain and the C-terminal domain. A large conformational change was found in the linker region of *BaVirB11* when compared with the structure of HP0525.

In order to elucidate the functional role of each domain and relate its function to the structure, seven mutations of *BaVirB11* were generated, isolated and tested for their ATPase activities and ATP binding affinities. The *BaVirB11* structure allows the loss of function associated with mutations to be explained. In the study, we found that the GER motif and the linker region are crucial for ATP hydrolysis activity of *BaVirB11* to a similar degree as that of the Walker A and the His-box motif. Mutations in the GER motif (R101Q) and the linker region (R120E) of *BaVirB11* completely abolish the ATP hydrolysis activity of the enzyme. However, the binding affinities of the two mutants to

the ATP are similar to that of the wild-type enzyme, indicating that mutation in the GER motif or the linker region has no effect on ATP binding, which is different from the Walker and the His-box motif. A possible explanation for the decreased ATP hydrolysis activity in the linker mutation is that the movement of the linker region rotates the N-terminal domain of VirB11 and serves as the driving force for ATP hydrolysis. The R120E mutation disrupts the flexibly linker and locks the N-terminal domain in one conformation and, consequently, ATP hydrolysis is disrupted.

## CHAPTER V

### SUMMARY AND FUTURE DIRECTIONS

The challenge of fighting against tuberculosis is that there is wide spread drug resistant strains. Primary resistance of *M. tuberculosis* is the resistance to INH, the first line antituberculosis drug. In an effort to elucidate the molecular mechanism of INH activation and the relationship between drug resistance and the function of catalase-peroxidase, we have solved the X-ray crystallographic structures of the wtKatG, S315T mutant, and INH co-crystallized wtKatG. The dimeric enzyme contains a heme cofactor of the iron protoporphyrin IX in each monomer. The heme iron of the wtKatG has six coordinates: the fifth coordinate is occupied by the side chain of His270 from the proximal side of the heme, and the sixth coordinate is from an ordered water molecule on the distal side of the heme. Three catalytically important residues His270, Asp381, and Trp321 from the proximal side of the heme are conserved in the class I peroxidase family. On the distal side of the heme, three catalytically important residues Arg104, Trp107, and His108 are conserved as well. An unusual adduct formed between side chains of Trp107, Tyr229 and Met255 is found to exist in the vicinity of the distal heme binding pocket. Arg418 with double conformation side chains is located near the Trp-Tyr-Met adduct. In one conformation, the guanidino group of Arg418 forms a hydrogen bond with O<sup>n</sup> of Tyr229, the central residue of the adduct. At the alternative conformation, the guanidino group points toward a large U-shaped solvent channel. A molecular surface of the wtKatG reveals that two substrate access channels exist in each

dimer. The major channel provides access to the deeply buried heme with the narrowest neck delimited by the carboxyl group of Asp137 and Ser315. A large U-shaped channel connects to the molecular surface through two funnels. Arg418 is located on the bottom of the channel. In the conformation in which the side chain of Arg418 points to the molecular surface, the U-shaped channel is interrupted, indicating that the channel provides direct access to the adduct through the side chain of Arg418.

Our results provide a detailed picture of how the S315T mutation affects the function of the enzyme by comparing the wtKatG structure to that of the mutant enzyme. The arrangement of the catalytically important residues from both the proximal side and the distal side is essentially the same as that of the wild-type enzyme, indicating the unaltered catalase and peroxidase activities of the mutant. The heme iron in the S315T mutant has 5-coordinate instead of 6-coordinate in the wtKatG. It has been shown that the oxyferrous wtKatG, either as Compound I or Compound II, is capable of oxidizing INH, while the oxyferrous KatG[S315T] is incapable (Ghiladi 2004; Ghiladi et al., 2005). The most significant change in KatG[S315T] is the presence of the methyl group of the side chain of threonine, which effectively narrows the substrate access channel and hinders the continuous flow of the substrates.

The structure of the wtKatG co-crystallized with INH was investigated to identify the substrate binding site in the enzyme. The wild-type enzyme was treated with KCN, an inhibitor for a heme containing enzyme, before the co-crystallization with INH. The overall structure of the wtKatG-INH remained the same as that of the wtKatG. An INH molecule was fitted and refined into a region of electron density located in close

proximity to the Pyrrole I of the distal heme. The pyridine ring of INH is located parallel to the heme plane. The carbonyl oxygen of INH forms hydrogen bond with N<sup>ε1</sup> of the indole ring of Trp107 and the pyridinyl nitrogen of INH forms hydrogen bond with the nitrogen atom of Tyr229. Both Trp107 and Tyr229 are involved in the distal adduct formation. The nicotinamide-NH<sub>2</sub> group of INH forms a hydrogen bond with the carboxyl group of Asp137, a key residue that has been proposed to play a role in the binding and activation of INH (Jakopitsch et al. 2003b). Our data revealed an excellent position for INH binding and activation through interaction with Asp137 and the distal adduct. Future work would be to determine structures of Compound I, Compound II and Compound III by using the KatG[Yy229F] mutant to elucidate the catalytic mechanism of the enzyme.

VirB11, an ATPase, has been identified as an essential component of the T4SS that mediates the translocation of virulence factors of many pathogenic bacteria into eukaryotic cells (O'Callaghan et al., 1999; Schmiederer and Anderson 2000; Baron 2002; Cascales and Christie 2004; Christie 2004; Remaut 2004; Sexton 2004). It presents an excellent drug target for the development of antimicrobial drugs, as inhibitors of VirB11 would essentially disarm the function of the T4SS. In the thesis, a series of structural and functional studies have been initiated to elucidate the molecular features and structural determinants of the *Ba*VirB11. Structure of *Ba*VirB11 was found to exist as a homohexamer formed by two layers of rings, a wheel-like inner ring formed by the C-terminal domains and an outer ring constituted by the N-terminal domains. The two rings are connected through a linker that is in between the N-terminal domain and



the C-terminal domain. A large conformational change was found in the linker region of *BaVirB11* when compared with the structure of HP0525.

In order to elucidate the functional role of each domain and relate its function to the structure, seven mutations of *BaVirB11* were generated, isolated and tested for their ATPase activities and ATP binding affinities. The *BaVirB11* structure allows the loss of function associated with mutations to be explained. In the study, we found that the GER motif and the linker region are crucial for ATP hydrolysis activity of *BaVirB11* to a similar degree as that of the Walker A and the His-box motif. Mutations in the GER motif (R101Q) and the linker region (R120E) of *BaVirB11* completely abolish the ATP hydrolysis activity of the enzyme. However, the binding affinities of the two mutants to the ATP are similar to that of the wild-type enzyme, indicating that mutation in the GER motif or the linker region has no effect on ATP binding, which is different from the Walker and the His-box motif. A possible explanation for the decreased ATP hydrolysis activity in the linker mutation is that the movement of the linker region rotates the N-terminal domain of VirB11 and serves as the driving force for ATP hydrolysis. The R120E mutation disrupts the flexibly linker and locks the N-terminal domain in one conformation and, consequently, ATP hydrolysis is disrupted.

The work on the I281T mutant reveals that the mutant binds ATP weakly; however, it retains its ATPase activity. Interestingly, the I281T mutant was found to show no effect on substrate transfer but abolishes the formation of the T-pilus (Sagulenko et al., 2001). Structural analysis reveals that I281 is located in between the two His-box residues H277 and H285 and is not in direct contact to the ATP-binding site. This may

explain the efficient substrate transfer in the I281T mutant because of the retained ATP hydrolysis activity of the mutant enzyme. However, it is not known how this mutation affects the pilus formation *in vivo*.

In order to further investigate the functional role of each domain, more structural studies are needed. The primary study shows that each mutant forms crystals in different shapes, which even resulted in different space groups under different crystallization conditions. Structures of the linker mutant, the GER motif mutant and the I281T mutant may help us understand the mechanism of the *BaVirB11* better, especially when the structures of the substrate bound mutants are available. To further study the roles of the linker region and the GER motif in substrate transfer and the pilus biogenesis of the T4SS, each mutant gene can be transformed into the wild-type *A. tumefaciens* strain (A348) or the  $\Delta$ VirB11 gene deletion strain and the virulence assays can be performed and compared using T-pilus isolation and conjugation assay. Nucleotide-dependent conformational changes in the linker mutant and the GER mutant can be compared by the analytical sedimentation studies. We also may be able to monitor the conformational change during ATP binding and hydrolysis by using the MINT-ATP, which releases fluorescence upon the ATP binding.

VirB11 was shown to interact with other VirB protein components such as VirB1, VirB4 and VirB10, to coordinate substrate transfer across the inner membrane. The structures of the protein-protein complexes are more likely to give us insight about the functionality of the VirB11 protein as well as the T4SS.

The ultimate goal of the structural studies is to design drugs that can be used to treat the T4SS dependent pathogens. Such drugs would disarm but not kill the pathogens and therefore not be subject to resistance selection as other classical antibiotics.

## REFERENCES

- Acha P, Szylres B (1980) *Zoonoses and Communicable Diseases Common to Man and Animals*. Washington, DC: Pan American Health Organization.
- Adams PD, Grosse-Kunstleve RW, Hung LW, Ioerger TR, McCoy AJ, et al., (2002) PHENIX: building new software for automated crystallographic structure determination. *Acta Crystallogr D Biol Crystallogr* **58**(Pt 11): 1948-1954.
- Alexander S, Brigitte P, Saint-Joanis B, Cole ST (2002) Effect of katG mutations on the virulence of *Mycobacterium tuberculosis* and the implication for transmission in humans, *Infect Immun* **70**(9): 4955-4960.
- Alland DA, Kalkut GE, Moss AR, McAdam RA, Hahn JA, Bosworth W, Drucker E, Bloom BR (1994) Transmission of tuberculosis in New York City: an analysis by DNA fingerprinting and conventional epidemiologic methods. *New Eng J Med* **330**: 1710-1716.
- Andersen C (2001) Protein export and drug efflux through bacterial channel-tunnels. *Curr Opin Cell Biol* **13**: 412-416.
- Anderson LB, Hertzelt AV, Das A (1996) *Agrobacterium tumefaciens* VirB7 and VirB9 form a disulfide-linked protein complex. *Proc Natl Acad Sci USA* **93**(17): 8889-8894.
- Arenas GN, Staskevich AS, Aballay A, Mayorga LS (2000) Intracellular trafficking of *Brucella abortus* in J774 macrophages. *Infect Immun* **68**(7): 4255-4263.

- Ariza J, Corredoira J, Pallares R, Viladrich PF, Rufi G, Pujol, M, Gudiol, F (1995) Characteristics of and risk factors for relapse of brucellosis in humans. *Clin Infect Dis* **20**(5): 1241-1249.
- Ariza J, Pujol M, Valve de J, Nolla JM, Rufi G, Viladrich PF, Corredoira J M, Gudiol F (1993) *Brucellar sacroiliitis*: findings in 63 episodes and current relevance. *Clin Infect Dis* **16**(6): 761-765.
- Atmakuri K, Cascales E, Christie PJ (2004) Energetic components VirD4, VirB11 and VirB4 mediate early DNA transfer reactions required for bacterial type IV secretion. *Mol Microbio* **54**(5): 1199-1211.
- ATS/CDC (1994) Treatment of tuberculosis and tuberculosis infection in adults and children. *Am J Respir Crit Care Med* **149**: 1359-1374.
- ATS/CDC (2003) Update: adverse event data and revised American Thoracic Society/CDC recommendations against the use of rifampin and pyrazinamide for treatment of latent tuberculosis infection-- United States, 2003. *Morbidity and Mortality Weekly Report* **52**(31): 735-739.
- Ayvazian LF (1993) History of tuberculosis. In *Lung biology in health and disease*. Edited by Reichman LB, Hershfield. New York: Marcel Dekker, 1-20
- Banai M, Adams LG, Frey M, Pugh R, Ficht TA (2002) The myth of *Brucella* L-forms and possible involvement of *Brucella* penicillin binding proteins (PBPs) in pathogenicity. *Vet Microbiol* **90**(1-4): 263-279.

- Banerjee AE, Dubnau E., Quemard A, Balasubramanian V, Um KS, Wilson T, Collins D, de Lisle G, Jacobs WR Jr. (1994) inhA, a gene encoding a target for isoniazid and ethionamide in *Mycobacterium tuberculosis*. *Science* **263**: 227-230.
- Baron C, O'Callaghan D, Lanka E. (2002) Bacterial secrets of secretion: EuroConference on the biology of type IV secretion processes. *Mol Microbiol* **43**:1359-1366.
- Baron C, Thorstenson YR, Zambryski PC (1997) The lipoprotein VirB7 interacts with VirB9 in the membranes of *Agrobacterium tumefaciens*. *J Bacteriol* **179**(4): 1211-1218.
- Basso LA, Zheng R., Musser JM, Jacobs WR Jr, Blanchard JS (1998) Mechanisms of isoniazid resistance in *Mycobacterium tuberculosis*: enzymatic characterization of enoyl reductase mutants identified in isoniazid-resistant clinical isolates. *J Infec Dis* **178**: 769-775.
- Bates JH, Stead W (1993) The history of tuberculosis as a global epidemic. *Med Clin North Am* **77**: 1205-1217.
- Battistuzzi G, Bellei M, Borsari M, Di Rocco G, Ranieri A, Sola M (2005) Axial ligation and polypeptide matrix effects on the reduction potential of heme proteins probed on their cyanide adducts. *J Biol Inorg Chem* **10**(6): 643-651.
- Beaupre CE, Bohn J, Dale EM, Binns AN (1997) Interactions between VirB9 and VirB10 membrane proteins involved in movement of DNA from *Agrobacterium tumefaciens* into plant cells. *J Bacteriol* **179**(1): 78-89.

- Berger BR, Christie PJ (1994) Genetic complementation analysis of the *Agrobacterium tumefaciens* virB operon: virB2 through virB11 are essential virulence genes. *J Bacteriol* **176**: 3646-3660.
- Bernstein J, Lott. W, Steinberg BA, Yale HL (1952) Chemotherapy of experimental tuberculosis. V. Isonicotinic acid hydrazide (Nydrazid) and related compounds. *Am Rev Tuberc* **65**: 357-364.
- Bertrand T, Eady N, Jones JN, Jesmin, Nagy JM, Jamart-Gregoire B, Raven EL, Brown KA (2004) Crystal structure of *Mycobacterium tuberculosis* catalase-peroxidase. *J Biol Chem* **279**: 38991-38999.
- Blocker A, Jouihri N, Larquet E, Gounon P, Ebel F, Parsot C, Sansonetti P, Allaoui A (2001) Structure and composition of the *Shigella flexneri* "needle complex", a part of its type III secreton. *Mol Microbiol* **39**(3): 652-663.
- Bloom B, Murry C (1992) Tuberculosis: commentary on a reemergent killer. *Science* **257**: 1055-1064.
- Boschiroli ML, Quahrani-Bettache S, Foulongne V, Michaux-Charachon S, Bourg G, et al., (2002a) Type IV secretion and *Brucella* virulence. *Vet Microbiol* **90**: 341-348.
- Boschiroli ML, Quahrani-Bettache S, Foulongne V, Michaux-Charachon S, Bourg G, et al. (2002b) The *Brucella suis* virB operon is induced intracellularly in macrophages. *Proc Natl Acad Sci USA* **99**(3): 1544-1549.
- Boschiroli ML, Foulongne V, O'Callaghan D (2001) Brucellosis: a worldwide zoonosis. *Curr Opin Microbiol* **4**: 58-64.

- Braibant M, Gilot P, Content J (2000) The ATP binding cassette (ABC) transport systems of *Mycobacterium tuberculosis*. *FEMS Microbiol Rev* **24**(4): 449-467.
- Bravo J, Verdaguer N, Tormo J, Betzel C, Switala J, Loewen PC, Fita I (1995) Crystal structure of catalase HP11 from *Escherichia coli*. *Structure* **3**(5): 491-502.
- Breathnach AS, de Ruiter A, Holdsworth GM, Bateman NT, O'Sullivan DG, Rees PJ, Snashall D, Milburn HJ, Peters BS, Watson J, Drobniewski FA, French GL. (1998) An outbreak of multi-drug-resistant tuberculosis in a London teaching hospital. *J Hosp Infect* **39**(2): 111-117.
- Brunger AT, Adams PD, Clore GM, DeLano WL, Gros P, Grosse-Kunstleve RW, Jiang JS, Kuszewski J, Nilges M, Pannu NS, Read RJ, Rice LM, Simonson T, Warren GL (1998) Crystallography and NMR system: a new software suite for macromolecular structure determination. *Acta Cryst* **54**: 905-921.
- Bumann D, Aksu S, Wendland M, Janek K, Zimny-Arndt U, Sabarth N, Meyer TF, Jungblut PR (2002) Proteome analysis of secreted proteins of the gastric pathogen *Helicobacter pylori*. *Infect Immun* **70**(7): 3396-3403.
- Carpena X, Loprasert S, Mongkolsuk S, Switala J, Loewen PC, and Fita I (2003) Catalase-peroxidase KatG of *Burkholderia pseudomallei* at 1.7Å resolution. *J Mol Biol* **327**: 475-489.
- Cascales E, Christie PJ (2003) The versatile bacterial type IV secretion systems. *Nat Rev Microbio* **1**: 137-150
- Cascales E, Christie PJ (2004) Definition of a bacterial type IV secretion pathway for a DNA substrate. *Science* **304**(5674): 1170-1173.



- Celli J, Gorvel JP (2004) Organelle robbery: *Brucella* interactions with the endoplasmic reticulum. *Curr Opin Microbiol* **7**: 93-97.
- Chaves-Olarte E, Guzman-Verri C, Meresse S, Desjardins M, Pizarro-Cerda J, Badilla J, Gorvel JP, Moreno E (2002) Activation of Rho and Rab GTPases dissociates *Brucella abortus* internalization from intracellular trafficking. *Cell Microbiol* **4**(10): 663-676.
- Chorine V (1945) Action de l'amide nicotinique sur les bacilles du genre *Mycobacterium*. *C R Acad Sci* **220**: 150-151.
- Chouchane S, Lippai I, Magliozzo RS (2000) Catalase-peroxidase (*Mycobacterium tuberculosis* KatG) catalysis and isoniazid activation. *Biochemistry* **39**: 9975-9983.
- Christie PJ (2001) *Agrobacterium tumefaciens* T-complex transport apparatus: a paradigm for a new family of multifunctional transporters in eubacteria. *J Bacteriol* **179**: 3085-3094.
- Christie PJ (2004) Type IV secretion: the *Agrobacterium* VirB/D4 and related conjugation systems. *Biochim Biophys Acta* **1694**: 219-234.
- Christie PJ, Atmakuri K, Krishnamoorthy V, Jakubowski S, Cascales E (2005) Biogenesis, architecture, and function of bacterial type IV secretion systems. *Annu Rev Microbiol* **59**: 451-485.
- Christie PJ, Cascales E (2005) Structural and dynamic properties of bacterial type IV secretion systems (review). *Mol Membr Biol* **22**(1-2): 51-61.
- Christie PJ, Vogel JP (2000) Bacterial type IV secretion: conjugation systems adapted to deliver effector molecules to host cells. *Trends Microbiol* **8**(8): 354-360.

- Christie PJ, Ward JE Jr., Gordon MP, Nester EW (1989) A gene required for transfer of T-DNA to plants encodes an ATPase with autophosphorylating activity. *Proc Natl Acad Sci USA* **86**(24): 9677-9681.
- Christopher JA (2004) SPOCK: the structural properties observation and calculation kit. (online) <http://quorum.tamu.edu>
- Coberly JS (2001) Infectious Disease Epidemiology theory and Practice. *Tuberculosis*, Kenrad NM and Nelson E, Graham, **Chapter 14**: 411-437.
- Cogan EB, Birrell GB, Griffith OH (1999) A robotics-based automated assay for inorganic and organic phosphates. *Anal Biochem* **271**: 29-35.
- Collaborative Computational Project, Number 4 (1994) The CCP4 suite: programs for protein crystallography. *Acta Crystallogr D Biol Crystallogr* **50**: 760-763.
- Comerci D J, Martinez-Lorenzo MJ, Sieira R, Gorvel JP, Ugalde RA (2001) Essential role of the VirB machinery in the maturation of the *Brucella abortus*-containing vacuole. *Cell Microbiol* **3**: 159-168.
- Corbel JM (1997) Brucellosis: an overview. *Emerg Infect Des* **2**: 213-221.
- Corbel JM (1984) Properties of Brucella-phages lytic for non-smooth *Brucella* strains. *Dev Biol Stand* **56**: 55-62.
- Covacci A, Rappuoli R (1993) Pertussis toxin export requires accessory genes located downstream from the pertussis toxin operon. *Mol. Microbiol* **8**(3): 429-434.
- Covacci A, Telford JL, Del Giudice G, Parsonnet J, Rappuoli R (1999) *Helicobacter pylori* virulence and genetic geography. *Science* **284**(5418): 1328-1333.

- Culter S J, Whatmore AM, Commander NJ (2005) Brucellosis -- New aspects of an old disease. *J Applied Microbiology* **98**: 1270-1281.
- Daniel H, Connor, Francis W, Chandler, David A, Schwartz, Herbert J, Manz, Lack E (1997) Tuberculosis. *Pathology of Infectious Diseases*, McGraw-Hill **1**: 857-868.
- Dang TA, Zhou XR Graf B, Christie PJ (1999) Dimerization of the *Agrobacterium tumefaciens* VirB4 ATPase and the effect of ATP-binding cassette mutations on the assembly and function of the T-DNA transporter. *Mol. Microbiol* **32**(6): 1239-1253.
- Das A, Xie YH (2000). The *Agrobacterium* T-DNA transport pore proteins VirB8, VirB9, and VirB10 interact with one another. *J Bacteriol* **182**: 758-763.
- Dean A, Hinshelwood CN (1953) Observation on bacteria adaptation. Adaptation in Microorganisms, 3rd Symp. Soc. *General Microbiology*. Edited by Gale EF. Cambridge, Cambridge University Press: 21-25.
- DeLano WL (2002) The PyMol Molecular Graphics System. [Online] <http://www.pymol.org>.
- Delrue RM, Deschamps C, Leonard S, Nijskens C, Danese I, Schaus JM, Bonnot S, et al., (2005) A quorum-sensing regulator controls expression of both the type IV secretion system and the flagellar apparatus of *Brucella melitensis*. *Cell Microbiol* **7**(8): 1151-1161.
- Delrue RM, Martinez-Lorenzo M, Lestrade P, Danese I, Bielarz V, et al. (2001). Identification of *Brucella spp.* genes involved in intracellular trafficking. *Cell Microbiol* **3**(7): 487-497.

- DelVecchio VG, Kapatral V, Redkar RJ, Patra G, Mujer C, Los T, et al. (2002) The genome sequence of the facultative intracellular pathogen *Brucella melitensis*. *Proc Natl Acad Sci USA* **99**(1): 443-448.
- den Hartigh AB, Sun YH, Sondervan D, Heuvelmans N, Reinders MO, Ficht TA, Tsolis RM (2004) Differential requirements for VirB1 and VirB2 during *Brucella abortus* infection. *Infect Immun* **72**(9): 5143-5149.
- Dessen A, Quemard A, Blanchard J, Jacobs WR Jr, Sacchettini JC (1995) Crystal structure and function of the isoniazid target of *Mycobacterium tuberculosis*. *Science* **267**: 1638-1641.
- Detilleux PG, Deyoe BL, Cheville NF (1990) Entry and intracellular localization of *Brucella spp.* in Vero cells: fluorescence and electron microscopy. *Vet Pathol* **27**(5): 317-328.
- DeVito JA, Morris S (2003) Exploring the structure and function of the mycobacterial KatG protein using trans-dominant mutants. *Antimicrob Agents Chemother* **47**: 188-195.
- Ding Z, Atmakuri K, Christie PJ (2003) The outs and ins of bacterial type IV secretion substrates. *Trends Microbiol* **11**(11): 527-535.
- Drenth J (1999) *Principles of Protein X-ray Crystallography*, 2nd ed. Boston: Springer.
- Dubos R, Dubos J (1952) Tuberculosis, Man and Society. In *The White Plague*. Edited by Mechanie D. Boston: Little Brown: 3-10.
- Dunford HB (1999) Heme peroxidase and Catalase Families and Superfamilies: Crystal Structures. In *Heme Peroxidases*. New York: Wiley & Sons, Inc., 33-57.

- Duroux L, Welinder KG (2003) The peroxidase gene family in plants: a phylogenetic overview. *J Mol Evol* **57**(4): 397-407.
- Ellner JJ (1997) The immune response in human tuberculosis--implications for tuberculosis control. *J Infect Dis* **176**: 1351-1359.
- Emsley P, Cowtan K (2004). Coot: model-building tools for molecular graphics. *Acta Crystallogr D Biol Crystallogr* **60**(Pt 12 Pt 1): 2126-2132.
- Espinal MA, Laszlo A, Simonsen L, Boulahbal F, Kim SJ, Reniero A, Hoffner S, Reider HL, Binkin N, Dye C, Williams, R, Raviglione MC (2001) Global trends in resistance to antituberculosis drugs. *New Engl J Med* **344**: 1294-1303.
- Ferreira CM, da Silva Rosa OP, Torres SA, Ferreira FB, Bernardinelli N (2002) Activity of endodontic antibacterial agents against selected anaerobic bacteria. *Braz Dent J* **13**(2): 118-122.
- Ficht TA (2003) Intracellular survival of Brucella: defining the link with persistence. *Vet Microbiol* **92**: 213-223.
- Filloux A, Michel G, Bally M (1998) GSP-dependent protein secretion in gram-negative bacteria: the Xcp system of *Pseudomonas aeruginosa*. *FEMS Microbiol Rev* **22**(3): 177-198.
- Finzel BC, Poulos TL, Kraut J (1984) Crystal structure of yeast cytochrome c peroxidase refined at 1.7-Å resolution. *J Biol Chem* **259**: 13027-13036.
- Foshay MC, Vitello LB, Erman JE (2004) pH Dependence of heme iron coordination, hydrogen peroxide reactivity, and cyanide binding in cytochrome c peroxidase (H52K). *Biochemistry* **43**(17): 5065-5072.

- Fox H (1952) The chemical approach to the control of tuberculosis. *Science* **116**: 129-134.
- Freer E, Moreno E, Moriyon I, Pizarro-Cerda J, Weintraub A, Gorvel JP (1996) Brucella-Salmonella lipopolysaccharide chimeras are less permeable to hydrophobic probes and more sensitive to cationic peptides and EDTA than are their native Brucella sp. counterparts. *J Bacteriol* **178**(20): 5867-5876.
- Gajhede M, Schuller DJ, Henriksen A, Smith AT, Poulos TL (1997) Crystal structure of horseradish peroxidase C at 2.15 Å resolution. *Nat Struct Biol* **4**: 1032-1038.
- Ghiladi RA, Medzihradzky KF, Rusnak FM, de Montellano PR (2005) Correlation between isoniazid resistance and superoxide reactivity in *Mycobacterium tuberculosis* KatG. *J Am Chem Soc* **127**: 13428-13442.
- Ghiladi RA, Cabelli DE, Ortiz de Montellano PR (2004) Superoxide reactivity of KatG: insights into isoniazid resistance pathways in TB. *J Am Chem Soc* **126**: 4772-4773.
- Gorvel JP, Moreno E (2002) Brucella intracellular life: from invasion to intracellular replication. *Vet Microbiol* **90**(1-4): 281-297.
- Gross-Kunstleve RW, Adams PD (2003) Substructure search procedures for macromolecular structures. *Acta Crystallogr D* **59**: 1966-1973.
- Guzman-Verri C, Chaves-Olarte E, von Eichel-Streiber C, Lopez-Goni I, Thelestam M, Arvidson S, Gorvel JP, Moreno E (2001) GTPases of the Rho subfamily are required for *Brucella abortus* internalization in nonprofessional phagocytes: direct activation of Cdc42. *J Biol Chem* **276**(48): 44435-44443.

- Haase J, Lanka E (1997) A specific protease encoded by the conjugative DNA transfer systems of IncP and Ti plasmids is essential for pilus synthesis. *J Bacteriol* **179**(18): 5728-5735.
- Hapfelmeier S, Domke N, Zambryski PC, Baron C (2000) VirB6 is required for stabilization of VirB5 and VirB3 and formation of VirB7 homodimers in *Agrobacterium tumefaciens*. *J Bacteriol* **182**: 4505-4511.
- Hardt WD, Galan JE (1997) A secreted Salmonella protein with homology to an avirulence determinant of plant pathogenic bacteria. *Proc Natl Acad Sci USA* **94**(18): 9887-9892.
- Harmon BG, Adams LG, Templeton JW, Smith R (1988) Survival of rough and smooth strains of *Brucella abortus* in bovine mammary gland macrophages. *Am J Vet Res* **49**(7): 1092-1097.
- He SY, Nomura K, Whittam TS (2004) Type III protein secretion mechanism in mammalian and plant pathogens. *Biochim Biophys Acta* **1694**(1-3): 181-206.
- Hendrickson W (1991) Determination of macromolecular structures from anomalous diffraction of synchrotron radiation. *Science* **254**: 51-58.
- Hendrickson WA, Horton JR, LeMaster DM (1990) Selenomethionyl proteins produced for analysis by multiwavelength anomalous diffraction (MAD): a vehicle for direct determination of three-dimensional structure. *EMBO J* **9**: 1665-1672.
- Henriksen A, Smith A, Gajhede M. (1999) The Structures of the horseradish peroxidase C-ferulic acid complex and the ternary complex with cyanide suggest how peroxidases oxidize small phenolic substrates. *J Biol Chem* **274**: 35005-35011.

- Heym B, Alzari P, Honore N, Cole ST (1995) Missense mutations in the catalase-peroxidase gene, *katG*, are associated with isoniazid resistance in *Mycobacterium tuberculosis*. *Mol Microbiol* **15**(2): 235-245.
- Heyme BY, Zhang Y, Poulet S, Young D, Cole ST (1993) Characterization of the *katG* gene encoding a catalase-peroxidase required for isoniazid susceptibility of *Mycobacterium tuberculosis*. *J Bacteriol* **175**: 4233-4259.
- Hillar A, Peters B, Pauls R, Loboda A, Zhang H, Mauk AG, Loewen PC (2000) Modulation of the activities of catalase-peroxidase HPI of *Escherichia coli* by site-directed mutagenesis. *Biochemistry* **39**(19): 5868-5875.
- Hiner AN, Raven EL, Thorneley RN, Garcia-Canovas F, Rodriguez-Lopez JN (2002) Mechanisms of compound I formation in heme peroxidases. *J. Inorganic Biochemistry* **91**: 27-34.
- Hofreuter D, Karnholz A, Haas R (2003) Topology and membrane interaction of *Helicobacter pylori* ComB proteins involved in natural transformation competence. *Int J Med Microbiol* **293**(2-3): 153-165.
- Hofreuter D, Odenbreit S, Haas R (2001) Natural transformation competence in *Helicobacter pylori* is mediated by the basic components of a type IV secretion system. *Mol Microbiol* **41**(2): 379-391.
- Hofreuter D, Odenbreit S, Puls J, Schwan D, Haas R (2000) Genetic competence in *Helicobacter pylori*: mechanisms and biological implications. *Res Microbiol* **151**(6): 487-491.



- Hoppner C, Carle A, Sivanesan D, Hoepfner S, Baron C (2005). The putative lytic transglycosylase VirB1 from *Brucella suis* interacts with the type IV secretion system core components VirB8, VirB9 and VirB11. *Microbiology* **151**: 3469-3482.
- Hueck CJ (1998) Type III protein secretion systems in bacterial pathogens of animals and plants. *Microbiol. Mol. Biol. Rev.*, **62**(2), 379-433.
- Ioerger T, Sacchettini JC (2003) The TEXTAL System: artificial intelligence techniques for automated protein model building. *Methods Enzymol* **374**: 244-270.
- Itakura H, Oda Y, Fukuyama K (1997) Binding mode of benzhydroxamic acid to *Arthromyces ramosus* peroxidase shown by X-ray crystallographic analysis of the complex at 1.6 Å resolution. *FEBS Lett* **412**(1): 107-110.
- Jakopitsch C, Auer M, Ivancich A, Ruker F, Furtmüller PG, Obinger C (2003a) Total conversion of bifunctional catalase-peroxidase (KatG) to monofunctional peroxidase by exchange of a conserved distal side tyrosine. *J Biol Chem* **278**: 20185-20191.
- Jakopitsch C, Auer M, Regelsberger G, Jakopitsch W, Furtmüller PG, Ruker F, Obinger C (2003b) The catalytic role of the distal site asparagine-histidine couple in catalase-peroxidases. *Eur J Biochem* **270**: 1006-1013.
- Jakopitsch C, Wanasinghe A, Jantschko W, Furtmüller PG, Obinger C (2005) Kinetics of interconversion of ferrous enzymes, compound II and compound III, of wild-type *Synechocystis* catalase-peroxidase and Y249F: proposal for the catalytic mechanism. *J Biol Chem* **280**(10): 9037-9042.
- Jakubowski SJ, Cascales E, Krishnamoorthy V, Christie PJ (2005) *Agrobacterium tumefaciens* VirB9, an outer-membrane-associated component of a type IV secretion

system, regulates substrate selection and T-pilus biogenesis. *J Bacteriol* **187**(10): 3486-3495.

Jakubowski SJ, Krishnamoorthy V, Cascales E, Christie PJ (2004). *Agrobacterium tumefaciens* VirB6 domains direct the ordered export of a DNA substrate through a type IV secretion System. *J Mol Biol* **341**(4): 961-977.

Jakubowski SJ, Krishnamoorthy V, Christie PJ (2003) *Agrobacterium tumefaciens* VirB6 protein participates in formation of VirB7 and VirB9 complexes required for type IV secretion. *J Bacteriol* **185**(9): 2867-2878.

Johnsson K, King D, Schultz PG (1998) Studies on the mechanism of action of isoniazid and ethionamide in the chemotherapy of tuberculosis. *J Am Chem Soc* **117**: 5009-5010.

Johnsson K, Schultz PG (1994) Mechanistic studies of the oxidation of isoniazid by the catalase-peroxidase from *Mycobacterium tuberculosis*. *J Am Chem Soc* **116**: 7425-7426.

Jones AL, Shirasu K, Kado CI (1994) The product of the virB4 gene of *Agrobacterium tumefaciens* promotes accumulation of VirB3 protein. *J Bacteriol* **176**(17): 5255-5261.

Jones P (2001) Roles of water in heme peroxidase and catalase mechanisms. *J Biol Chem* **276**: 13791-13796.

Kapetanaki S, Chouchane S, Giroto S, Yu S, Magliozzo RS, et al., (2003) Conformational differences in *Mycobacterium tuberculosis* catalase-peroxidase

KatG and its S315T mutant revealed by resonance Raman spectroscopy. *Biochemistry* **42**: 3835-3845.

Karnholz A, Hoefler C, Odenbreit S, Fischer W, Hpfreuter D, et al., (2006) Functional and topological characterization of novel components of the comB DNA transformation competence system in *Helicobacter pylori*. *J Bacteriol* **188**(3): 882-893.

Khan MY, Mah, MW, Memish ZA (2001) Brucellosis in pregnant women. *Clin Infect Dis* **32**(8): 1172-1177.

Kissinger CR, Daniel K, Gehlhaar, David B, Fogel (1999) Rapid automated molecular replacement by evolutionary search. *Acta Crystallographica* **D55**: 484-491.

Komoriya K, Shibano N, Higano T, Azuma N, Yamaguchi S, Aizawa SI (1999) Flagellar proteins and type III-exported virulence factors are the predominant proteins secreted into the culture media of *Salmonella typhimurium*. *Mol Microbiol* **34**(4): 767-779.

Krall L, Wiedemann U, Unsin G, Weiss S, Domke N, Baron C (2002) Detergent extraction identifies different VirB protein subassemblies of the type IV secretion machinery in the membranes of *Agrobacterium tumefaciens*. *Proc Natl Acad Sci USA* **99**(17): 11405-11410.

Kraulis PJ (1991) MOLSCRIPT: a program to produce both detailed and schematic plots of protein structures. *J Applied Crystallogr* **24**: 946-950.

Krause S, Barcena M, Pansegrau W, Lurz R, Carazo JM, Lanka E (2000) Sequence-related protein export NTPases encoded by the conjugative transfer region of RP4

and by the *cag* pathogenicity island of *Helicobacter pylori* share similar hexameric ring structures. *PNAS* **97**: 3067-3072.

Krause S, Pansegrau W, Lurz R, de la Cruz F, Lanka E (2000) Enzymology of type IV macromolecule secretion systems: the conjugative transfer regions of plasmids RP4 and R388 and the *cag* pathogenicity island of *Helicobacter pylori* encode structurally and functionally related nucleoside triphosphate hydrolases. *J Bacteriol* **182**: 2761-2770.

Kremer L, Dover LG, Morbidoni HR, Vilcheze C, Maughan WN, Baulard A, Tu SC, Honore N, Deretic V, Sacchettini JC, Locht C, Jacobs WR Jr, Besra GS (2003) Inhibition of InhA activity, but not KasA activity, induces formation of a KasA-containing complex in mycobacteria. *J Biol Chem* **278**(23): 20547-20554.

Laberge M, Osvath S, Fidy J (2001) Aromatic substrate specificity of horseradish peroxidase C studied by a combined fluorescence line narrowing/energy minimization approach: the effect of localized side-chain reorganization. *Biochemistry* **40**: 9226-9237.

Lai EM, Chesnokova O, Banta LM, Kado CI (2000) Genetic and environmental factors affecting T-pilin export and T-pilus biogenesis in relation to flagellation of *Agrobacterium tumefaciens*. *J Bacteriol* **182**(13): 3705-3716.

Lai EM, Eisenbrandt R, Kalkum M, Lanka E, Kado CI (2002) Biogenesis of T pili in *Agrobacterium tumefaciens* requires precise VirB2 propilin cleavage and cyclization. *J Bacteriol* **184**(1): 327-330.

- Lai EM, Kado CI (1998) Processed VirB2 is the major subunit of the promiscuous pilus of *Agrobacterium tumefaciens*. *J Bacteriol* **180**(10): 2711-2717.
- Laskowski RA, MacArthur MW, Moss DS, Thornton JM (1993) PROCHECK: a program to check the stereochemical quality of protein structures. *J Appl Cryst* **26**: 283-291.
- Lei B, Wei CJ, Tu SC (2000) Action mechanism of antitubercular isoniazid. Activation by *Mycobacterium tuberculosis* KatG, isolation, and characterization of InhA inhibitor. *J Biol Chem* **275**: 2520-2526.
- Llosa M, Gomis-Ruth FX, Coll M, de la Cruz F (2002) Bacterial conjugation: a two-step mechanism for DNA transport. *Mol Microbiol* **45**(1): 1-8.
- Lopez-Goni I, Guzman-Verri C, Manterola L, Sola-Landa A, Moriyon I, Moreno E (2002) Regulation of *Brucella* virulence by the two-component system BvrR/BvrS. *Vet Microbiol* **90**(1-4): 329-339.
- Magliozzo R, Marcinkeviciene JA (1997) The role of Mn(II)-peroxidase activity of mycobacterial catalase-peroxidase in activation of the antibiotic isoniazid. *J Biol Chem* **272**: 8867-8870.
- Manca C, Paul S, Barry CE, Freedman VH, Kaplan G (1999) Mycobacterium tuberculosis catalase and peroxidase activities and resistance to oxidative killing in human monocytes in vitro. *Infect Immun* **67**: 74-79.
- Manterola L, Moriyon I, Moreno E, Sola-Landa A, Weiss DS, et al., (2005) The lipopolysaccharide of *Brucella abortus* BvrS/BvrR mutants contains lipid A

modifications and has higher affinity for bactericidal cationic peptides. *J Bacteriol* **187**(16): 5631-5639.

Marchesini MI, Ugalde JE, Czibener C, Comerici DJ, Ugalde RA (2004) N-terminal-capturing screening system for the isolation of *Brucella abortus* genes encoding surface exposed and secreted proteins. *Microb Pathog* **37**(2): 95-105.

Marrakchi H, Laneelle G, Quemard AI (2000) InhA, a target of the antituberculous drug isoniazid, is involved in a mycobacterial fatty acid elongation system, FAS-II. *Microbiology* **146**: 289-296.

McCoy AJ, Grosse-Kunstleve RW, Storoni LC, Read RJ (2005) Likelihood-enhanced fast translation functions. *Acta Crystallogr D Biol Crystallogr* **61**(Pt 4): 458-464.

McDemott W (1958) Microbial perristence. *Yale J Biol Med* **30**: 257-291.

McRee DE (1999) XtalView/Xfit--A versatile program for manipulating atomic coordinates and electron density. *J Struct Biol* **125**(2-3): 156-165.

Mecsas J, Raupach B, Falkow S (1998) The *Yersinia* Yops inhibit invasion of *Listeria*, *Shigella* and *Edwardsiella* but not *Salmonella* into epithelial cells. *Mol Microbiol* **28**(6): 1269-1281.

Meyer H (1912) Uber hydrazinderivate de pyridincarbonsauren. *Montashefte Chem* **33**: 393-414.

Middlebrook G (1952) Sterilization of tubercle bacilli by INH and incidence of variants resistant to drug in vitro. *Am Rev Tuberc* **65**: 765-767.

- Middleton R, Sjolander K, Krishnamurthy N, Foley J, Zambryski P (2005) Predicted hexameric structure of the *Agrobacterium* VirB4 C terminus suggests VirB4 acts as a docking site during type IV secretion. *Proc Natl Acad Sci USA* **102**(5): 1685-1690.
- Mo L, Zhang W, Wang J, Weng XH, Chen S, Shao LY, Pang MY, Chen ZW (2004) Three-dimensional model and molecular mechanism of *Mycobacterium tuberculosis* catalase-peroxidase (KatG) and isoniazid-resistant KatG mutants. *Microbial Drug Resistance* **10**(4): 269-279.
- Moreno E, Moriyon I (2002) *Brucella melitensis*: a nasty bug with hidden credentials for virulence. *Proc. Natl. Acad. Sci. USA* **99**(1): 1-3.
- Moreno E, Stackebrandt E, Dorsch M, Wolters J, Busch M, Mayer H (1990) *Brucella abortus* 16S rRNA and lipid A reveal a phylogenetic relationship with members of the alpha-2 subdivision of the class Proteobacteria. *J Bacteriol* **172**(7): 3569-3576.
- Morse D, Brothwell D, Ucko PJ (1964) Tuberculosis in ancient Egypt. *Am Rev Respir Dis* **90**: 524-541.
- Muir RE, Gober JW (2002) Mutations in FlbD that relieve the dependency on flagellum assembly alter the temporal and spatial pattern of developmental transcription in *Caulobacter crescentus*. *Mol Microbiol* **43**(3): 597-615.
- Murshudov G, Vagin AA, Dodson EJ (1997) Refinement of macromolecular structures by the maximum-likelihood method. *Acta Crystallogr D Biol Crystallogr* **53**(3): 240-255.
- Murthy M, Reid TJ, Sicignano A, Tanaka N, Rossmann MG. (1981) Structure of beef liver catalase. *J Mol Biol* **152**(2): 465-499.

- Mushegian AR, Fullner KJ, Koonin EV, Nester EW (1996) A family of lysozyme-like virulence factors in bacterial pathogens of plants and animals. *Proc Natl Acad Sci USA* **93**(14): 7321-7326.
- Musser JM (1995) Antimicrobial agent resistance in mycobacteria: molecular genetic insights. *Clinical Microbiology Reviews* (**Oct.**): 496-514.
- Nagai H, Kagan JC, Zhu X, Kahn RA, Roy CR (2002) A bacterial guanine nucleotide exchange factor activates ARF on *Legionella* phagosomes. *Science* **295**: 679-682.
- Nagai H, Roy CR (2001) The DotA protein from *Legionella pneumophila* is secreted by a novel process that requires the Dot/Icm transporter. *EMBO J* **20**(21): 5962-5970.
- Navarro-Martinez A, Solera J, Corredoira J, Beato JL, Martinez-Alfaro E, Atienzar M, Ariza J, (2001) Epididymoorchitis due to *Brucella mellitensis*: a retrospective study of 59 patients. *Clin Infect Dis* **33**(12): 2017-2022.
- Nelson DL, Cox MM (2000) *Lehninger Principles of Biochemistry*. New York: Worth Publishers.
- O'Callaghan, Cazevieille C, Allardet-Servent A, Boschirolu ML, Bourg G, Foulongne V, Frutos P, Kulakov Y, Ramuz M (1999) A homologue of the *Agrobacterium tumefaciens* VirB and Bordetella pertussis Ptl type IV secretion systems is essential for intracellular survival of *Brucella suis*. *Mol Microbiol* **33**: 1210-1220.
- Ochman H, Lawrence JG, Gronisman A (2000) Lateral gene transfer and the nature of bacterial innovation. *Nature* **405**(6784): 299-304.



- Offe HA, Siefken W, Domagk G. 1952 The tuberculostatic activity of hydrazine derivatives from pyridine carboxylic acids and carbony compounds. *Z Naturforsch* **7b**: 462-468.
- Osoba AQ (2003) Microbiology of tuberculosis. In *Tuberculosis*. Edited by Monir Madkour. Berlin, Heidelberg: Springer-Verlag, 115-132.
- Otwinowski Z, Minor W (1997) Processing of X-ray diffraction data collected in oscillation mode. *Methods Enzymol* **276**: 307-326.
- Pansy F, S. H., Donovan R. (1952) *In vitro* studies on isonicotinic acid hydrazide. *Am Rev tuberc* **65**: 761-764.
- Patterson WR, Poulos TL (1995) Crystal structure of recombinant pea cytosolic ascorbate peroxidase. *Biochemistry* **34**: 4331-4341.
- Pizarro-Cerda J, Desjardins M, Moreno E, Akira S, Gorvel JP (1999) Modulation of endocytosis in nuclear factor IL-6(-/-) macrophages is responsible for a high susceptibility to intracellular bacterial infection. *J Immunol* **162**(6): 3519-3526.
- Pizarro-Cerda J, Meresse S, Parton RG, van der Goot G, Sola-Landa A, Lopez-Goni I, Moreno E, Gorvel JP (1998) *Brucella abortus* transits through the autophagic pathway and replicates in the endoplasmic reticulum of nonprofessional phagocytes. *Infect Immun* **66**(12): 5711-5724.
- Planet PJ, Kachlany SC, DeSalle R, Figurski DH (2001) Phylogeny of genes for secretion NTPases: identification of the widespread tadA subfamily and development of a diagnostic key for gene classification. *Proc Natl Acad Sci USA* **98**(5): 2503-2508.

- Poulos TL, Kraut J (1980) The stereochemistry of peroxidase catalysis. *J Biol Chem* **255**: 8199-8205.
- Potterton E, Briggs P, Turkenburg M, Dodson E (2003) A graphical user interface to the CCP4 program suite. *Acta Crystallogr D Biol Crystallogr* **59**: 1131-1137.
- Proshlyakov DA, Pressler MA, DeMaso C, Leykam JF, deWitt DL, Babcock GT (2000) Oxygen activation and reduction in respiration: involvement of redox-active tyrosine 244. *Science* **290**: 1588-1591.
- Pym AS, Saint-Joanis B, Cole ST (2002) Effect of katG mutations on the virulence of *Mycobacterium tuberculosis* and the implication for transmission in humans. *Infection and Immunity* **70**(9): 4955-4960.
- Quemard A, Sacchettini JC, Dessen A, Vilcheze C, Bittman R, Jacobs WR Jr, Blanchard JS (1995) Enzymatic characterization of the target for isoniazid in *Mycobacterium tuberculosis*. *Biochemistry* **34**: 8235-8241.
- Rashkova S, Zhou XR, Chen J, Christie PJ (2000) Self-assembly of the *Agrobacterium tumefaciens* VirB11 traffic ATPase. *J Bacteriol* **182**(15): 4137-4145.
- Rawat R, Whitty A, Tonge PJ (2003) The isoniazid-NAD adduct is a slow, tight-binding inhibitor of InhA, the *Mycobacterium tuberculosis* enoyl reductase: adduct affinity and drug resistance. *PNAS* **100**: 13881-13886.
- Raynal N, Hamaia SW, Siljander PR, Maddox B, Peachey AR, Fernandez R, Foley LJ, Slatter DA, Jarvis GE, Farndale RW (2006) Use of synthetic peptides to locate novel integrin  $\alpha 2 \beta 1$ -binding motifs in human collagen III. *J Biol Chem* **281**(7): 3821-3831.

- Read RJ (2001) Pushing the boundaries of molecular replacement with maximum likelihood. *Acta Cryst* **D57**: 1373-1382.
- Reddy V, Swanson S, Segelke B, Kantardjieff KA, Sacchettini JC, Rupp B(2003) Effective electron density map improvement and structure validation on a linux multi-CPU web cluster: The TB Structural Genomics Consortium Bias Removal Web Service. *Acta Crystallogr* **D59**: 2200-2210.
- Regelsberger G, Jakopitsch C, Ruker F, Krois D, Peschek GA, Obinger C (2000) Effect of distal cavity mutations on the formation of compound I in catalase-peroxidases. *J Biol Chem* **275**: 22845-22861.
- Reid TJ 3rd, Murthy MR, Sicignano A, Tanaka N, Musick WD, Rossmann MG (1981) Structure and heme environment of beef liver catalase at 2.5 Å resolution. *Proc. Natl. Acad. Sci. USA* **78**: 4767-4771.
- Remaut H, Waksman G (2004) Structural biology of bacterial pathogenesis. *Curr Opin Struct Biol* **14**: 161-170.
- Rhodes G (1993) *Crystallography Made Crystal Clear*. San Diego: Academic Press.
- Rieder HL, Cauthen GM, Comstock GW, Snider DE (1989) Epidemiology of tuberculosis in the United States. *Epidemiologic Review* **11**: 79-98.
- Rivas S, Bolland S, Cabezon E, Goni FM, de la Cruz F (1997) TrwD, a protein encoded by the IncW plasmid R388, displays an ATP hydrolase activity essential for bacterial conjugation. *J Biol Chem* **272**(41): 25583-25590.
- Robinson-Dunn B (2002) The microbiology laboratory's role in response to bioterrorism. *Arch Pathol Lab Med* **126**(3): 291-294.

- Rodriguez-Lopez JN, Lowe DJ, Hernandez-Ruiz J, Hiner ANP, Garcia-Canovas F, Thorneley RNF (2001) Mechanism of reaction of hydrogen peroxide with horseradish peroxidase: identification of intermediates in the catalytic cycle. *J Am Chem Soc* **123**: 11838-11847.
- Rouse DA, DeVito JA, Li Z, Byer H, Morris SL (1996) Site-directed mutagenesis of the katG gene of *Mycobacterium tuberculosis*: effects on catalase-peroxidase activities and isoniazid resistance. *Mol Microbiol* **22**(3): 583-592.
- Rouse DA, Li Z, Bai GH, Morris SL (1995) Molecular mechanisms of isoniazid resistance in *Mycobacterium tuberculosis* and *Mycobacterium bovis*. *Infect Immun* **63**: 1427-1433.
- Rozwarski DA, Grant GA, Barton DH, Jacobs WR Jr, Sacchettini JC (1998) Modification of the NADH of the isoniazid target (InhA) from *Mycobacterium tuberculosis*. *Science* **279**: 98-102.
- Sagulenko E, Sagulenko V, Chen J, Christie PJ (2001) Role of *Agrobacterium* VirB11 ATPase in T-pilus assembly and substrate selection. *J Bacteriol* **183**: 5813-5825.
- Sagulenko V, Sagulenko E, Jakubowski S, Spudich E, Christie PJ (2001) VirB7 lipoprotein is exocellular and associates with the *Agrobacterium tumefaciens* T pilus. *J Bacteriol* **183**: 3642-3651.
- Saint-Joanis B, Souchon H, Wilming M, Johnson K, Alzar PM, Cole ST (1999) Use of site-directed mutagenesis to probe the structure, function and isoniazid activation of the catalase/peroxidase, KatG, from *Mycobacterium tuberculosis*. *Biochem J* **338**: 753-760.

Sakula A (1982) Robert Koch: centenary of the discovery of the tubercle bacillus, 1882. *Thorax* **37**(4): 246-251.

Savvides SN, Yeo HJ, Beck MR, Blaesing F, Lurz R, Lanka E, Buhrdorf R, Fischer W, Haas R, Waksman G (2003) VirB11 ATPases are dynamic hexameric assemblies: new insights into bacterial type IV secretion. *EMBO J* **22**: 1969-1980.

Schatz A, Bugie E, Waksman SA (2005) Streptomycin, a substance exhibiting antibiotic activity against gram-positive and gram-negative bacteria. *Clin Orthop Relat Res* **437**(Aug.): 3-6.

Schmidt-Eisenlohr H, Domke N, Angerer C, Wanner G, Zambryski PC, Baron C (1999) Vir proteins stabilize VirB5 and mediate its association with the T pilus of *Agrobacterium tumefaciens*. *J Bacteriol* **181**: 7485-7492.

Schmiederer M, Anderson B (2000) Cloning, sequencing and expression of three *Bartonella henselae* genes homologous to the *Agrobacterium tumefaciens* virB region. *DNA Cell Biol* **19**: 141-147.

Schneider TR, Sheldrick GM (2002) Substructure solution with SHELXD. *Acta Crystallogr D Biol Crystallogr* **58**: 1772-1779.

Schulein R, Dehio C (2002) The VirB/VirD4 type IV secretion system of *Bartonella* is essential for establishing intraerythrocytic infection. *Mol Microbiol* **46**(4): 1053-1067.

Schweinle JE (1990) Evolving concepts of the epidemiology diagnosis, and therapy of *Mycobacterium tuberculosis* infection. *Yale J Bio Med* **117**: 191-196.

- Segal ED, Cha J, Lo J, Falkow S, Tompkins LS (1999) Altered states: involvement of phosphorylated CagA in the induction of host cellular growth changes by *Helicobacter pylori*. *Proc Natl Acad Sci USA* **96**(25): 14559-14564.
- Sexton JA, Pinkner JS, Roth R, Heuser JE, Hultgren SJ, Vogel JP (2004) The *Legionella pneumophila* PilT Homologue DotB exhibits ATPase activity that is critical for intracellular growth. *J Bacteriol* **186**: 1658-1666.
- Sharp KH, Mewies M, Moody PC, Raven EL (2003) Crystal structure of the ascorbate peroxidase-ascorbate complex. *Nat Struct Biol* **10**: 303-307.
- Sherman DR, Mdluli K, Hickey MJ, Arain TM, Morris SL, Barry CE, Stover CK (1996) Compensatory *ahpC* gene expression in isoniazid-resistant *Mycobacterium tuberculosis*. *Science* **272**: 1641-1643.
- Shoeb HA, Bowman BH, Ottolenghi AC, Merola AJ (1985) Peroxidase-mediated oxidation of isoniazid. *Antimicrob Agents Chemother* **27**(3): 399-403.
- Sieira R, Comerci DJ, Sanchez D, Ugalde R (2000) A homologue of an operon required for DNA transfer in *Agrobacterium* is required in *Brucella abortus* for virulence and intracellular multiplication. *J Bacteriol* **182**(17): 4849-4855.
- Sieira R, Comerci DJ, Pietrasanta LI, Ugalde RA (2004) Integration host factor is involved in transcriptional regulation of the *Brucella abortus* *virB* operon. *Mol Microbiol* **54**(3): 808-822.
- Slayden RA, Barry CE (2000) The genetics and biochemistry of isoniazid resistance in *Mycobacterium tuberculosis*. *Microbes Infect* **2**: 659-669.
- Smith LD, Ficht TA (1990) Pathogenesis of *Brucella*. *Crit Rev Microbiol* **17**: 209-230.

- Sola-Landa A, Pizarro-Cerda J, Grillo MJ, Moreno E, Moriyon I, Blasco JM, Gorvel JP, Lopez-Goni I (1998) A two-component regulatory system playing a critical role in plant pathogens and endosymbionts is present in *Brucella abortus* and controls cell invasion and virulence. *Mol Microbiol* **29**(1): 125-138.
- Sopasakis VR, Sandqvist M, Gustafson B, Hammarstedt A, Schmelz M, Yang X, Jansson PA, Smith U (2004) High local concentrations and effects on differentiation implicate interleukin-6 as a paracrine regulator. *Obes Res* **12**(3): 454-460.
- Stathopoulos C, Hendrixson DR, Thanassi DG, Hultgren SJ, St Geme, Curtiss R (2000) Secretion of virulence determinants by the general secretory pathway in gram-negative pathogens: an evolving story. *Microbes Infect* **2**(9): 1061-1072.
- Stephens KM, Roush C, Nester E (1995) *Agrobacterium tumefaciens* VirB11 protein requires a consensus nucleotide-binding site for function in virulence. *J Bacteriol* **177**(1): 27-36.
- Stoeckle MY, Guan L, Riegler N, Weitzman I, Kreiswirth B, Kornblum J, Laraque F, Riley LW (1993) Catalase-peroxidase gene sequences in isoniazid-sensitive and -resistant strains of *Mycobacterium tuberculosis* from New York City. *J Infect Dis* **168**: 1063-1065.
- Sundaramoorthy M, Kishi K, Gold MH, Poulos TL (1994) Preliminary crystallographic analysis of manganese peroxidase from *Phanerochaete chrysosporium*. *J Mol Biol* **238**: 845-848.
- Tampakaki AP, Fadoulglou VE, Gazi AD, Panopoulos NJ, Kokkinidis M (2004) Conserved features of type III secretion. *Cell Microbiol* **6**(9): 805-816.

- Tanaka J, Suzuki T, Mimuro H, Sasakawa C (2003) Structural definition on the surface of *Helicobacter pylori* type IV secretion apparatus. *Cell Microbiol* **5**(6): 395-404.
- Temple AD (1951) Rehabilitation of the tuberculous. *Can J Occup Ther* **18**: 5-16.
- Terradot L, Bayliss R, Oomen C, Leonard G, Baron C, Waksman G (2005) Structures of two core subunits of the bacterial type IV secretion system, VirB8 from *Brucella suis* and ComB10 from *Helicobacter pylori*. *Proc Natl Acad Sci USA* **102**(12): 4596-4601.
- Terradot L, Durnell N, Li M, Li M, Ory J, Labigne A, Legrain P, Colland F, Waksman G (2004) Biochemical characterization of protein complexes from the *Helicobacter pylori* protein interaction map: strategies for complex formation and evidence for novel interactions within type IV secretion systems. *Mol Cell Proteomics* **3**(8): 809-819.
- Thorstenson YR, Kulda GA, Zamrsky PC (1993) Subcellular localization of seven VirB proteins of *Agrobacterium tumefaciens*: implications for the formation of a T-DNA transport structure. *J Bacteriol* **175**(16): 5233-5241.
- Tovar JV, Moreno R, Ferez A, Satorres J, Navarro F, Royo G (1990) Gluteal abscesses caused by *Brucella melitensis*. Probable iatrogenic pathogenesis. *Enferm Infecc Microbiol Clin* **8**(9): 588-588.
- Tu X, Nisan I, Miller JF, Hanski E, Rosenshine I (2001) Construction of mini-Tn5cyaA' and its utilization for the identification of genes encoding surface-exposed and secreted proteins in *Bordetella bronchiseptica*. *FEMS Microbiol Lett* **205**(1): 119-123.



- Turner LR, Lara JC, Nunn DN, Lory S (1993) Mutations in the consensus ATP-binding sites of XcpR and PilB eliminate extracellular protein secretion and pilus biogenesis in *Pseudomonas aeruginosa*. *J Bacteriol* **175**(16): 4962-4969.
- Vagin A, Teplyakov A (1997) MOLREP: an automated program for molecular replacement. *J Appl Cryst* **30**: 1022-1025.
- van Soolingen D, de Haas PE, van Doorn HR, Kuijper E, Rinder H, Borgdorff MW (2000) Mutations at amino acid position 315 of the katG gene are associated with high-level resistance to isoniazid, other drug resistance, and successful transmission of *Mycobacterium tuberculosis* in the Netherlands. *J Infect Dis* **182**: 1788-1790.
- Walter R, Thiel DJ, Barna SL, Tate MW, Wall ME, Eikenberry EF, Gruner SM, Ealick SE (1995) High-resolution macromolecular structure determination using CCD detectors and synchrotron radiation. *Structure* **3**(8): 835-844.
- Ward DV, Draper O, Zupan JR, Zambryski PC (2002) Peptide linkage mapping of the *Agrobacterium tumefaciens* vir-encoded type IV secretion system reveals protein subassemblies. *Proc Natl Acad Sci USA* **99**(17): 11493-11500.
- Watarai M, Andrews HL, Isberg RR (2001). Formation of a fibrous structure on the surface of *Legionella pneumophila* associated with exposure of DotH and DotO proteins after intracellular growth. *Mol Microbiol* **39**: 313-329.
- Weiss AA, Johnson FD, Burns DL (1993) Molecular characterization of an operon required for pertussis toxin secretion. *Proc Natl Acad Sci USA* **90**(7): 2970-2974.
- Welinder KG (1992a) Bacterial catalase-peroxidases are gene duplicated members of the plant peroxidase superfamily. *Biochim Biophys Acta* **1080**: 215-220.

- Welinder KG (1992b) Superfamily of plant, fungal and bacterial peroxidases. *Curr Opin Struc Biol* **2**: 388-393.
- Wengenack NL, Lane BD, Hill PJ, Uh1 Jr, Lukat-Rodgers GS, Hall L, Roberts GD, Cockerill FR, Brennan PJ, Rodgers KR, Belisle JT, Rusnak F (2004) Purification and characterization of *Mycobacterium tuberculosis* KatG, KatG(S315T), and *Mycobacterium bovis* KatG(R463). *Protein Expr Purif* **36**(2): 232-243.
- Wengenack NL, Uh1 Jr, St Amand AL, Tomlinson AJ, Benson LM, Naylor S, Kline BC, Cockerill FR, Rusnak F (1997) Recombinant *Mycobacterium tuberculosis* KatG(S315T) is a competent catalase-peroxidase with reduced activity toward isoniazid. *J Infect Dis* **176**: 722-727.
- WHO (1986) Joint FAO/WHO expert committee on brucellosis. *World Health Organ. Tech Rep Ser* **740**: 1-132.
- WHO (2003) *The World Health Organization Global Tuberculosis Program*. Geneva: World Health Organization.
- WHO (2005) World Health Organization Tuberculosis Fact Sheet. Online <http://www.who.int/gtb/publications/factsheet/>.
- Wilming M (2001) Inter- and intramolecular domain interactions of the catalase-peroxidase KatG from *M. tuberculosis*. *FEBS Lett* **509**: 272-276.
- Winn M, Murshudov GN, Papiz MZ (2003) macromolecular TLS refinement in REFMAC at moderate resolutions. *Methods Enzymol* **374**(14): 300-321.
- Wu H, Fives-Taylor PM (2001). Molecular strategies for fimbrial expression and assembly. *Crit Rev Oral Biol Med* **12**(2): 101-115.

- Yamada Y, Fujiwara T, Sato T, Igarashi N, Tanaka N (2002) The 2.0 Å crystal structure of catalase-peroxidase from *Haloarcula marismortui*. *Nat Struct Biol* **9**(Sep.): 691-695.
- Yeo H, Savvides SN, Herr AB, Lanka E, Waksman G (2000) Crystal structure of the hexameric traffic ATPase of the *Helicobacter pylori* type IV secretion system. *Mol Cell* **6**: 1461-1472.
- Youmans GP, Feldman WH (1946) Increase in resistance of tubercle bacilli to streptomycin. A preliminary report. *Proc Mayo Clin* **21**: 16.
- Young E J (1983) Human brucellosis. *Rev Infect Dis* **5**: 821-842.
- Yuan Q, Carle A, Gao C, Sivanesan D, Aly K, Höppner C, Krall L, Domke N, Baron, C. (2005) Identification of the VirB4-VirB8-VirB5-VirB2 pilus assembly sequence of type IV secretion systems. *J Biol Chem* **280**(28): 26349-26359.
- Zhang Y (2005) The magic bullets and tuberculosis drug targets. *Annu Rev Pharmacol Toxicol* **45**: 529-564.
- Zhang Y, Heym B, Allen B, Young D, Cole S. (1992) The catalase-peroxidase gene and isoniazid resistance of *Mycobacterium tuberculosis*. *Nature* **358**: 591-593.
- Zhang Y, Young DB (1993) Molecular mechanisms of isoniazid: a drug at the front line of tuberculosis control. *Trends Microbiol* **1**(3): 109-113.
- Zhang Y, Garbe T, Young D (1993) Transformation with *katG* restores isoniazid-sensitivity in *Mycobacterium tuberculosis* isolates resistant to a range of drug concentrations. *Mol Microbiol* **8**: 521-524.

- Zhao X, Yu H, Yu S, Wang F, Sacchettini JC, Magliozzo RS (2006) Hydrogen peroxide-mediated isoniazid activation catalyzed by *Mycobacterium tuberculosis* catalase-peroxidase (KatG) and its S315T mutant. *Biochemistry* **45**(13): 4131-4140.
- Zwart PH, Gross-Kunstleve RW, Adams PD (2005) Xtriage and Fest: automatic assessment of X-ray data and substructure factor estimation. *CCP4 Newsletter* (No. 42): 1-2.

**VITA**

Name: Hong Yu

Address: 2108 Demona Dr., Austin, TX 78733

Email: honghyu@hotmail.com

Education: B.S., Northeast Agriculture University, China, 1984  
M.S., Kansas State University, 1991  
Ph.D., Texas A&M University, 2007